HARVARD UNIVERSITY
Graduate School of Arts and Sciences

DISSERTATION ACCEPTANCE CERTIFICATE

The undersigned, appointed by the

Department of Physics

have examined a dissertation entitled

Analytical Methods in Mesoscopic Systems

presented by

Douglas Joseph Mason

candidate for the degree of Doctor of Philosophy and hereby certify that it is worthy of acceptance.

Signature ______________________________

Typed name: Professor Eric Heller, Chair

Signature ______________________________

Typed name: Professor Alan Aspuru-Guzik (CCB)

Signature ______________________________

Typed name: Professor Efthimios Kaxiras

Signature ______________________________

Typed name: Professor Robert Westervelt

Date: May 7, 2012

Analytical Methods in Mesoscopic Systems

A dissertation presented
by

Douglas Joseph Mason

to
The Department of Physics
in partial fulfillment of the requirements
for the degree of
Doctor of Philosophy
in the subject of

Physics

Harvard University
Cambridge, Massachusetts
November 2012

Thesis advisor Author

Eric Heller **Douglas Joseph Mason**

Analytical Methods in Mesoscopic Systems

Abstract

The propsect of designing technologies around the quantum behavior of mesoscopic devices is enticing. This thesis present several tools to facilitate the process of calculating and analyzing the quantum properties of such devices – resonance, boundary conditions, and the quantum-classical correspondence are major themes that we study with these tools. In Chapter 1, we begin by laying the groundwork for the tools that follow by defining the Hamiltonian, the Green's function, the scattering matrix, and the Landauer formalism for ballistic conduction.

In Chapter 2, we present an efficient and easy-to-implement algorithm called the Outward Wave Algorithm, which calculates the conductance function and scattering density matrix when a system is coupled to an environment in a variety of geometries and contexts beyond the simple two-lead schematic. In Chapter 3, we present a unique geometry and numerical method called the Boundary Reflectin Matrix that allows us to calculate the full scattering matrix from arbitrary boundaries of a lattice system, and introduce the phenomenon of internal Bragg diffraction. In Chapter 4, we present a new method for visualizing wavefunctions called the Husimi map, which uses measurement by coherent states to form a bridge between the quantum flux operator and semiclassics. We extend the formalism from Chapter 4 to lattice systems in Chapter 5, and comment on our results in Chapter 3 and other work in the literature.

These three tools – the Outward Wave Algorithm, the Boundary Reflection Matrix, and the Husimi map – work together to throw light on our interpretation of resonance and scattering in quantum systems, effectively codifying the expertise developed in semiclassics over the past few decades in an efficient and robust package. The data and images that they make available promise to help design better technologies based on quantum scattering.

Contents

Citations to Previously-Published Work

Chapter 2 appears almost in its entirety as

> Douglas J. Mason, David Prendergast, Jeffrey B. Neaton, and Eric J. Heller. "Algorithm for efficient elastic transport calculations for arbitrary device geometries" Phys. Rev. B *84*, 155401. (2011). [1]

Chapter 3 appears almost in its entirety as

> Douglas J. Mason, Mario F. Borunda, and Eric J. Heller. "The Boundary Reflection Matrix for Arbitrary Cuts in Lattices" *in preparation* [2]

Chapter 4 appears almost in its entirety as

> Douglas J. Mason, Mario F. Borunda, and Eric J. Heller. "Extending the Concept of Probability Flux" submitted to Physical Review B. arXiv:1205.3708 [3]

Parts of Chapter 4 also appear in

> Douglas J. Mason, Mario F. Borunda, and Eric J. Heller. "Quantum Flux and Reverse Engineering of Quantum Eigenstates" submitted to Physical Review Letters. arXiv/1205.0291 [4]

Most of Chapter 5 except for Section 5.6, and parts of Section 3.5, appear in

> Douglas J. Mason, Mario F. Borunda, and Eric J. Heller. "Husimi Maps in Lattices" submitted to Physical Review B. arXiv:1206.1013 [5]

Section 5.6 appears almost in its entirety as

> Douglas J. Mason, Mario F. Borunda, and Eric J. Heller. "Husimi Maps in Graphene" submitted to Physical Review B. arXiv:1206.1776 [6]

Acknowledgments

Like all theses, this one is the culmination of years of effort and the influences of many people who have come across my path. The person most responsible, of course, is Rick! All those countless meetings where I'd walk into his office to discuss the meaning of a wavefunction, or a physical interpretation of a result – they all built up the intuition and understanding you see here. I loved hearing him fantasize about the possible dynamics of edge states in graphene. While the details of that project didn't pan out, the tools we developed along the way to ask those deep questions certainly did. It has been my goal to codify his very unique perspective on the quantum world, which constitutes the bulk of this thesis. I'm so proud to be his student and to have learned so much from him.

Another important mentor along the way, from an unlikely source, is Michael Cuthbert, Associate Professor at MIT in Musicology. His pioneering work on the Music21 project (REF) taught me that great insights could be made by looking at systems in an aggregate. It is my firm belief that understanding how to write a great piece of music based on the examples set by the great composers is a very similar process to designing a quantum system based on the examples published in the literature. The threads of my music visualization project with him course their way throughout this thesis.

Of course, a major influence on my work was the year I spent with David Prendergast and Jeff Neaton at the Molecular Foundry at Lawrence Berkeley National Laboratory. I came to them with numerical prowess and an obsession with intricate programming, but they taught me to boil down my problems to simple easy-to-understand models and build up from there. I learned so much from them, which is

really remarkable considering that I was merely visiting their group! I feel blessed to have been given so many scientific gifts.

On the personal side, I want to thank all the people in my family: My dad, my mother, my sister, my brother-in-law, and my girlfriend. All of them gave me emotional support and encouraged me along the way. And most importantly, they endured my many descriptions of my work to sort out the kinks, which I'm sure must have sounded like gobbledegook!

Reaching back into my past, I'd also like to thank my mentors in college at USC. Gene Bickers, Werner Dappen, and Maxim Olshanii formed a mighty triumvirate of physics mentors who got me on my feet. Jim Smith, Lynn McGrath, Bill Kanengiser, Brian Head, and Erica Muhl all taught me to love music and its mathematical intricacies. I definitely feel that both music and physics course through this thesis.

Now for the technical stuff: This research was conducted with funding from the Department of Energy Computer Science Graduate Fellowship program under Contract No. DE-FG02-97ER25308. Code and development for Chapter 2, as well as computer time for the SuperLU simulations, were conducted with D. P. and J. N. as a User project at the Molecular Foundry, Lawrence Berkeley National Laboratory, which is supported by the Office of Science, Office of Basic Energy Sciences, of the U.S. Department of Energy under Contract No. DE-AC02-05CH11231. MFB and EJH were supported by the Department of Energy, office of basic science (grant DE-FG02-08ER46513).

For my ever-supportive father, Thomas,

my loving late mother, Eileen,

my partner-in-crime sister, Karen,

my intellectually inspiring brother-in-law, Richard,

my late guitar teacher and musical inspiration, Jim Smith,

and the love of my life who made this thesis possible, Ariel

Chapter 1

Landauer Formalism and the Scattering Matrix

This thesis covers methods for computing and analyzing the single-electron wavefunction in a variety of systems it can inhabit, two of which derive considerable attention – graphene and the two-dimensional electron gas. In this chapter, we cover the fundamentals of the two systems, and the assumptions underlying ballistic conductance experiments and numerical simulations that are used to probe their quantum behaviors. The numerical simulations are based around implementing the Green's function, which describes the response of a system described by a wave equation like the Schrodinger equation, and the scattering matrix, which condenses information about how a small and complicated device interacts with modes at a distance. This chapter acts as a reference for the rest of the thesis: subsequent chapters elaborate on the formalism reviewed here, and occaisionally review a few key elements as relevant to their discussion.

1.1 Two Hamiltonians

This thesis studies scattering phenomena and conductance in two-dimensional systems. In the past few decades, the experimental focus for such phenomena has been placed on two systems: the two-dimensional electron gas (2DEG) which arises from crystal heterostructures like gallium arsenide (GaAs)[7], and an atomically thin sheet of graphite known as a graphene[8]. Because the scattering length in these two systems is large, and because it is possible to examine the behavior of individual electrons in them (hence the "gas" terminology), they are ideal candidates for examining single-body quantum scattering. Moreover, while an electron in the former system behaves like a free particle in the continuum, graphene introduces new behaviors becuase of its band structure and dispersion relation[9].

1.1.1 Graphene

Graphene marched onto the scene in 2004 when it was first isolated by Novoselov and Geim[8] from pencil shavings and scotch tape. In graphene, carbon atoms are arranged in a honeycomb pattern, allowing each atom's s,p_x and p_y orbitals to hybridize into an sp^2 orbital and forge a strong bond between neighboring atoms, collectively known as the valence σ-band. This leaves over the p_z orbital which extends above and below the plane. The collective p_z orbitals form the conductive π^*-band that gives graphene its unique conductive properties (see Fig. 1.1.1).

Because the p_z orbitals are tightly-bound to their carbon atoms, the overlap between p_z orbitals on adjacent atoms is small but non-trivial. As a result, the single electron wavefunction that inhabits the π band can be described by an effective mass

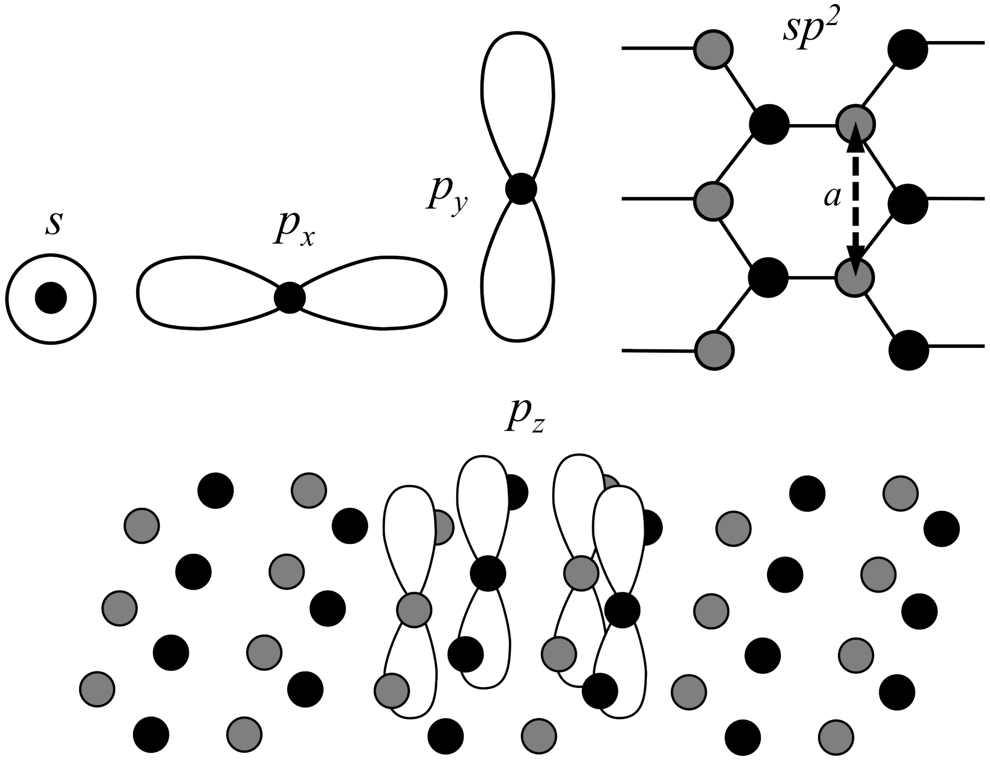

Figure 1.1.1: The atomic orbitals for graphene. The s, p_x, and p_y orbitals form a hybrid sp^2 orbital. The sp^2 orbitals of neighboring atoms overlap to form extraordinarily strong bonds and constitute the valence band. This still leaves over p_z orbitals which collectively form the conduction band. In the unit cell for graphene, there are two sublattices which are indicated in black (grey) for the A (B) sublattices, and the lattice spacing a between adjacent atom sites in the same sublattice is indicated by the dashed double-arrow.

envelope function over the p_z orbitals at each atom site. We can describe the Hamiltonian for this envelope function as a sparse matrix with entries along its diagonal and off-diagonal entires between adjacent orbitals:

$$H = \sum_i \epsilon_i \mathbf{a}_i^\dagger \mathbf{a}_i - t \sum_{\langle ij \rangle} \mathbf{a}_i^\dagger \mathbf{a}_j, \tag{1.1.1}$$

where $\mathbf{a}_i$ is the annihilation operator for the i^{th} orbital, ϵ_i is the energy of the system plus the disorder potential, and $\langle ij \rangle$ cycles through all nearest-neighbor pairs. The hopping parameter t is determined by the inter-orbital overlap. For small perturbations from the interatomic distance $a = 1.42$, the hopping parameter has been computed as $t_l = te^{-3.37(l/a-1)}$[10] where l is the strained inter-atomic distance, although we will not be addressing questions of strain in this dissertation. Also not covered are other approximations to the Hamiltonian, such as next-nearest neighbor tight-binding models.

From this Hamiltonian, we can compute the dispersion relation[11] as

$$\begin{aligned} E\left(\mathbf{k}\right) &= \pm t\sqrt{3+f\left(\mathbf{k}\right)} \\ f\left(\mathbf{k}\right) &= 2\cos\left(\sqrt{3}k_y a\right) + 4\cos\left(\frac{\sqrt{3}}{2}k_y a\right)\cos\left(\frac{3}{2}k_x a\right). \end{aligned} \tag{1.1.2}$$

The plus and minus refer to the positive-energy π^* and negative-energy π orbitals respectively. We have plotted the dispersion relation in Fig. 1.1.2.

At energies close to the Dirac point, defined as $E = 0$, the dispersion relation approximates to the linear relationship $E \approx v_f q$ where $\mathbf{q} = \mathbf{k} - \mathbf{K}^{(\prime)}$ and $\mathbf{K}^{(\prime)}$ are the wavevectors at the edges of the Brillouin zone and shown in Fig. 1.1.2. This linear dispersion relationship distinguishes graphene from the continuous system which has a quadratic relationship $E \propto k^2$.

Solutions to the Bloch equation can be written using the creation operators $\mathbf{a}^\dagger$ and $\mathbf{b}^\dagger$ on the A- and B-sublattices respectively, giving rise to two Dirac pseudospinors written as

$$\psi_{\pm,\mathbf{K}}(\mathbf{k}) = \frac{1}{\sqrt{2}}\left(e^{-i\theta_\mathbf{k}/2}\mathbf{a}^\dagger \pm e^{i\theta_\mathbf{k}/2}\mathbf{b}^\dagger\right) \tag{1.1.3}$$

$$\psi_{\pm,\mathbf{K}'}(\mathbf{k}) = \frac{1}{\sqrt{2}}\left(e^{i\theta_\mathbf{k}/2}\mathbf{a}^\dagger \pm e^{-i\theta_\mathbf{k}/2}\mathbf{b}^\dagger\right), \tag{1.1.4}$$

where $\theta_\mathbf{k} = \arctan\left(\frac{q_x}{q_y}\right)$, and the ± signs indicate whether the positive- or negative-energy solutions are being used[12].

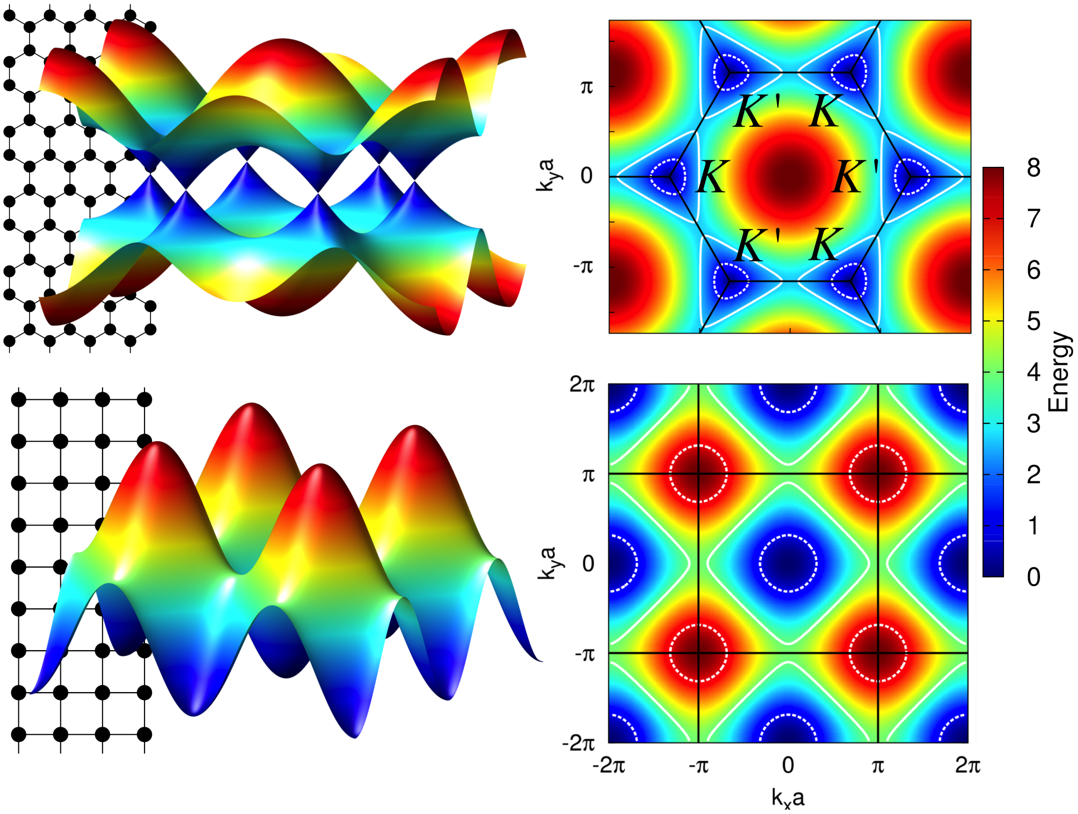

Figure 1.1.2: The dispersion relation for the honeycomb lattice (Eq. 1.1.2) is shown at top-right, and for the square lattice (Eq. 1.1.13) at bottom-right; three-dimensional renditions are shown at the left. The parabolic relationship in the square lattice is instead a linear relationship for the honeycomb lattice at energies near zero, with two distinct valleys (K and K') which appear as cones in the dispersion relation which touch at the Dirac point $E = 0$. In the honeycomb lattice, the dispersion relation for $E = 0.5t$ (dashed white lines) is nearly circular, while the relation at $E = 0.98t$ (solid white lines) shows strong three-way warping. In the square lattice, the dispersion relations for $E = 0.9t$, and $7.1t$ (dashed white lines) are nearly circular, while the relation near the band edge at $E = 3.9t$ (solid white lines) shows strong *four*-way warping. The warping in both relations are further discussed in Chapters 3 and 5.

If you create a coherent state defined as

$$|\mathbf{r}_0, \mathbf{k}_0, \sigma\rangle = \psi_{+,\mathbf{K}^{(\prime)}}(\mathbf{k}_0) e^{-(\mathbf{r}-\mathbf{r}_0)/2\sigma + i\mathbf{k}_0\cdot\mathbf{r}} \tag{1.1.5}$$

and propagate it in time, it will move in the unique direction determined by the group velocity at wavevector $\mathbf{k}_0$. We have tested this and all results in Chapter 3 using the propagator method

$$\psi(t) = e^{iHt}\psi(t=0) \tag{1.1.6}$$

where the matrix exponent is computed using the Expokit library[13, 14].

Away from the Dirac point but between $-2.7\text{eV} < E < 2.7\text{eV}$, the dispersion relation for a given energy transforms from circles around each K-point into triangles, which emphasize three directions for each valley in the distribution of group velocities $v_g = \boldsymbol{\nabla}_{\mathbf{k}} E\left(\mathbf{k}\right)$. As a result, the magnitude of the wavevector $\mathbf{q} = \mathbf{k} - \mathbf{K}^{(\prime)}$ depends on its orientation: It is bounded above by

$$q_{\text{up}} = \frac{2}{a}\cos^{-1}\left[\frac{1}{4t}\left(E + t + \sqrt{-3E^2 - 6Et + 9t^2}\right)\right], \tag{1.1.7}$$

and from below by

$$q_{\text{low}} = \frac{2}{a}\cos^{-1}\left[\frac{1}{4t}\left(-E + t + \sqrt{-3E^2 + 6Et + 9t^2}\right)\right]. \tag{1.1.8}$$

When characterizing the momentum uncertainty, we use the average of these two quantities.

The graphene systems examined in this thesis are cut from an infinite honeycomb lattice. A filter is then applied to remove atom sites which are attached to only one other atom site, and to bridge under-coordinated sites whose π orbitals would strongly overlap. This still leaves over zig-zag edges with under-coordinated orbitals.

For these sites, it is possible to modify the hopping parameters to neighboring sites as well as the onsite energy, called the passivation parameter, to reflect bonding to hydrogen atoms from the environment. We do not make these modifications except to study the role of edge-state hybridization in Sec. 5.6.2.

Recent calculations have suggested that under certain circumstances, zig-zag edges reconstruct to form a 5-7 chain[15]. In Sec. 3.6, we conclude that these edges behave like zig-zag intra-valley scatters at most energies, which has been corroborated by van Ostaay et al.[16]. At higher energies, the presence of internal Bragg diffraction also plays a significant role, with the possibility of incorporating a mixture of both intra- and inter-valley scattering (See Sec. 3.6). For most of this thesis, we restrict our studies to the zig-zag and armchair boundaries, leaving more complicated mixed boundaries to future work.

1.1.2 Finite-Difference Approximation to the Continuum

We can use a similar formalism to describe an electron in a two-dimensional electron gas, which behaves like a free particle in a two-dimensional continuum. To numerically approximate the Schrodinger equation for a continuous system, we sample it along a square lattice and apply the finite difference equations

$$\begin{aligned} \left.\frac{dF}{dx}\right|_{x=x_0} &= \frac{1}{a}\left(F\left(x_0+a\right)-F\left(x_0-a\right)\right) \qquad (1.1.9)\\ \left.\frac{d^2F}{dx^2}\right|_{x=x_0} &= \frac{1}{a^2}\left(F\left(x_0+a\right)-F\left(x_0\right)+F\left(x_0-a\right)\right) \end{aligned}$$

where a is the lattice spacing. For the time-dependent Schrodinger equation

$$i\hbar\frac{\partial}{\partial t}\psi = \hat{H}\psi \qquad (1.1.10)$$

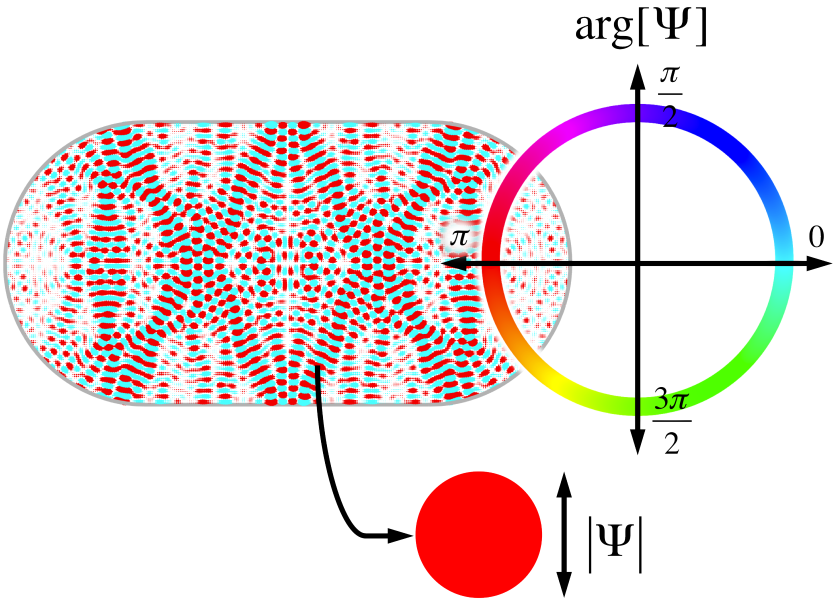

Figure 1.1.3: A wavefunction $\psi(\mathbf{r})$ is represented in this thesis by placing circles at each lattice site. Their radii correspond to $|\psi(\mathbf{r})|$ and their colors correspond to the color wheel above. This wavefunction, taken from Fig. 1.1.3, is stationary, so all probability amplitudes are real. As a result, only cyan and red appear in this representation.

we write out the Hamiltonian

$$\hat{H} = -\frac{\hbar^2}{2m}\nabla^2 + V(\mathbf{r}) \tag{1.1.11}$$

which can be approximated in parallel to the tight-binding equation for graphene (Eq. 1.1.1) as

$$H = \sum_i \epsilon_i \mathbf{a}_i^\dagger \mathbf{a}_i - t \sum_{\langle ij \rangle} \mathbf{a}_i^\dagger \mathbf{a}_j, \tag{1.1.12}$$

where $\epsilon_i = V(\mathbf{r}_i) + 2dt$, d is the dimensionality of the system (always $d = 2$ for this thesis), $t = \frac{\hbar^2}{2ma^2}$, and the set $\langle ij \rangle$ covers all neighboring pairs.

Throughout this thesis, we represent wavefunctions for both the continuous system and the graphene system by placing circles at each point in the numerical lattice whose radii correspond to the absolute value of the probability amplitude $|\psi|$. This ensures that the area contained by each circle corresponds to the measurement probability $|\psi|^2$ at each point. The color of each circle is defined by the phase $\arg(\psi)$ according to Fig. 1.1.3. In this example, which is taken from Fig. 4.0.1, a stationary state has only real wavefunction values, so all colors are either cyan or red. In non-stationary states, like Fig. 4.3.3, the whole color wheel is engaged.

The dispersion relation for the two-dimensional square lattice is thus

$$E(\mathbf{k}) = 4t - 2t\left(\cos(k_x a) + \cos(k_y a)\right) \tag{1.1.13}$$

and is shown in Fig. 1.1.2. For wavelengths that are long compared to the lattice spacing, we can approximate this relationship as $E(\mathbf{k}) = \frac{\hbar^2 k^2}{2m}$, which is the standard kinetic energy in a continuum.

Like the graphene system, the magnitude of the wavevector at any energy of the square lattice depends on its orientation. It is bounded above by

$$k_{\text{up}} = \frac{1}{a}\cos^{-1}\left(\frac{4t-E}{2t}\right), \tag{1.1.14}$$

and from below by

$$k_{\text{low}} = \frac{1}{\sqrt{2}a}\cos^{-1}\left(\frac{4t-E}{4t}\right). \tag{1.1.15}$$

When characterizing the momentum uncertainty, we use the average of these two quantities.

1.2 Ballistic Conductance

Imagine that a small piece of graphene, or any conductive material, is attached to two leads. The system is held at a potential μ_0, but across the two leads a bias

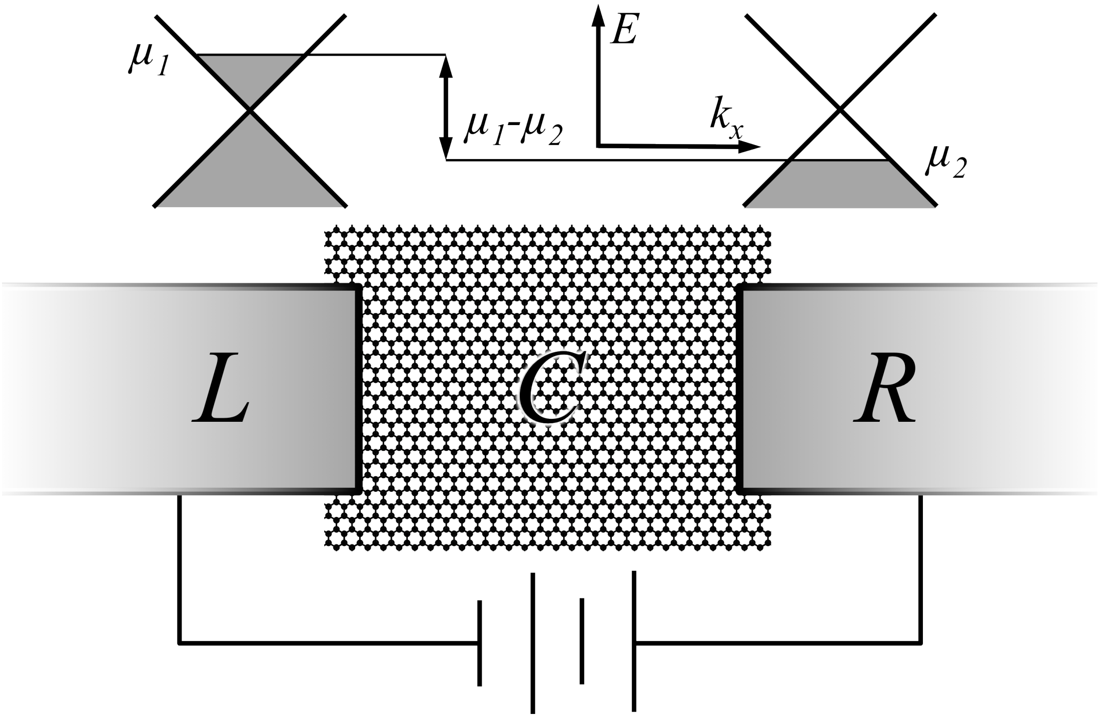

Figure 1.2.1: A schematic of the experimental apparatus for conductance measurements. A central region (C) of graphene is connected to two leads at the left (L) and right (R). A bias voltage V shifts the potentials in each lead, resulting in electrons in the conduction band to flow from left to right which have momenta available in the potential gap and determined by the dispersion relation (top).

voltage V is applied, which raises the potential of the left lead to μ_1 and lowers the potential of the right lead to μ_2 (See Fig. 1.2.1). The difference $\mu_1 - \mu_2 \propto V$, and the potential at each lead corresponds to its Fermi energy, which determines the momenta of electrons that can conduct transport. What is the current through this device?

Ohm's law gives the current in relation to the bias voltage by $I = VG$, where G is the conductance, which is the inverse of the resistance. For large enough samples, the resistance is proportional to the length of the sample between the leads and it's cross-sectional area, or, in the case of a two-dimensional system, it's transverse width.

The resistance arises from the fact that as an electron travels between the leads under the force of the bias voltage, its momentum changes (scatters) in response to a myriad of forces such as phonon scattering, electron-electron interaction, and defect scattering to name a few. Conductance then occurs as a result of drift velocity over many scattered trajectories. But for certain materials, like graphene or gallium arsenide, at low enough temperature the average distance between scattering events can grow to a micron (for graphene, that's several thousand atoms long), which can easily exceed the size of mesoscopic systems. In this case, the conductance of the system is determined by quantum transport.

Due to quantum confinement, a small system can only support a finite set of modes through which electron transport can occur. For the quantum point contact or the simple waveguide, these modes are standing waves between each wall of the waveguide and are known as transverse modes. If the bias voltage is small so that $\mu_1 \approx \mu_2$, then only one conducting electron exists in the device at a time, eliminating interaction effects. For small bias voltages at zero temperature and for systems where the mean-free path between scattering events exceeds the size of the system, the Landauer formula applies[17], which states that the conductivity

$$G = \frac{2e^2}{h} \sum_i T_i, \tag{1.2.1}$$

where T_i is the likelihood that the i^{th} mode of transport transmits across the device. The quantity e is the electron charge, and h is Planck's constant; the factor of two arises from the up and down spins of the electron.

For a simple waveguide with no scattering, T_i is always unity since each mode transmits across the system unfettered, so that the conductance is a simple function of the number of transverse modes. For more complicated system geometries, quantum scattering can reflect some of the transmitting mode back to the incoming lead. As a result, T_i becomes a function of the fermi Energy within the system. At higher temperatures, the conductance in the linear regime can be obtained by applying a Gaussian-like kernel using a thermal broadening function of width k_BT, where k_B is the Boltzmann constant and T refers to the temperature. That is,

$$\bar{G}(E_F) = \frac{2e^2}{h} \int F\left(E - E_F\right) \sum_i T_i(E) dE \tag{1.2.2}$$

where the broadening function is $F\left(E - E_F\right) = \frac{1}{4k_BT}\text{sech}^2\left(\frac{E}{2k_BT}\right)$. The current at larger voltage biases can be obtained by integrating between the potentials at each lead,

$$I = \int_{E_{F_1}}^{E_{F_2}} \bar{G}(E) dE. \tag{1.2.3}$$

Under the assumptions where the Landauer formula applies, the variable needing the most attention is then the set of transmission functions T_i, which depend on quantum scattering matrix, whose calculation and analysis form the bulk of the dissertation

1.3 Scattering Matrix and Green's Function Formalism

Perhaps one of the most valuable currencies in physics is the scattering matrix, a quantity which gives the transition probability from one wavefunction to another. In general, the wavefunctions of interest are *asymptotic* wavefunctions, or modes, far from a scattering center. This section explains how we arrive at the scattering matrix numerically in the case of a device defined by a finite Hamiltonian, and its interaction with asymptotic modes within waveguides that connect to the device.

The scattering matrix can be divided into four blocks, which describe the set of modes that are treated as inputs and outputs:

$$s = \begin{pmatrix} r & t^\dagger \\ t & r^\dagger \end{pmatrix} \tag{1.3.1}$$

The sub-matrices r and t represent the reflection and transmission matrices respectively.

The transmission functions T_i from Eq. 1.2.1 are determined by summing over the scattering matrix elements

$$T_i = \sum_j |t_{ij}|^2 \tag{1.3.2}$$

corresponding to transmission from a particular mode. Determining the scattering matrix for a system can be aided using the Green's function formalism.

1.3.1 The Green's Function

The Green's function for the system in Fig. 1.2.1 is determined by first considering the time-independent Schrödinger equation

$$(E\mathbf{I} - H)\,\psi\left(\mathbf{r}\right) = 0, \tag{1.3.3}$$

where $\mathbf{I}$ is the identity matrix of the same size as $\hat{H}$, and the response to an impulse

$$(E\mathbf{I} - H)\,G\left(\mathbf{r},\mathbf{r}'\right) = \delta\left(\mathbf{r} - \mathbf{r}'\right). \tag{1.3.4}$$

where G should not be confused with the conductance introduced earlier. The Green's function answers the question: given a source term $f(\mathbf{r})$, what is the time-dependent wavefunction of the system? This can be obtained by integrating

$$\psi\left(\mathbf{r}\right)=\int G\left(\mathbf{r},\mathbf{r}'\right)f(\mathbf{r}')d\mathbf{r}', \tag{1.3.5}$$

or by the matrix equation

$$\left|\psi\right\rangle=G\left|f\right\rangle.$$

The response can either consist of wavefunctions that emanate from the impulse or lead up to it. To choose the former and to avoid poles in the complex plane, we apply a small positive η parameter to define the retarded Green's function

$$\left(\left(E+i\eta\right)\mathbf{I}-H\right)G^{\mathrm{R}}\left(\mathbf{r},\mathbf{r}'\right)=\delta\left(\mathbf{r}-\mathbf{r}'\right). \tag{1.3.6}$$

In the real-space representation, $\delta\left(\mathbf{r}-\mathbf{r}'\right)\rightarrow\mathbf{I}$ and we can write

$$G\left(\mathbf{r},\mathbf{r}'\right)=\left(\left(E+i\eta\right)\mathbf{I}-H\right)^{-1}. \tag{1.3.7}$$

In general, we drop the explicit reference to the retarded part of the Green's function.

1.3.2 Green's Function for Infinite and Semi-Infinite Waveguides

Imagine a horizontal waveguide with a set of transverse modes $\chi_m(y)$, ordered by index m (Fig. 1.3.1). Each mode travels down the waveguide with its own wavevector $k_m(E)$ determined by the band structure of the waveguide. The Green's function along an infinite waveguide is then the sum of excitation responses from each of these modes, which can be written as

$$G(x,y,x',y,E)=\sum_m A_m^{\pm}\chi_m(y)e^{ik_m(E)|x'-x|}, \tag{1.3.8}$$

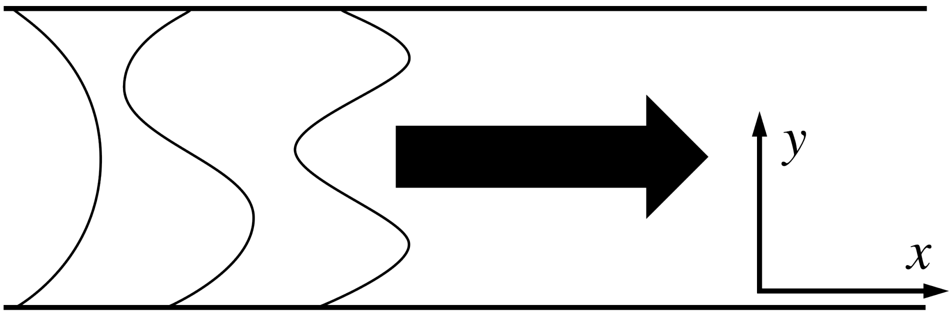

Figure 1.3.1: An unperturbed waveguide is shown with the first three transverse modes $\chi_{1,2,3}(y)$ propagating to the right. More discussion of this geometry and transport modes can be found in Fig. 4.4.7.

where $A_m^{\pm}$ are excitation amplitudes, moving in the positive (+) and negative (−) directions along the x-axis. We can determine the relationship between A_m^+, A_m^-, and $k_m(E)$ by solving for the Schrodinger equation on the points immediately in front of and behind $x = x'$:

$$\left(E + \frac{\hbar^2}{2m}\frac{\partial^2}{\partial x^2} + i\eta\right) G(x, x') = \delta(x - x'). \tag{1.3.9}$$

We solve for

$$A_m^+ = A_m^- = -\frac{i}{\hbar v_m}\chi_m(y') = \frac{-im^*}{\hbar^2 k_m}\chi_m(y'), \tag{1.3.10}$$

where m^* is the effective mass. We then arrive at the solution:

$$G(x, y, x', y', E) = \sum_m -\frac{i}{\hbar v_m(E)}\chi_m(y)\chi_m(y')e^{ik_m(E)|x-x'|}. \tag{1.3.11}$$

The semi-infinite lead imposes an additional constraint, since just beyond its surface the wavefunction must go to zero. In the case of a lattice, we impose this condition at a distance one lattice constant beyond the surface. For the case of a square lattice with lattice constant a, the Green's function at the surface of a semi-infinite lead is given by

$$g(y, y', E) = -\frac{1}{t} \sum_m \chi_m(y) e^{ik_m(E)a} \chi_m(y') \tag{1.3.12}$$

where $\frac{1}{t} = \frac{2\sin(k_m(E)a)}{\hbar v_m(E)}$, a constant. In general, we will be using numerical routines to determine g, since for many of the systems we study, the derivation must be automated under many different system parameters.

1.3.3 The Self-Energy

Given the Green's function for the surface of the semi-infinite lead, we can then derive its coupling to the the device region. We being by considering the Green's function of the system from Eq. 1.3.7. We decompose the Hamiltonian into the central device region H_C, the left lead region H_L, and the right lead region H_R according to Fig. 1.2.1. The off-diagonal component that couples the left lead to the device is written as V_{LC} and $V_{CL} = V_{LC}^\dagger$, where the dagger refers to the Hermitian conjugate, and similarly for the right lead, so that the infinite Hamiltonian can be decomposed into eight sub-units:

$$H = \begin{pmatrix} H_L & V_{LC} & 0 \\ V_{CL} & H_C & V_{CR} \\ 0 & V_{RC} & H_R \end{pmatrix}. \tag{1.3.13}$$

It is then a simple mathematical identity from the decomposition

$$G = \begin{pmatrix} (E + i\eta)\,\mathbf{I} - H_L & V_{LC} & 0 \\ V_{LC}^\dagger & (E + i\eta)\,\mathbf{I} - H_C & V_{RC}^\dagger \\ 0 & V_{RC} & (E + i\eta)\,\mathbf{I} - H_R \end{pmatrix}^{-1} \tag{1.3.14}$$

that

$$G_C = \left(E - H_C - V_{LC}\frac{1}{(E+i\eta)\,\mathbf{I} - H_L}V_{LC}^{\dagger} - V_{RC}\frac{1}{(E+i\eta)\,\mathbf{I} - H_R}V_{RC}^{\dagger} \right)^{-1}. \tag{1.3.15}$$

Because the last two terms on the right-hand side provide a large imaginary contribution, the $i\eta$ parameter associated with H_C is omitted.

Assuming that V_{LC} and V_{RC} only connects lattice sites at the boundary of the lead to the device region (a safe assumption under all applications in this dissertation), we can replace

$$V_{LC}\frac{1}{(E+i\eta)\,\mathbf{I} - H_L}V_{LC}^{\dagger} \rightarrow V_{L_S C}\, g_L^R V_{L_S C}^{\dagger} \tag{1.3.16}$$

where the off-diagonal component $V_{L_S C}$ now projects onto the lead *surface* L_S as opposed to the entire lead region. Thus, we have actually perturbed the device Hamiltonian with a self-energy defined by $\Sigma_L^{\mathrm{R}} = V_{L_S D}\, g_L^{\mathrm{R}} V_{L_S D}^{\dagger}$, allowing us to contract the problem to a finite size

$$H' = H_C + \Sigma_L^{\mathrm{R}} + \Sigma_R^{\mathrm{R}} \tag{1.3.17}$$

so that

$$G_C = \left(E - H_C - \Sigma_L - \Sigma_R\right)^{-1}. \tag{1.3.18}$$

If we imagine a simple finite-difference lattice, $V_{L_S C}$ is a sparse matrix containing the hopping element t at off-diagonal points connecting g_L to the device. Under this assumption, we can write the self-energy in the same form as the semi-infinite Green's function from Eq. 1.3.12:

$$\Sigma_{L(R)}(\mathbf{r},\mathbf{r}',E) = -t \sum_{m\in L(R)} \chi_m(\mathbf{r}) e^{ik_m(E)a} \chi_m(\mathbf{r}') \tag{1.3.19}$$

The real parts of $\Sigma_{L,R}$ indicate what stays within the device, while the imaginary parts indicate which parts are able to propagate.

To understand why, imagine the system propagating in time, governed by the Schrodinger equation $\frac{\partial}{\partial t}\Psi = -\frac{i}{\hbar}H\Psi$. The eigestates of the Hamiltonian H can be obtained from the eigenvalue equation $H\Psi = E\Psi$. In general, states evolve in time according to

$$\psi(t) = e^{-\frac{i}{\hbar}Ht}\psi(t=0),$$

but eigenstates evolve according to

$$\phi(t) = e^{-\frac{i}{\hbar}Et}\phi_0.$$

Thus, real parts of the Hamiltonian cause a phase shift to each eigenstate of H, and the interference of these phases merely rearrange the wave-function amplitude. On the other hand, positive and negative imaginary parts of H cause a given state's probability amplitude to grow or shrink, giving the system sources and drains.

The direction of time is encoded in the Green's function in the choice of sign for the small perturbation $i\eta$ (positive implies forward time propagation, to derive the retarded Green's function, while negative implies backward time propagation, to derive the advanced Green's function). Because each piece of the Hamiltonian is a closed system, we can invert the passage of time by converting all $+i\eta$ to $-i\eta$ in Eq. 1.3.14, that is, by taking the Hermitian transpose of the Green's function. Using this identity, it is straightforward to define a quantity that tells use the net flow into the device: these will be the imaginary part of the retarded self-energy (sources) minus the imaginary part of its Hermitian conjugate (drains). This is summarized by the asymptotic coupling matrix Γ_L defined by $\Gamma_L = \Im\left[\Sigma_L - \Sigma_L^\dagger\right] = 2\mathrm{Im}\left[\Sigma_L\right]$

We can also derive the coupling matrix for the left (right) lead $\Gamma_{L(R)}$ using Eq. 1.3.19 and the definition of t from Eq. 1.3.12 in terms of the asymptotic modes:

$$\Gamma_{L(R)}(\mathbf{r}, \mathbf{r}', E) = \sum_{m \in L(R)} \chi_m(\mathbf{r}) \frac{\hbar v_m(E)}{a} \chi_m(\mathbf{r}'). \tag{1.3.20}$$

1.3.4 Information Inside the Scattering Region

The coupling matrix Γ_{in} for the incoming lead acts as a source term, since it describes the rate of influx for each mode χ_m. Specifically, the source term is

$$S(\mathbf{r}) \propto \sum_{m \in \mathrm{in}} \sqrt{\frac{\hbar v_m}{a}} \chi_m(\mathbf{r}) \tag{1.3.21}$$

since its probability amplitude is $S(\mathbf{r})S^*(\mathbf{r})$. The wavefunction in the system can be determined by applying the Green's function to the source term

$$\Psi(\mathbf{r}) = \int G(\mathbf{r}, \mathbf{r}') S(\mathbf{r}') d\mathbf{r}' \tag{1.3.22}$$

and the density matrix can be derived as

$$\rho(\mathbf{r}, \mathbf{r}') = \Psi(\mathbf{r})\Psi^*(\mathbf{r}') = \int\int G(\mathbf{r}, \mathbf{r}_1) S(\mathbf{r}_1) G(\mathbf{r}', \mathbf{r}_2) S^*(\mathbf{r}_2) d\mathbf{r}_1 d\mathbf{r}_2 = \frac{1}{2\pi} G \Gamma_{\mathrm{in}} G^\dagger. \tag{1.3.23}$$

The density matrix can then be used to extract the individual scattering wavefunctions inside the system, as discussed in Subsection 2.2.5.

If we treat all leads as sources in a single coupling matrix Γ, we can arrive at the customary definition of the local density of states

$$\mathrm{LDOS}(\mathbf{r}) = \frac{1}{2\pi}\left[G\Gamma G^\dagger\right]_{\mathbf{r},\mathbf{r}} = \frac{1}{\pi}\mathrm{Im}\left[G\right]_{\mathbf{r},\mathbf{r}}, \tag{1.3.24}$$

since $\Gamma = 2\mathrm{Im}\left[\Sigma\right]$ and the imaginary parts of Σ are the only parts that contribute to the imaginary part of G.

The current density map

$$\mathbf{j} = \frac{e}{2m}\left(\Psi\hat{p}\Psi^* + \Psi^*\hat{p}\Psi\right) = -\frac{ie\hbar}{2m}\left(\Psi\nabla\Psi^* + \Psi^*\nabla\Psi\right) \tag{1.3.25}$$

can now be written in terms of the density matrix as

$$\mathbf{j}(\mathbf{r}) = -\frac{ie\hbar}{2m}\left[\left(\nabla - \nabla^\dagger\right)\rho\right]_{\mathbf{r},\mathbf{r}}, \tag{1.3.26}$$

where ∇ is a matrix operator.

1.3.5 A Matrix Algebra Formulation of the Scattering Matrix

The relations found in the previous section allow us to complete a simple linear-algebraic formalism for the scattering matrix. We begin by writing the scattering matrix in terms of the modes and the Green's function as

$$s_{nm} = -\delta_{nm} + \frac{i\hbar\sqrt{v_n v_m}}{a}\int\int \chi_n(\mathbf{r}_1)G^{\mathrm{R}}(\mathbf{r}_1,\mathbf{r}_2)\chi_m(\mathbf{r}_2)d\mathbf{r}_1 d\mathbf{r}_2 \tag{1.3.27}$$

which provides us the probability amplitude by which an asymptotic wave-function in one mode moves to the other asymptotic modes over an infinite time scale.

A few notes about the terms here. The scattering matrix has units of unity. The factor preceding the integral has units of energy, and by its definition, the Green's function has units of inverse energy, so that the two factors cancel each other out in dimensional analysis. The delta function exists to maintain unity of the scattering matrix by anticipating the effect of double-counting the reflection probability. For instance, in the case where a mode scatters back to itself, the second term in Eq. 1.3.27

integrates twice over the mode whose integrated amplitude is unity. The value of the second term is then set to 2, and the delta function ensures that $s_{nn} = 1$.

To obtain the full scattering matrix in linear-algebraic terms, Eq. 1.3.27 is reformulated as

$$s = i\Gamma^{1/2} G \Gamma^{1/2} - \mathbf{I}, \tag{1.3.28}$$

where $\mathbf{I}$ is the identity matrix of the size of the central region. A key observation here is that just like the $-\delta_{nm}$ term in equation 1.3.27, the identity matrix in Equation 1.3.28 affects only the reflection matrix, and relies on the assumption that Γ can be diagonalized into orthogonal vectors. This is because taking the square root of a matrix is identical to diagonalizing the matrix, taking the square root of its eigenvalues, and then reconstructing the matrix from its eigenvectors and the new eigenvalues. For most of the thesis, this assumption is held, but in Chapter 3, we will break the assumption and find another solution which gives the desired result.

There is an ambiguity in Eq. 1.3.28: there are actually two solutions to the square root of a real matrix like Γ, and so the above definition is ill-defined by a factor of -1. However, when probabilities are measured, as opposed to their amplitudes, only the square of the result ($S = ss^\dagger$) is used.

Thanks to the engineering applications of Landauer-Buttiker, there is a well-developed field of numerical methods for calculating the energy-dependent Green's function for semi-infinite leads, in particular, the methods developed by Lopez-Sancho and Rubio[18, 19]. Such methods are extremely helpful for lattices like the honeycomb lattice where analytical solutions to the modes in the leads may not be available. By the above identities, these numerical methods can also give us the set of open and closed asymptotic modes χ_m at each energy, their coupling matrices Γ to the device region, and their band structures. In general, these applications are interested in calculating the sum of absolute squared scattering matrix elements from one set of modes that are spatially separated from another set of modes, that is,

$$T = tt^\dagger = \sum_{n \in \text{in}, m \in \text{out}} |s_{nm}|^2 = \sum_{n \in \text{in}, m \in \text{out}} S_{nm}. \tag{1.3.29}$$

The Landauer formula (Eq. 1.2.1) gives the proportionality between T and the conductance across the device in the linear regime (See Sec. 1.2), and is the basis of a wide range of studies into condensed matter systems. Buttiker later generalized the formula to systems with more than two leads[20], and now many papers use the Landauer-Buttiker [17, 20]formula

$$T = \text{Tr}\left[\Gamma_{\text{in}} G \Gamma_{\text{out}} G^*\right], \tag{1.3.30}$$

which makes use of matrix identities to reduce the problem to the trace of the product of the coupling matrices and the Green's function of the device. The elegance and fool-proofness of this formula, along with it's direct physical intuition, are responsible for its wide popularity.

Chapter 2

Outward Wave Algorithm

In this chapter we describe a method for computing the electron transport properties of graphene systems with arbitrary geometries. We are motivated by recent experiments that have stepped outside the realm of linear, rectangular MOSFET-type devices and into fully two-dimensional geometries with multiple leads at arbitrary angles [21, 22, 23]. Challenges to graphene fabrication give even linear devices substantial two-dimensional character, largely due to unpredictable defects in the etching process[24, 25]. Moreover, novel applications for graphene have been recently proposed using spin polarization that explicitly relies on irregular geometries [26]. The current gap between theory and experiment in the literature can be attributed to the lack of efficient computational tools to handle such arbitrary devices at the nano- and meso-scopic scales.

This paper addresses these problems and outlines an algorithm that generalizes the well-known recursive Green's function (RGF) method outlined by Datta[27] by incorporating the reverse Cuthill-McKee algorithm for connected graphs[28]. By reinterpreting the Landauer-Buttiker formalism, we demonstrate that RGF can work for systems that do not fit an input-system-output schematic, expanding the fruits of algorithmic advances in transmission calculations to the general scattering matrix problem. Like RGF, our algorithm can also produce the local density of states (LDOS) at a comparable computational cost.

One important aim for this chapter is to produce and explain a method that is straightforward to implement and does not require cumbersome external software packages. Accordingly, each calculation is performed using the standard BLAS and LAPACK dense matrix algebra routines[29] which come pre-installed on nearly all scientific machines today. Comparisons to sparse matrix packages like SuperLU[30] are discussed in Section 2.3.4.

2.1 Background

2.1.1 Hamiltonian and Formalism

The methods used in this chapter apply to Hamiltonians with sparse character (composed of many off-diagonal zeros) and poses some order of localization, that is, one part of the Hamiltonian doesn't couple to another distant part. For instance, for all of our calculations we will be using the general single-orbital nearest-neighbor tight-binding Hamiltonian from Eq. 1.1.1. These methods are quite general since the structure of this Hamiltonian is very similar to any finite-difference continuous wave equation sampled on a lattice of any character. Moreover, recursive methods apply to all other orders of tight-binding and finite-difference approximations, such

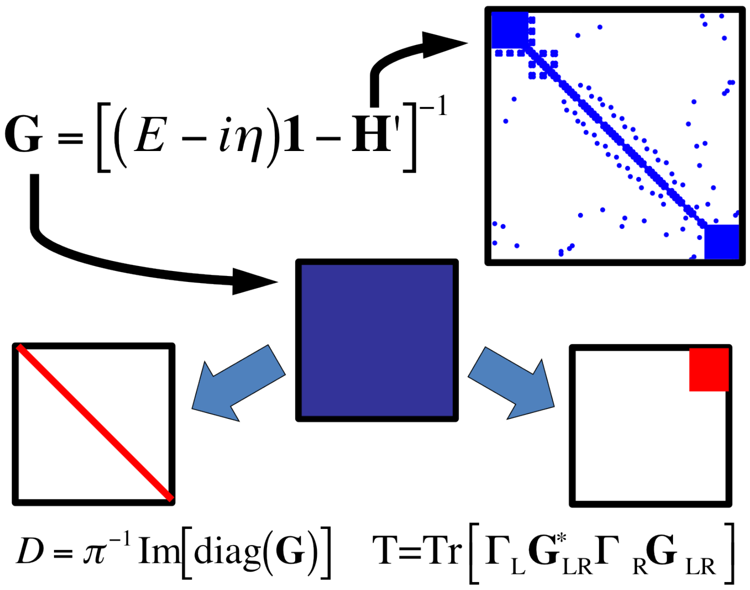

Figure 2.1.1: While the Hamiltonian is sparse, the Green's function is dense. However, only a few parts of the Green's function are needed to calculate the local density of states and the transmission function, indicated in red for the left-to-right regime. Once the Hamiltonian is permuted according to the algorithm in this chapter, the relevant parts of the Green's function shift (Fig. 2.2.3)

as nearest-nearest-neighbor tight-binding, although their efficiency will drop for increasing orders.

The reader is encouraged to review the background of scattering matrix calculations in Section 1.3. The Hamiltonian describing the infinite system can be contracted onto a finite basis using the retarded self-energy of the leads $\Sigma(E)$ according to

$$H'(E) = H_C + \Sigma(E)$$

which has the same dimension as the central (finite) region. Because H_C describes the central region as a closed system, it is Hermitian. Accordingly, H' is Hermitian except where there are contributions from the self-energies of the leads (See Fig. 2.1.1).

Using the definition of the Green's function

$$G(E) = \left[E \cdot \mathbb{I}_C - H'(E)\right]^{-1}, \tag{2.1.1}$$

we identify the local density of states as

$$D(E, n) = \frac{1}{\pi} \mathrm{Im}\left[G_{n,n}(E)\right] \tag{2.1.2}$$

That is, the local density of states is encoded along the diagonal entries of the full retarded Green's function of the system (See Fig. 2.1.1). From here on out, we omit the explicit energy dependence in G.

The transmission matrix is calculated not from entries of G along the diagonal but from the off-diagonal elements communicating information from the input to the output boundaries. Even though these boundaries can be general, we choose to use the familiar two-terminal nomenclature, so that we write the relevant sub-matrix as G_{LR} (See Fig. (See Fig. 2.1.1). The incoming and outgoing wavefunctions for each mode can then be represented by the matrix square-root of the coupling matrix for the left (right) lead $\Gamma_{L(R)}$, and the transmission function between the left and right leads can be written as a matrix

$$t = \sqrt{\Gamma_{\mathrm{L}}} G_{\mathrm{LR}} \sqrt{\Gamma_R} \tag{2.1.3}$$

In the linear regime, conductance through the system will be proportional to the sum-squares of transmission functions for each incoming mode. Trace identities then produce the transmission probability[31]

$$T(E) \propto \mathrm{Tr}\left[T\right] = \mathrm{Tr}[tt^\dagger] = \mathrm{Tr}\left[\Gamma_L G^*_{LR} \Gamma_R G_{LR}\right]. \tag{2.1.4}$$

2.1.2 Full Inversion

The most straightforward calculation of the LDOS and transmission matrix involves first inverting the entire matrix $M = E \cdot \mathbb{I}_C - H'$ and then projecting out the diagonal elements of G for the LDOS and the sub-matrix G_{LR} for the transmission matrix. As is well known, the time to compute the inverse of a matrix with N rows and columns scales as N^3. Moreover, the sparse systems this chapter addresses invert to dense matrices, adding a memory cost that scales by N^2. Such large scaling factors make this calculation prohibitively costly for systems on the order of thousands of atoms.

A shortcut to calculating the LDOS and transmission can be made by solving a set of linear equations $M\mathbf{x_i} = \hat{e}_{i,C}$ where $\hat{e}_{i,C}$ is a unit vector of size C with unity on the basis index i. Solving for the diagonal entries then requires solving for $\mathbf{x}_i$ for all $i \in [1, N]$. Such calculations can be aided by sophisticated sparse matrix software packages which cut the number of operations by permuting the matrix columns and rows, and many different approaches are outlined in [29]. Solving for all the diagonal entries, however, requires one to solve for N separate systems of equations, which makes these approaches less efficient than one would hope. For instance it can be shown that nested-dissection methods[32] can under optimal circumstances return the inverse with scaling of order $N^2 \log N$ after a re-ordering operation whose cost grows with some function of N. This is better than N^3 but still worse than N^2 as promised by the linear recursive Green's Function method.

2.1.3 Linear Recursive Green's Function Method

To reduce the computational footprint of LDOS and transmission calculations, the recursive Green's Function method was developed. In its usual implementation, the recursive Green's Function method operates on a Hamiltonian that satisfies the following three conditions:

1. An input lead contributes the boundary condition Σ_L from the left (incoming)
2. An output lead contributes the boundary condition Σ_R from the right (outgoing)
3. A linear device rests in between the leads, which can be divided into N vertical slices referred to as "primary layers", which we number in increasing order from left-to-right.

While the particular expression of this topology can be distorted, the means of calculation is always the same, and assumes that the system can be mapped onto a linear chain of primary layers. Accordingly, we refer to it as the linear recursive Green's Function method, or LRGF. In LRGF, one employs the Dyson equation, which is derived from partial block inversion, to move left-to-right along the primary layers (see, for example, [27, 33]). In fact, LRGF performs partial block inversion on the tridiagonal matrix

$$M = \begin{pmatrix} H'_1 & H'_{12} & & & \\ H'_{21} & H'_2 & H'_{23} & & \\ & H'_{32} & \ddots & \ddots & \\ & & \ddots & H'_{N_L-1} & H'_{N_L-1,N_L} \\ & & & H'_{N_L,N_L-1} & H'_{N_L} \end{pmatrix} \qquad (2.1.5)$$

where H'_i is the system Hamiltonian H' projected at the primary layer i. The partial-block inversion algorithm is outlined in the next section.

2.1.4 Block Inversion

To demonstrate the block inversion algorithm, we rewrite

$$M = \begin{pmatrix} M_1 & M_{12} & & \\ M_{21} & M_2 & \ddots & \\ & \ddots & \ddots & M_{N_L-1,N_L} \\ & & M_{N_L-1,N_L} & M_{N_L} \end{pmatrix} \tag{2.1.6}$$

and employ Algorithm 2.1.

The first for-loop (Step 2) returns the inverse $G_{N_L} = (M^{-1})_{N_L}$ at the bottom-right-most block (see Step 4). The second for-loop (Step 6) returns the set of block inverses along the diagonal: $G_i = (M^{-1})_i$ of sizes $\{N_i | \sum_i N_i = N\}$. From these blocks one can obtain the diagonal elements of M^{-1} and thus the LDOS. The efficiency of this algorithm scales $\leq \max_i N_i^3 N_L$ and in the case of a square device, where $\{N_i\} \sim N_L \sim \sqrt{N}$, it can scale with N^2, a vast improvement over full inversion when only the diagonal entries are required. A further extension allows us to calculate any block of the inverse off the diagonal, but at the cost of additional operations (see Cauley et al. [34]). For LRGF, calculating G_{LR} requires us to calculate the inverse at the far upper-right block $(M^{-1})_{1,N_L}$ and an additional step in the first for-loop can compute this block while minimizing memory allocation (see Datta [27]).

Algorithm 2.1 Diagonal-block-inversion for block-tridiagonal matrix

```
1. $g_1^L = M_1^{-1}$
2. for $i = 2$ to $N_L$
    (a) $\Sigma_i^L = M_{i,i-1} g_{i-1}^L M_{i-1,i}$
    (b) $g_i^L = \left(M_i - \Sigma_i^L\right)^{-1}$
3. end for
4. $G_{N_L} = g_{N_L}^L$
5. $g_{N_L}^R = M_{N_L}^{-1}$
6. for $i = N_L - 1$ to 1
    (a) $\Sigma_i^R = M_{i+1,i} g_{i+1}^R M_{i,i+1}$
    (b) $g_i^R = \left(M_i - \Sigma_i^R\right)^{-1}$
    (c) $G_i = g_i^L \left(\mathbb{I}_i - \Sigma_i^R g_i^L\right)^{-1}$
7. end for
```

2.2 The Outward Wave Method

For linear systems satisfying the conditions of LRGF (see Section 2.1.3) the block-tridiagonal nature of $M = E \cdot \mathbb{I}_C - H'$ is evident: one simply slices the device into vertical sections, from left-to-right. However, this is not the case for general geometries even though many Hamiltonians are sparse and exhibit a similar structure. In order to take advantage of the computational efficiency of LRGF, one must find a way to map the system geometry onto a linear chain,

Literature through the past two decades describes many inventive methods to accomplish precisely this goal. Among those methods are a conformal map to transform a quasi-circular system onto a linear chain, using continuous eigenfunctions as their basis[35], and a unique geometry for applying LRGF to four-terminal devices[36]. More recent work on the contact-block reduction method [37] divides a generic device into smaller blocks which are pieced together like a jig-saw puzzle. In addition, graph theory has been used to develop a relatively elaborate system permitting the use of LRGF with generic boundary conditions[38]. These results, along with others[39], suggest the approach we explore in depth in this chapter, however we argue that the formalism of the "virtual lead" is not necessary. Our formalism, in addition, opens the Landauer-Buttiker formalism to tractable reflection matrix calculations as described in Section 2.2.5.

2.2.1 Reverse Cuthill-McKee

Given any sparse matrix A, the Reverse Cuthill-McKee (RCM) algorithm[28] automatically calculates a permutation matrix P so that PAP^T produces a block-tridiagonal matrix, which enables us to use the LRGF method. The only requirement for RCM is that the matrix A satisfy the properties of an adjacency matrix, which describes the edges between vertices of an undirected graph. This is satisfied when the non-zero entries of a matrix are symmetrically distributed across the diagonal, and is therefore satisfied for any Hermitian Hamiltonian. Since the tight-binding and similar localized models create Hamiltonians that describe actual graphs, where nodes map onto atomic orbitals and edges onto overlap functions which are distributed in physical space, RCM is ideal for such systems.

RCM aims to minimize the distance of non-zero entries to the diagonal, which makes it a "bandwidth minimization" algorithm and ideal for our purposes. This is because the most computationally expensive step in an LRGF calculation constitutes inverting each individual block, and this time is dependent upon the cube of number of rows N_i for each block. However, we are constrained by the fact that the number of rows for each block must add up to the number of rows in the entire system, that is, $\sum_i N_i = N$. We can write a rough optimization function $\sum_i N_i^3$ which describes the time of calculation. This optimization function is minimized when the number of blocks is maximized, and the size of each block is reduced. Ideally, no block is especially large compared to the others, since the cubic function grows rapidly.

RCM is able to reduce block sizes by keeping track of site indices while propagating through the system like a wave propagates on a pond surface. It begins by taking a seed of indices S_1, which constitute a set of nodes in the graph represented by A. RCM then calculates which nodes share an edge with nodes in S_1 and saves their indices as S_2. In the second iteration, it computes the set of nodes connected to S_2 but eliminates any nodes it has previously visited, and saves the result to S_3. These steps are repeated until the entire system has been explored. For a locally connected graph like a single-orbital tight-binding model, the RCM technique will actually appear as a wave that emanates from the seed until it has filled the entire system.

To give the reader a precise account of RCM, we describe it in terms of the matrix A and its indices in Algorithm 2.2.

2.2.2 Applying RCM on a Model System

We demonstrate how the RCM algorithm would apply to a model system which consists of just six sites arranged in a ring as depicted in Figure 2.2.1. This geometry is

Algorithm 2.2 Reverse Cuthill-McKee

```
1. define $S_1, i = 2$
2. while $S_{i-1} \neq \emptyset$
    (a) define $S_i$ as the indices of the columns of the off-diagonal elements in the rows $S_{i-1}$
    (b) $S_i = S_i / \{S_j | j = 1, \ldots, i-1\}$ that is, eliminate the indices that have been visited previously
    (c) $i = i + 1$
3. end while
4. reverse subscripts of $\{S_i\}$
```

one of the simplest diversions from a linear topology, and we can write the Hamiltonian for this system as

$$H = \begin{pmatrix} \epsilon_1 & t & 0 & 0 & 0 & t \\ t & \epsilon_2 & t & 0 & 0 & 0 \\ 0 & t & \epsilon_3 & t & 0 & 0 \\ 0 & 0 & t & \epsilon_4 & t & 0 \\ 0 & 0 & 0 & t & \epsilon_5 & t \\ t & 0 & 0 & 0 & t & \epsilon_6 \end{pmatrix}$$

where $\epsilon_{1\ldots6}$ are on-site potentials and t is the hopping element between neighboring sites. If the sites were arranged in a straight line, the Hamiltonian would be trivially block-tridiagonal. But because the sites are now arranged in a ring, the two hopping-terms in the extreme off-diagonals break this property. To compute H^{-1} at site 1, one might naively invert the entire 6×6 matrix, with an associated 6^3 scaling.

To resolve this, RCM begins with a seed index and moves out through the system,

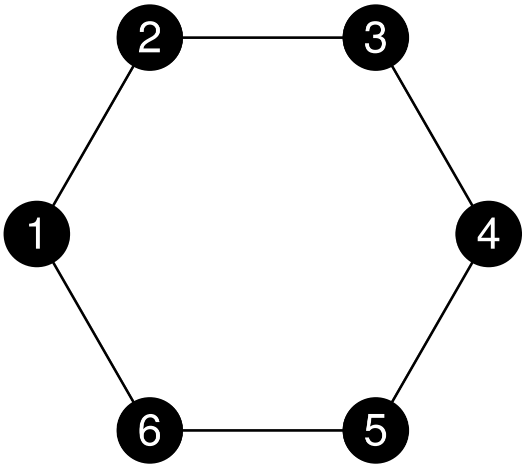

Figure 2.2.1: The six sites of a model nearest-neighbor tight-binding system are shown with index labels. Lines between sites indicate off-diagonal entries in the Hamiltonian

keeping track of indices along the way. If we set the seed to site 1, RCM would obtain a series of indices $S_1 = \{1\}, S_2 = \{2, 6\}, S_3 = \{3, 5\}, S_4 = \{4\}$, which allows us to construct a permutation matrix by placing 1's in a zero-matrix. As we move down each row we place a 1 in a column that matches an index in one of the RCM sets, beginning with S_1, then S_2 and so on. The order within each set doesn't matter. For example, the above construction would give us

$$P = \begin{pmatrix} 1 & 0 & 0 & 0 & 0 & 0 \\ 0 & 1 & 0 & 0 & 0 & 0 \\ 0 & 0 & 0 & 0 & 0 & 1 \\ 0 & 0 & 1 & 0 & 0 & 0 \\ 0 & 0 & 0 & 0 & 1 & 0 \\ 0 & 0 & 0 & 1 & 0 & 0 \end{pmatrix}$$

by which we can then compute

$$H' = PHP^T = \begin{pmatrix} \epsilon_1 & t & t & 0 & 0 & 0 \\ t & \epsilon_2 & 0 & t & 0 & 0 \\ t & 0 & \epsilon_6 & 0 & t & 0 \\ 0 & t & 0 & \epsilon_3 & 0 & t \\ 0 & 0 & t & 0 & \epsilon_5 & t \\ 0 & 0 & 0 & t & t & t\epsilon_4 \end{pmatrix}$$

The bandwidth of the Hamiltonian has been reduced, converting it into a 4×4 block-tridiagonal form. The Hamiltonian is then reversed in accordance with Algorithm 2.2 Step 4 by a final permutation using

$$P = \begin{pmatrix} 0 & 0 & 0 & 0 & 0 & 1 \\ 0 & 0 & 0 & 0 & 1 & 0 \\ 0 & 0 & 0 & 1 & 0 & 0 \\ 0 & 0 & 1 & 0 & 0 & 0 \\ 0 & 1 & 0 & 0 & 0 & 0 \\ 1 & 0 & 0 & 0 & 0 & 0 \end{pmatrix}$$

2.2.3 Using RCM to Block-Invert an Open System

Here we explore the role of the seed in RCM. For a given system, the optimization of RCM is entirely determined by this choice. But because block-diagonal inversion using RCM only produces blocks along the diagonal, which entries we need to calculate will also affect our choice. For instance, if only the diagonal entries of the Green's function matrix are needed, then any seed will suffice because these entries

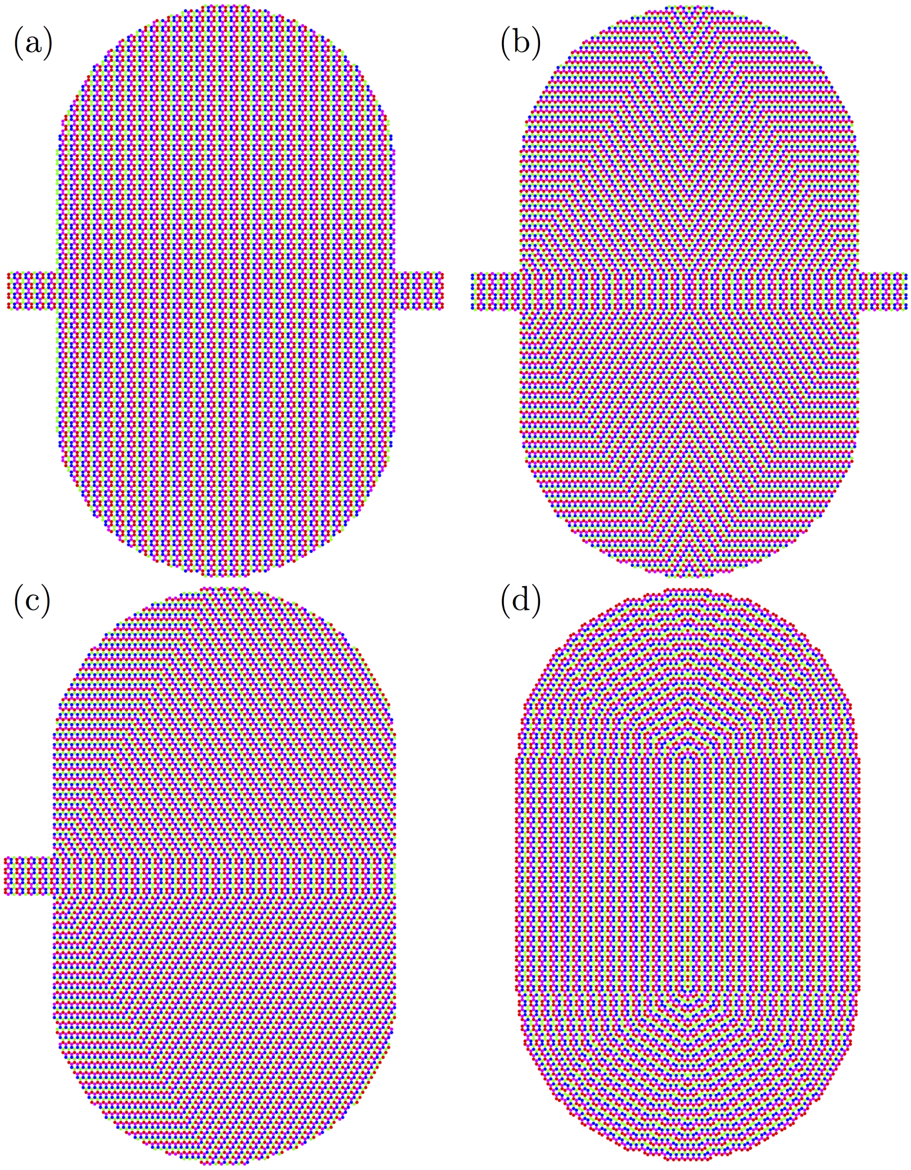

Figure 2.2.2: Recursive Green's function methods demonstrated on a nearest-neighbor single-orbital tight-binding Hamiltonian for a graphene stadium. Each block of the Hamiltonian is represented by different colors of atoms. In (a) and (b), we have a common two-terminal left-to-right system. In (a) the recursive algorithm is determined by LRGF, and in (b) by the Outward Wave method. In (c), a single lead enters from the left for studying the full scattering matrix of reflected wavefunctions, as described in Section 2.2.5. In (d), the Outward Wave method is applied to an ensemble situation, in which the entire boundary of the device region is treated as a potential location for attaching a lead, as described in Section 2.2.4.

will always be returned by the inversion algorithm. We could even sample different seeds to see which would provide the most efficient permutation, although this process could prove computationally expensive. When a transmission calculation is required, however, there is an additional restraint to LRGF: the sub-matrix of the Hamiltonian describing coupling of the system to the environment is a dense matrix because of the contribution from the self-energy. Since we also need to produce all of these entries from the full inversion, it is necessary then to choose this as our seed.

The LRGF technique circumvents some of these restrictions by adding an additional step that permits block inversion to produce entries at the extreme diagonal block which conveys information from the input lead to the output lead. RCM could be adapted to this calculation by setting the seed to the input lead, and propagating to the output seed. For any system that deviates from a simple linear topology, however, we run into problems. As soon as a single index in the RCM routine is a member of the output boundary, the fact that the Hamiltonian for the output boundary is dense requires that all remaining indices be contained in the final block, which can result in an unnecessarily large block to invert. In fact, this very limitation was argued by Wimmer and Richter[38] as the motivation for developing their automatic procedure.

We instead propose to set the seed as the collective boundary between the central region and *all* the leads. The first for-loop in Algorithm 2.1 will then provide us the Green's function at the boundary G_{B}. This block is useful for transmission calculations since it automatically contains the off-diagonal entries corresponding to G_{LR}.

In fact, G_B can be permuted as

$$G_B = \begin{pmatrix} G_L & G_{LR} \\ G_{RL} & G_R \end{pmatrix} \tag{2.2.1}$$

Since the boundaries between a device and its leads generally lie at the device perimeter, RCM will first search into the interior of the device from the boundary regions at the perimeter. When this search is reversed as in the last line of Algorithm 2.2, RCM will produce a set of layers that appear to emanate from the interior of the device and radiate toward the leads. In the final step, the waves will converge upon the leads at the same time. We explore several geometries where this happens in Figure 2.2.2. Because of the appearance of the set of indices as an outward-moving wave, we call the techniques described in this chapter as the Outward Wave Method.

2.2.4 Application to Ensembles

For an ensemble of systems where the interior of each system is identical, but only the coupling to the environment changes, we can choose the seed wisely to enhance efficiency over the whole ensemble. This can be accomplished by defining the seed as the set of all possible boundaries in the ensemble. Potential applications include examining the response of a single device to varying lead geometries, which will attach at different points along the device perimeter.

We demonstrate this application by assuming that we have a device where we have set the seed at its entire perimeter. The first for-loop in Algorithm 2.1 will provide us the Schur complement at the penultimate block Σ^L_{N-1} (see Step 2a of Algorithm 2.1). For each member in the ensemble, this Schur complement will stay the same while the lead self-energy Σ^r, and thus H'_B, changes. We can then calculate for each member

$$G_B = \left(H'_B - E - \Sigma^L_{N-1}\right)^{-1} \tag{2.2.2}$$

which provides us the transmission information by Equation 2.1.4. Performing this one inversion over the device perimeter saves considerable computational time over the ensemble, enabling the examination of vast arrays of device-plus-lead ensembles.

2.2.5 Extension to the Reflection and Density Matrices

In systems in which the entire wavefunction is reflected, there is no distinction between and input and output boundary. While the total reflection coefficient is of course unity at all energies, mixing between the modes can be of scientific interest, for instance, when examining quantum ergodicity (see Kaplan and Heller[40] for an application to the tilted billiard). In this case, there is no alternative available to full matrix inversion, except for sparse matrix routines like SuperLU[30]. For full scattering matrix calculations of this variety, the Outward Wave method contributes an efficient dense-matrix algebra equivalent.

For the full scattering matrix, it is not sufficient to simply derive

$$r = i\sqrt{\Gamma_L} G_B \sqrt{\Gamma_L} - \mathbf{I}$$

according to the analysis in Chap. 1, since the coupling matrix Γ_L cannot generally be diagonalized into orthogonal modes along the boundary. In Chap. 3, we explore methods for resolving this issue and extending the Outward Wave method to the full scattering matrix.

However, the formalism for obtaining the transmission function doesn't need a diagonalizable coupling matrix. Is there a use for a transmission matrix using the same lead for both the incoming *and* outgoing coupline matrix, that is, $t_L = \sqrt{\Gamma_L} G_B \sqrt{\Gamma_L}$? Yes: this problem maps onto calculating the transmission across an infinite waveguide, where perpendicular to the waveguide is attached the equivalent device region. An example of this geometry is depicted in Figure 2.3.4. Such geometries are similar to that of a Helmholtz resonator, where current flow is absorbed by the resonator at some energies and enhanced at others, as a result of interference between the direct wavefunction and the wavefunction reflected in the resonator. We use this calculation to contribute to the physical picture of a Fano resonance in Section 2.3.3.

Extensions to the Outward Wave method can produce other quantities of interest. For instance, the density matrix from Eq. 1.3.23 is derived from

$$\rho = \frac{1}{2\pi} G \Gamma_L G^\dagger,$$

where Γ_L is the coupling matrix for the incoming lead. Because the coupling matrix is only defined on the boundary, the density matrix only has rank as high as the number of sites along the boundary where the incoming lead touches the scattering region. In fact, only a small part of G is needed to compute the density matrix – the vertical (or horizontal) column incident with the boundary.

For this reason, when calculating the scattering wavefunctions, which are eigenstates of the density matrix ρ, it is much more efficient not to diagonalize the entire matrix, but to apply a singular value decomposition (SVD) such that

$$\sqrt{\Gamma_L} G^\dagger = U^\dagger \Sigma V.$$

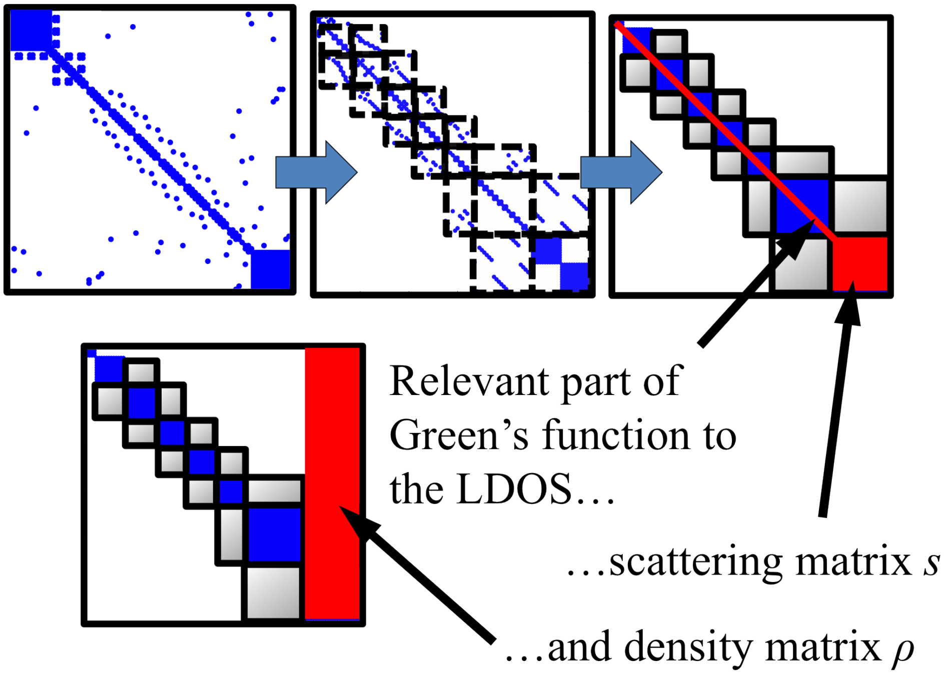

Figure 2.2.3: Only certain parts of the Green's function need to be retrieved for each metric used in this thesis, and they are premuted from the left-to-right geometry in Fig. 2.1.1. At top, a sparse Hermitian Hamiltonian is perturbed by dense self-energy contributions from the leads (blue squares, left). The Outward Wave Algorithm permutes this matrix into block tridiagonal form, and then inverts it piece by piece (middle). Only the diagonal and final block are needed for the LDOS and the scattering matrix s. The density matrix ρ, which is used in Chapters 4 and 5, only needs the vertical block at the boundaries.

The columns of U contain the source terms for each wavefunction (See Subsection 1.3.4), and the columns of V contain the scattering wavefunction inside the bulk. By limiting the SVD routine to only compute as many decompositions as there are lattice sites at the coupling region, extracting the scattering wavefunctions can be made enormously more efficient.

Because the boundary is often much smaller than the system as whole, this part of the Green's function is still manageable, and better still, it can be calculated by inserting an additional step in the Outward Wave algorithm, resulting in only a modest increase in calculation time. We summarize our results in Fig. 2.2.3, showing that only certain parts of the final Green's function are needed for the quantities relevant to this thesis.

2.3 Computational Experiments

We demonstrate the efficacy of our algorithm on a demonstration graphene system: the "relativistic stadium" geometry, which was first explored by Huang et al. [41]. We choose the single-orbital tight-binding model for graphene described in Equation 1.1.1 as our basis since it is the current *de facto* standard for computer simulations on graphene of this type (see, for example, Munoz-Rojas et al.[42]) and is the model used in the reference[41].

2.3.1 Relativistic Stadium

To validate our code, we compare our transmission results with those of Huang et al. in Figure 2.3.1. In addition, we compared our results among full inversion, LRGF, and Outward Wave methods and achieved identical results within machine precision. Compared to the published data, which we have sampled numerically from their article, we find that we achieve nearly-identical results for the system, except near singularities in the density of states, which appear as sharp transmission fluctuations. A close examination reveals that these deviations are numerical artifact partly as a consequence of choosing slightly different sampling points in the energy spectrum. Near singularities, even slight differences in where we sample the energy spectrum will have a significant impact on the reported value, making it very difficult to align with

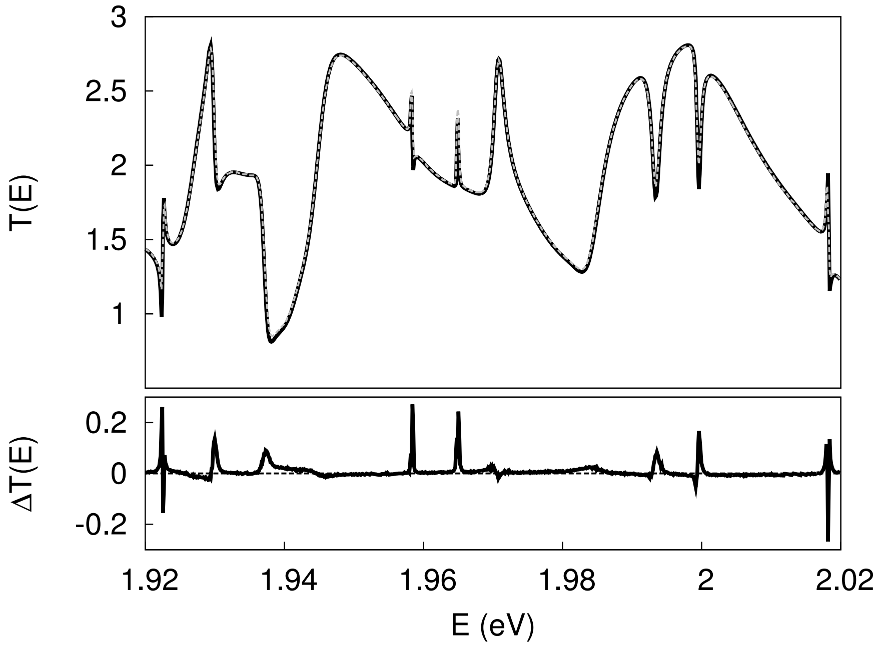

Figure 2.3.1: Transmission coefficient for the graphene stadium[?] using the Outward Wave method (black) and the original data (grey dashed). Differences between the two data are shown at bottom. Deviations arise from disparities in sampling points and the infinitesimal η parameter. We publish results for a very small η parameter of 2.7×10^{-5}eV.

the published results exactly. The broader differences, most notably near E=1.938eV and 1.985eV can be accounted for by another numerical artifact: a discrepancy in the size of the infinitesimal η parameter in calculating the self-energies of the leads. Since the value chosen in the original article is not published, and solutions approach an asymptote with smaller η parameters, we have chosen to present our results using a relatively small η parameter of 2.7×10^{-5}eV.

2.3.2 Relativistic Stadiums of Various Sizes

For a linear system in which the length of the boundary region is comparable to the width along each segment of the system, LRGF actually offers a factor of 4 improvement in efficiency over the Outward Wave method. Even though there are twice as many sub-matrices to invert in this case, each sub-matrix is now half the size compared to the Outward Wave method, that is, $\sum_{m=1}^{N_L} N_m^3 \to \sum_{m=1}^{2N_L} \left(\frac{1}{2}N_m\right)^3 = \frac{1}{4}\sum_{m=1}^{N_L} N_m^3$. There is a cross-over point, however, where each block in Outward Wave is equal to or smaller than the sub-matrices in an equivalent LRGF calculation. This occurs when the minimum distance between the input and output boundaries, L, satisfies

$$L \leq \frac{N}{2N_B}$$

where N is the number of basis functions in the device and N_B is the number of basis functions along the boundary.

To test this, we created an ensemble of 40 relativistic stadiums. Each has the same radius at the rounded edges of $30a$ where a is the lattice constant of graphene. However, the length along the straight section was varied by a linear function according to the system size parameter. We benchmarked fifty energy points within the spectrum of 1.92 and 2.02 eV using the Harvard Odyssey cluster with dual Xeon E5410 2.3Ghz quad core processors. The results of our benchmarks appear in Figure 2.3.2. Most prominently, we find the cross-over point between LRGF and Outward Wave to occur around a system size parameter of 12. For our largest system, we found over a 100-fold improvement for the Outward Wave method over the linear recursive method.

We expected the calculation time for full inversion to be the largest of the three methods, and to fail above a certain system size parameter because of memory requirements, which we find in our results above a system size parameter of 25. The

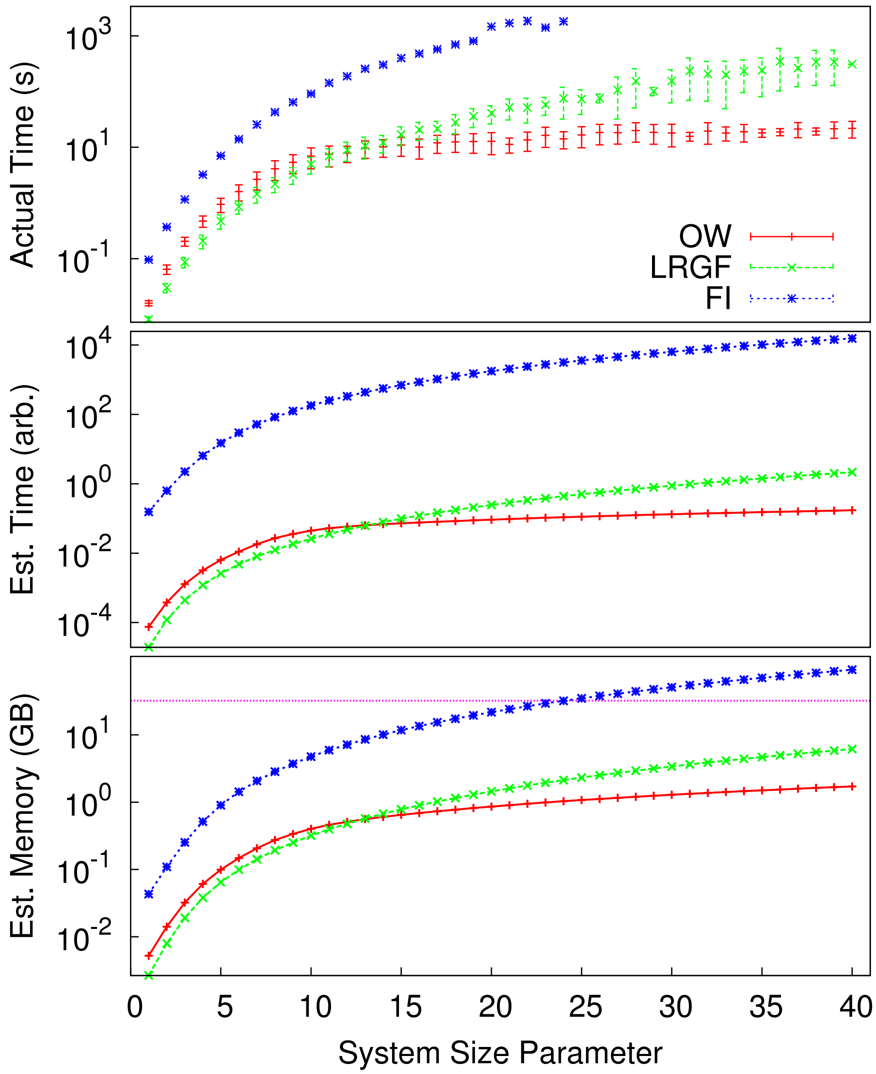

Figure 2.3.2: Top: Time of calculation for a single energy point for relativistic stadiums using full inversion (blue stars), LRGF (green crosses), and the Outward Wave method (red pluses). Standard deviations above and below are indicated by whisker bars. Middle: Estimated time for transmission calculations, in arbitrary units, computed from the optimization function discussed in Section 2.2.1. Bottom: Estimated memory requirements for each system. The clusters we used had a memory limit of 16GB, which is indicated by the magenta dotted line. Our simulations suggest that the memory estimation for LRGF and the Outward Wave method are undervalued. For the transmission calculation, all three methods returned the same transmission coefficient at the energy point within the precision of the machine. The number of basis functions in each calculation is a linear function of the system size parameter.

reduction in variance is partly explained because memory allocation is a major source of variance in these calculations. All recursive methods require that each sub-block be allocated to memory, and as these blocks grow larger, the relative allocation time also grows (which is shown in the other methods). For nodes with shared memory, interference in this step can be a significant factor. The full inversion method, on the other hand, only requires one allocation. In addition, the load balancer is likely shifting these calculations to nodes with identical processors but different priorities, which suggests the results for full inversion would actually be larger than what we report if all of our simulations ran on identical nodes. Happily, this would open the gap between the methods in terms of efficacy even further.

Above a system size parameter of 19, many of our time trials for the full inversion method failed. As a result, our times show a stark bump in value. To understand this, we estimated the memory requirements for each method by allocating a double-precision complex number for every element of the matrices used. We show our results in Figure 2.3.2. The clusters we used had a memory limit of 16 GB, which is indicated by the magenta dotted line. Our predictions are consistent with the bump in time trials for full inversion, since above a system size parameter of 19, the cluster would run out of memory and rely on virtual memory on the hard disk.

In addition, Figure 2.3.2 demonstrates the memory benefits of recursive methods in general, but especially the Outward Wave method when a system is large compared to the distance between its input and output boundaries. Memory use becomes especially important considering the memory challenges we faced for full inversion.

Time trials using the LRGF method failed due to memory limitations above a

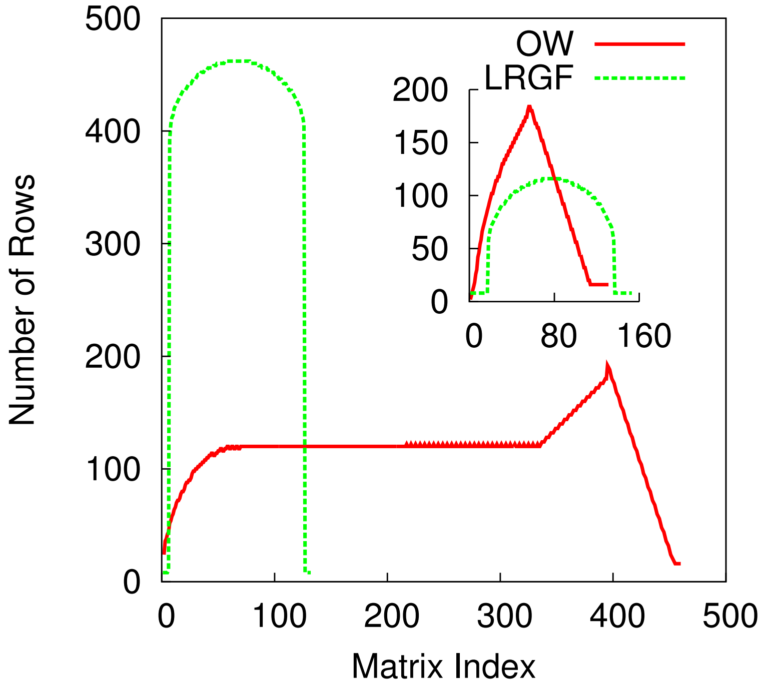

Figure 2.3.3: The size of each sub-matrix, in order of sub-matrix index, for Outward Wave (red pluses) and LRGF (green crosses) for stadiums of system size parameters 40 and 10 (insert).

system size parameter of 38, which surprised us since the data themselves wouldn't have breached the memory limit. However, since the recursive algorithms require allocating many blocks of memory of varying sizes, it is very likely that the pointer tables and the allocation process induce memory overheads.

We also modeled the estimated time of calculation for standard linear recursive and outward wave methods using the optimization function $O\left(\{N_i\}\right) = \sum_i N_i^3$ and found the same cross-over point at system size parameter 19 (Figure 2.3.2). For our ensembles, we found it difficult to determine whether the time of inversion or the challenges with allocating and storing memory were the dominant factors in the final calculation times. We did not plot the equivalent results using full inversion since the underlying algorithm is different.

To understand how each method contributed to the optimization function, we also plot the size of each matrix that must be inverted for the LRGF and Outward Wave methods for stadia of system size parameter 10 and 40 in Figure 2.3.3 as in Wimmer and Richter [38]. The area underneath each function is the same and adds to the total number of orbitals in each system. As a result, each curve represents, in effect, the bandwidth of the sparse Hamiltonian according to the two permutations. The better the permutation, the smaller the overall bandwidth the shorter (and wider) it will appear in this graphic. At the system size parameter 10, which is near the cross-over point at 12, we find very similar matrix bandwidths for the two methods, which corroborates both our predicted and measured calculation times. Beyond the cross-over point, the Outward Wave method requires the inversion of many more matrices but of far smaller size, giving an overall performance boost.

2.3.3 Reflection Matrix For Single-Lead Relativistic Stadium

We choose to examine the single transmission fluctuation at $E = 1.9584\text{eV}$ in Figure 2.3.1. The physical explanation for such transmission fluctuations is well accounted for by Fano resonance theory[43] which provides a succinct formula that models the conductance fluctuation as

$$G(\epsilon) \propto \frac{(\epsilon + q)^2}{\epsilon^2 + 1} \tag{2.3.1}$$

Here ϵ is the energy of the system, zeroed at the center of the resonance, and q is an asymmetry factor. Fano proposed that these conductance fluctuations result from the interference of a directly and an indirectly (resonant) scattering state. This theory suggests that the breadth of the resonance (and the conductance fluctuation) will be

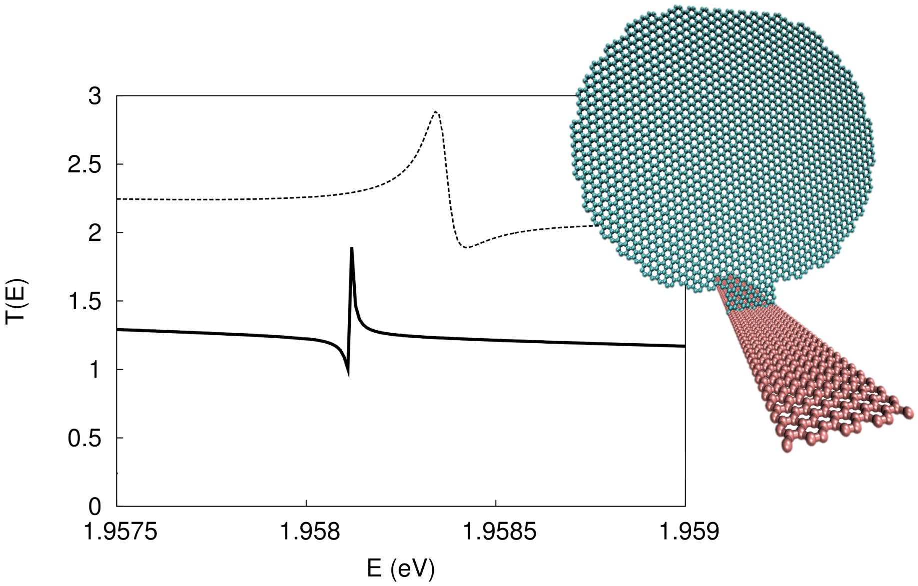

Figure 2.3.4: Transmission function for the relativistic stadium (dashed) and its Helmholtz-resonator equivalent (solid) which is shown in the insert.

proportional to the coupling between the resonant mode and the environment (leads), and that the asymmetrical q-factor can be accounted by the relative phase between the directly scattering state and the indirectly scattering state.

We can test these implications by comparing the two-lead stadium to an equivalent simulation where the incoming and outgoing leads are in fact an infinite nanoribbon with a stadium resonator attached perpendicular to the direction of flow, as depicted in Figure 2.3.4. This scenario can be described as a Helmholtz resonator as discussed in Section 2.2.5.

We expect three changes to happen for the Helmholtz resonator:

1. The energy of the resonance, and thus the center of the conductance fluctuation, will shift to reflect the change in coupling matrix.

2. The resonance width will reduce by a factor of two, to reflect that we have

System Size Parameter	SuperLU	Outward Wave	Ratio
80	57.3	49.5	1.158
100	76.7	56.3	1.362
200	156.3	95.1	1.644
300	247.6	132.0	1.876
400	340.8	174.8	1.950

Table 2.3.1: Comparison of time trials (in average seconds per energy trial) for rectangular graphene stadia. As the system size parameter increased, so did the improvement in efficiency for Outward Wave over SuperLU.

reduced coupling between the resonant state and the environment by half.

3. It has been suggested by Racec et al.[44] that the asymmetry q-factor can be explained by the relative lateral symmetry between the direct and scattering states. In this case, we expect the asymmetric pattern in transmission to reverse, to reflect the fact that we are now reflecting off the same side of the system, as opposed to tunneling through it. From this perspective, our calculation is an excellent validation of Racec's study.

Each point is beautifully verified in Figure 2.3.4. For instance, the peak at $E = 1.9584$eV shifts down by 0.0003eV and its resonance width is divided by a large fraction. In fact, it is much smaller than we predicted and suggests that there may be additional factors constricting the resonant width in the Helmholtz resonator scenario. In addition, we see that its asymmetric profile has reversed, reaching a transmission minimum before its transmission maximum. In both cases, the transmission fluctuation traverses approximately one unit.

2.3.4 Sparse Matrix Packages

We performed a set of experiments using a variation of the relativistic stadium with square ends. We tested our time trials using our Outward Wave method against an equivalent calculations using sparse matrix inversion for the required elements using SuperLU[30]. In each trial, we kept the length of the system identical, but increased its width according to the system size parameter, as with the relativistic stadium trials. We report the results in Table 2.3.1. In all experiments, we obtained identical results for transmission to within precision of the machine. For both algorithms, we found a similar scaling of computation time with the system size parameter. We found that for small systems, both algorithms returned results in approximately the same time scale. As the systems grew larger compared to the distance between the input and output boundaries, however, we found efficiency gain for Outward Wave, approaching a factor of two for our largest system. We attribute the efficiency gain of our code to the fact that the algorithm and software are specifically tailored to our problem. Moreover, the roughly equivalent scaling with system size between the Outward Wave method and SuperLU corroborates that Outward Wave achieves a close-to-optimal block-diagonalization of the Hamiltonian, and comes closest to the ideal case for systems that are large compared to the shortest path between the input and output boundaries. This would be the case, for instance, when the input and output boundaries overlap, as in Section 2.2.5.

Chapter 3

Boundary Reflection Matrix

This chapter provides a formalism for calculating the scattering matrix from arbitrary lattice boundaries using the numerical Green's function and Landauer-Buttiker formalism introduced in Chap. 1. Devised for tight-binding systems, the numerical Green's function is ideally suited to solve complex lattice systems which do not yield to analytical methods. But because conductance calculations only need the mode-by-mode *transmission* matrix for lattice systems, so far it has not been extended to provide that detail for the *reflection* matrix which is necessary to examine scattering off a lattice surface (See Fig. 3.0.1).

This chapter addresses the mathematical difficulties with the numerical Green's function technique when the system maps onto a semi-infinite plane by using skew-periodic tubes as leads. We also discuss the relationship between this approach and the phenomenon of internal Bragg diffraction. We demonstrate the boundary reflection matrix on square lattices and the honeycomb lattice, and we use it to examine the re-constructed zig-zag edge[15] at high energies, where we corroborate and extend

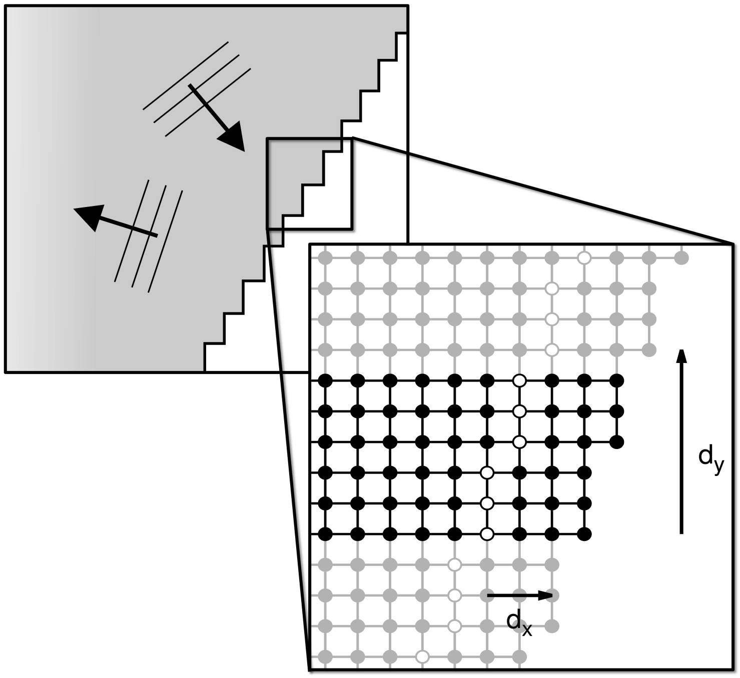

Figure 3.0.1: Schematic diagram of plane-wave reflection off a serrated boundary. Serrations occur on all boundaries of lattice system when they are cut off of an axis of symmetry, which is shown at bottom for an 18° cut on a square lattice. Points in white highlight a single unit cell, and points in grey indicate their skew-periodic continuation, discussed in Section 3.1. The distance traversed from vertically circumnavigating the system is indicated by the arrows, with a horizontal and vertical traverse of d_x and d_y respectively.

related work in the literature[16].

Our goal is to present a formalism that can be extended to any lattice in a general way. Merging the Boundary Reflection Matrix with the Outward Wave Algorithm presented in Chap. 2, we can propose a correct *and* computationally tractable solution to the problem.

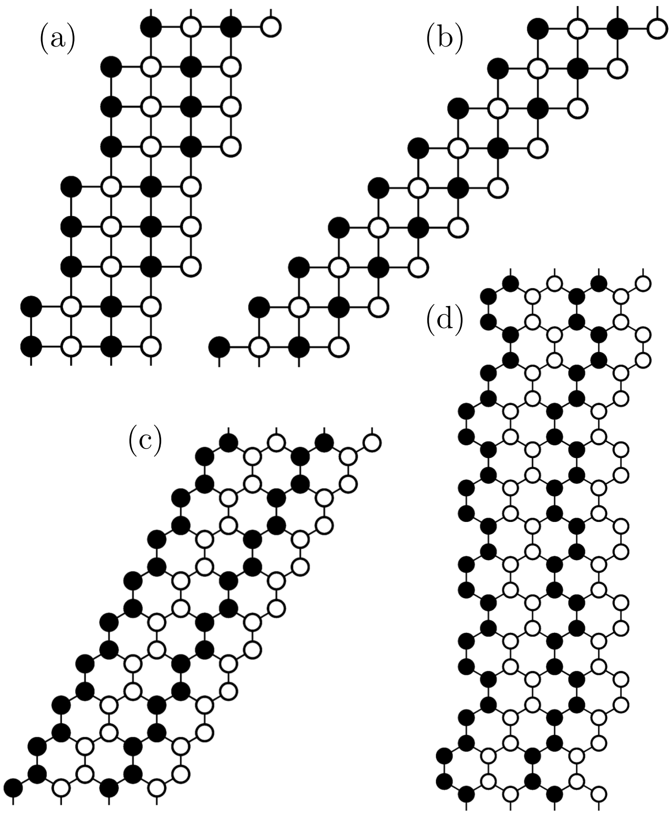

Figure 3.1.1: Schematic of the Hamiltonian for the asymptotic region is shown for the square lattice at 18° (a) and 45° (b), and the honeycomb lattice at 30° (c), and 3° (d). Each unit cell is indicated in alternating bands of white and black.

3.1 The Skew-Periodic Hamiltonian

This chapter examines square and honeycomb lattice Hamiltonians using the nearest-neighbor tight-binding approximation as introduced in Chap. 1. To address the semi-infinite plane, we approximate the Hamiltonian by applying vertical boundary conditions to a horizontal section. To accommodate cuts that do not fall on an axis of symmetry, these boundary conditions are skewed. Fig. 3.1.1 visualizes the skew-periodic boundary conditions by showing the unit cells for cuts along angles of 18° and 45° for the square lattice, and 30° and 3° for the honeycomb lattice.

To model this system using the numerical Greens' formalism outlined in Chapter 1 and Chapter 2, we consider the common left-to-right geometry represented by the Hamiltonian

$$H \to \begin{pmatrix} H_L & V_{LC} & 0 \\ V_{CL} & H_C & V_{CR} \\ 0 & V_{RC} & H_R \end{pmatrix}, \tag{3.1.1}$$

where a finite scattering region is described by the central region H_C which touches two infinite leads H_L and H_R at its left and right boundaries. In the case of a semi-infinite system, there is only one lead, which corresponds to the asymptotic region. Accordingly, we adjust our schematic to

$$H \to \begin{pmatrix} H_A & V_{AC} \\ V_{AC}^{\dagger} & H_C \end{pmatrix}. \tag{3.1.2}$$

The boundary between the scattering region and the asymptotic region can be seen as the line of white circles in Fig. 3.0.1.

3.2 Asymptotic Modes

For the continuum, the modes of the asymptotic region χ_m can be computed analytically or numerically by sampling the Schrodinger equation on a lattice with spacing a and diagonalizing the unit cell Hamiltonian. For the skew-periodic system and other lattices, however, this is not possible. For example, the unit cell Hamiltonian of the square lattice at a 45° cut has no off-diagonal entries in the Hamiltonian, so its eigenvectors are merely point functions.

There are two other ways to produce the modes in such systems. The first method

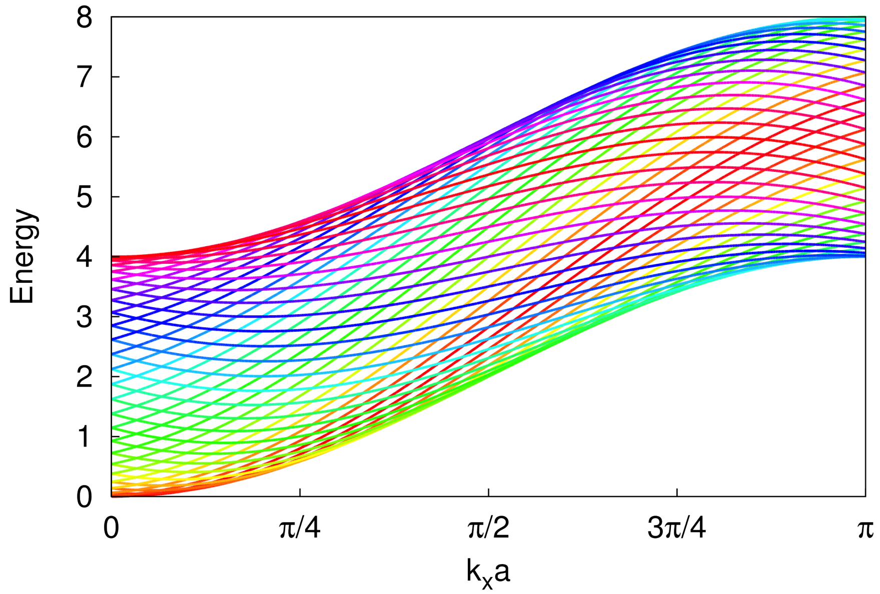

Figure 3.2.1: Band structure for a 30° cut with 50 unit cells.

applies horizontal Bloch conditions to the unit-cell Hamiltonian, which is then diagonalized to compute the band structure, as shown in Fig. 3.2.1 for the 30°cut. The drawback is that each calculation is dependent upon the wave-vector chosen for the Bloch condition, so that the Hamiltonian must be diagonalized for a spectrum of k-vectors. To arrive at solutions for a given energy, this method requires a function minimum search for each mode, which is computationally expensive and potentially imprecise.

Instead, we start from the asymptotic Green's function g which is computed in an automated fashion using the Lopez-Sancho method[18, 19], which provides state-of-the-art efficiency. This allows us to compute the matrix

$$A = gV_{LL} = V_A D_A V_A^{\dagger}, \tag{3.2.1}$$

where V_{LL} is the hopping term between subsequent unit cells in the asymptotic region.

The columns of V_A yield the asymptotic modes χ_m and are associated with eigenvalues equal to $e^{ik_{mx}(E)a}$ where $k_{mx}(E)$ is the horizontal Bloch wavevector.

When computing the asymptotic modes from Eq. 3.2.1, we can map them onto a plane-wave basis using the eigenvectors $e^{ik_{mx}(E)a}$, which provide the horizontal component of the wavevector $\mathbf{k}_m$ and must be satisfied exactly. Determining the vertical component is aided by the boundary conditions of the Hamiltonian.

We begin by considering the zero-degree cut, or tube. The vertical component of any mode in this system must satisfy $k_{my} = \frac{2\pi}{L}N$ where N is a positive or negative integer, since the wavefunction returns to its original value when it circumnavigates the tube.

When skew is applied to the periodicity, the plane wave effectively traverses a horizontal distance when it circumnavigates the system (see Figs. 3.0.1 and 3.1.1), and returns to its initial position with an additional phase of $k_{mx}d_x$, where d_x is the horizontal distance that the unit cell traverses. The equation

$$e^{ik_{my}d_y} = e^{ik_{my}d_y + ik_{mx}d_x} \tag{3.2.2}$$

must be satisfied, yielding

$$k_{my}(N) = 2\pi N/d_y - k_{mx}d_x/d_y \tag{3.2.3}$$

for negative and positive integers N.

To determine the vertical component of $\mathbf{k}_m$, the function

$$F_{mN} = \int \chi_m(x,y)e^{i(k_{mx}x + k_{my}(N)y)}dxdy \tag{3.2.4}$$

is computed for each value of N such that $-2\pi a^{-1} < k_{my}(N) \leq 2\pi a^{-1}$. For each mode, only one value of N returns a non-trivial value. The wavevector that corresponds to this value satisfies both the dispersion relation at the given energy *and* the vertical boundary conditions. Thus, for each asymptotic mode obtained from the quantity A, we can identify a unique plane wave with a wavevector pointing towards the cut.

3.3 Retrieving the Scattering Matrix

The scattering matrix, can be computed according to Eq. 1.3.28 as

$$s = i\Gamma^{1/2} G \Gamma^{1/2} - \mathbf{I}, \tag{3.3.1}$$

where $\mathbf{I}$ is the identity matrix of the size of the central region. A key observation here is that just like the $-\delta_{nm}$ term in Eq. 1.3.27, the identity matrix in Eq. 3.3.1 affects only the reflection matrix, and relies on the assumption that Γ can be diagonalized into orthogonal vectors.

For lattice systems and even the continuum with skew-periodic boundary conditions, there is no reason to expect this assumption to be held, since Γ is produced in a black-box fashion from the semi-infinite Green's function. For any cut, there will be degenerate modes with identical magnitudes of k_x corresponding to incoming and outgoing modes, which result in a non-symmetric coupling matrix Γ.

As a result, diagonalizing the matrix $\Gamma = VDV^\dagger$ fails to produce an orthogonal set. However, we can symmetrize the coupling matrix by the transformation

$$\Gamma \to \left(\Gamma + \Gamma^T\right)/2, \tag{3.3.2}$$

giving Γ an orthogonal decomposition, and making it possible to compute the scattering matrix according to Eq. 1.3.28. Unfortunately, the transformation mixes information between incoming/outgoing mode pairs, however, this information is already mixed in the original coupling matrix. For our calculations, it suffices to assume that any given mode determined by Γ is an incoming mode, since the system is expected to behave identically under time-reversal symmetry (this is obviously broken in the presence of the magnetic field).

Once the scattering matrix is calculated in Eq. 3.3.1 using the coupling matrix from Eq. 3.3.2, it can be transformed into any other complete basis set. For cuts along an axis of symmetry of the underlying lattice, the asymptotic modes χ_m derived from Eq. 3.2.1 constitute a complete set, but for others the matrix A is not symmetric, or the boundary region is often smaller than the size of a unit cell of the asymptotic region, collapsing asymptotic modes onto an incomplete basis set.

However, in all cases the modes of Γ under the transformation of Eq. 3.3.2 *do* constitute a complete set. As a result, it is possible in these situations to calculate the overlap between modes of Γ and the asymptotic modes to compute a quantity similar to the scattering matrix, but which only indicates whether reflection between two modes is *possible.* It turns out the that these permitted reflections follow physical laws which we explore in Sec. 3.5.

3.4 Results for the Square Lattice

For edge cuts along a symmetry axis of the lattice, the set of modes χ_m constitute a complete set and the scattering matrix can be unambiguously projected onto them. Because of the finite size of the system, however, only a finite number of points in the scattering matrix for the semi-infinite system are produced.

We introduce the reader to this principle using a square lattice at a 45° cut at low

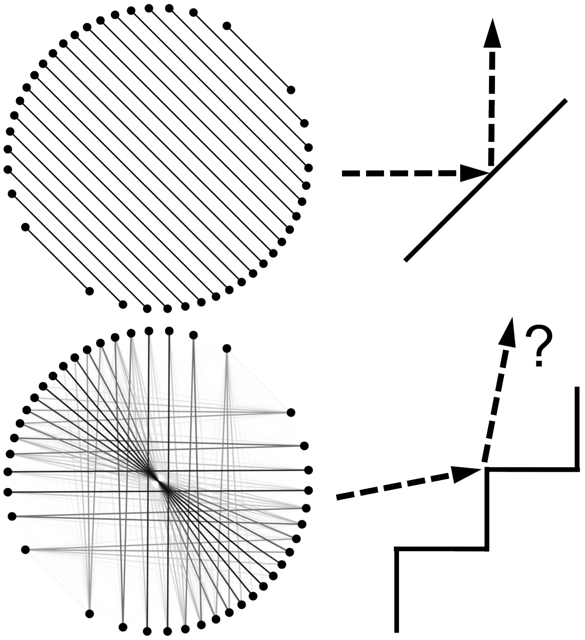

Figure 3.4.1: Part (a): The reflection matrix for the 45° cut in k-space as lines connecting discrete asymptotic modes. Part (b): A similar cut, but now with steps, produces and entirely different reflection matrix which is decomposed into three types of classical reflections in Fig. 3.4.3.

energy. In Fig. 3.4.1a we show the scattering matrix for this cut as lines connecting the incoming and outgoing wavevectors in k-space. Each line follows the 45° diagonal and corroborates predictions from specular reflection, in which the angles of incidence across a cut are equal for both the incoming and outgoing plane waves. As seen in the figure, only a finite set of points in k-space are sampled.

In Fig. 3.4.2 we show the incoming angles of these points as a function of energy. The figure shows that as energy increases, more modes become available. According to the law $E \propto k^2 = k_\parallel^2 + k_\perp^2$, as soon as a mode becomes available, it proportions all of its energy into the transverse component of the wavevector and points parallel to the cut. As energy increases further, the mode proportions more of its energy into the

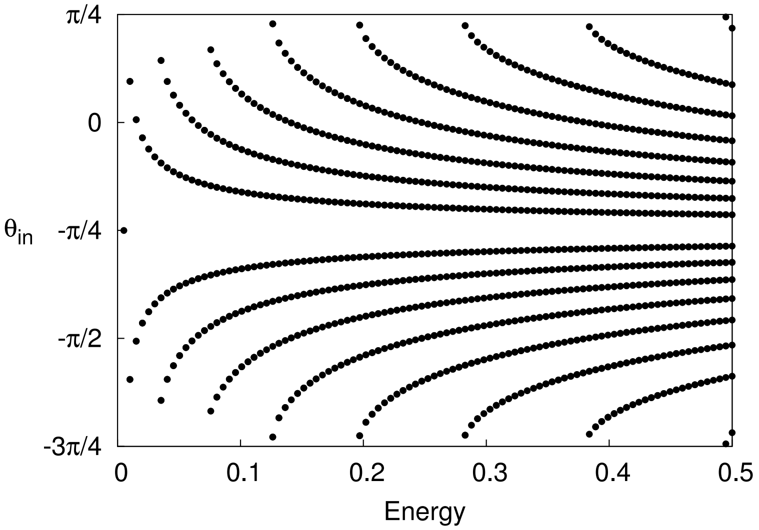

Figure 3.4.2: For the 45° cut with fifty vertical unit cells, the incoming angle is plotted against system energy. As modes become available at higher energies, their measured incoming angle asymptotically approaches $\pi/4$. This is understood since the wavevector component parallel to the cut remains the same at all energies for a given mode, but the component perpendicular to the cut grows with energy.

longitudinal component of the wavevector, and asymptotically points perpendicular to the cut.

More complicated geometries that follow the 45° diagonal can also be modeled . In Figs. 3.4.1b we show k-space representation of the reflection matrix for the 45° staircase, and find that we produce many more reflections.

Even though this is a black-box quantum computation, our results corroborate physical intuition. In the staircase, there are three types of reflections which we decompose in Fig. 3.4.3, and all can be described classically as reflection off the vertical wall (top), horizontal wall (middle), or both (bottom). Because this is a quantum system, however, one expects that as the incoming plane-wave angles move parallel to the cut, diffraction effects should arise and grow stronger. In Fig. 3.4.3, each mode close to the horizontal and vertical reflects onto another unambiguously, but modes

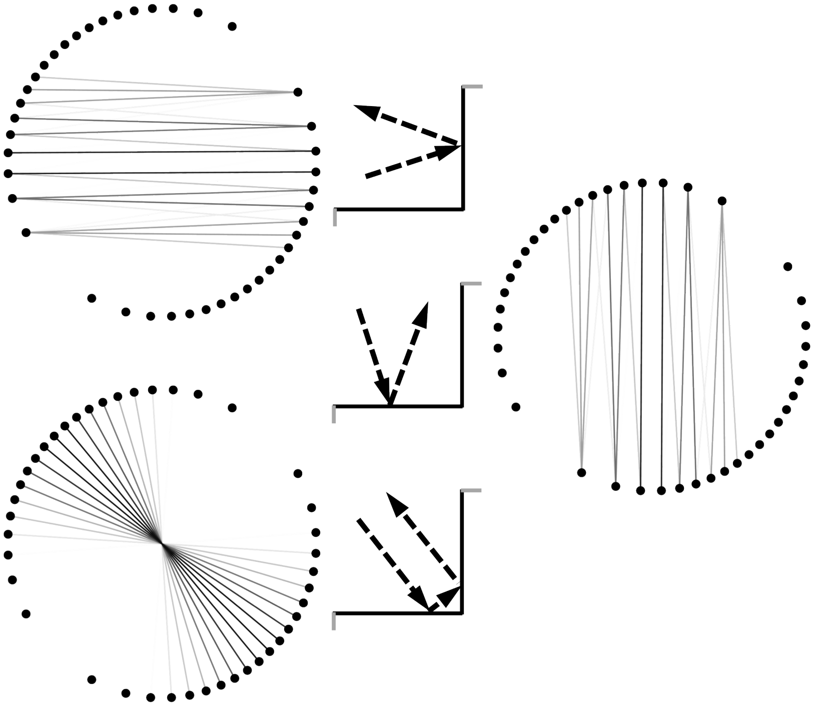

Figure 3.4.3: The reflection matrix from Fig. 3.4.1 is decomposed into four major reflection types. From top to bottom: Reflection off the vertical wall, reflection off the horizontal wall, reflection off of both walls, and diffraction from the edges, which only affects incoming angles that skim along the 45° cut.

closer the 45° angles reflect onto many modes, corroborating this expectation.

3.5 Internal Bragg Diffraction

Once we cut against an axis of symmetry, the modes of the asymptotic region are no longer orthogonal along the unit cell. At higher energies, the non-orthogonality of the asymptotic modes are closely related to internal Bragg diffraction.

It is possible to quantify internal Bragg diffraction by considering the schematic in Fig. 3.5.1. Here the boundary is cut at an angle angle $\phi \approx 18°$, where $\phi = 0$ is a vertical edge, and an incoming plane wave strikes the surface at angle θ_{in}, where

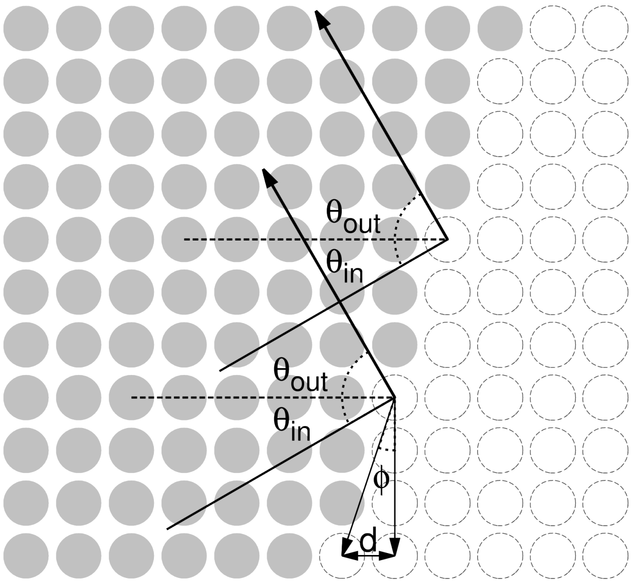

Figure 3.5.1: This diagram shows the considerations for Bragg diffraction from a boundary. In light gray are the lattice sites for the system, and in dark grey are shown phantom lattice points outside the system where the wavefunction must go to zero. A ray coming in at an angle θ_{in} and reflects at θ_{out} will interfere with rays from adjacent equivalent points on the boundary unit cell. The angle ϕ (18°) and horizontal distance between adjacent unit cells d are identical to many of the calculations presented throughout this chapter.

$\theta_{\text{in}} = 0$ points to the right, and positive angles point upward. This plane wave reflects to an outgoing angle θ_{out} where $\theta_{\text{out}} = 0$ points to the left and positive angles point upward.

If there is a repeating unit cell in the edge, two rays which hit equivalent points of adjacent boundary unit cells gain or lose relative phase based on their wavevectors and the distances they travel. For instance, a ray incurs an additional phase of $\delta = kd\frac{\sin(\theta-\phi)}{\sin\phi}$ when $\theta_{\text{in}} > -\phi$ and $\delta = kd\frac{\sin(\theta+\phi)}{\sin\phi}$ when $\theta_{in} \geq \phi$. Here d is the horizontal distance between identical points in adjacent unit cells and k is the wavevector magnitude of the incoming wave. When the plane wave is reflected, its neighbor gains phase according to the above formulas, but with k indicating the outgoing wavevector magnitude. When these two phases add to $n2\pi$ where n is an integer, the two rays constructively interfere.

Because the wavelength shrinks with increasing energy, more Bragg branches appear as energy goes up. And because the distance between adjacent unit cells increases for slighter angles against an axis of symmetry, more Bragg branches appear for shallower cuts.

To model internal Bragg diffraction, we have repeated the 18° unit cell from Fig. 3.1.1 and simply terminated it to produce a system similar to Fig. 3.5.1. In this case, and for all systems constructed in a similar fashion, the resulting scattering matrix in terms of modes of the transformed coupling matrix Γ is always identity. The off-diagonal results in terms of the asymptotic modes then arise entirely by the overlap of modes which satisfy Bragg conditions.

As a result, calculations using this method cannot unambiguously resolve between asymptotic modes and provide an accurate scattering probability. However, the scattering matrix that results *does* show among which asymptotic modes scattering is *possible*. In the left-hand column of Fig. 3.5.2, we show these relationships for the 18° as lines connect the incoming and outgoing wavevectors (bottom) and as a scatter plot in terms of incoming and outgoing angles (top), using the conventions in Fig. 3.5.1.

As can be seen, the equality of incoming and outgoing angles of incidence (dotted line) is no longer satisfied due the presence of additional Bragg branches above and below this relation. Specular reflection can be conceived as a special case of Bragg diffraction where $n = 0$, but because the dispersion relation alters the magnitudes of the incoming and outgoing based on their orientation (see Fig. 3.5.3), it is not true

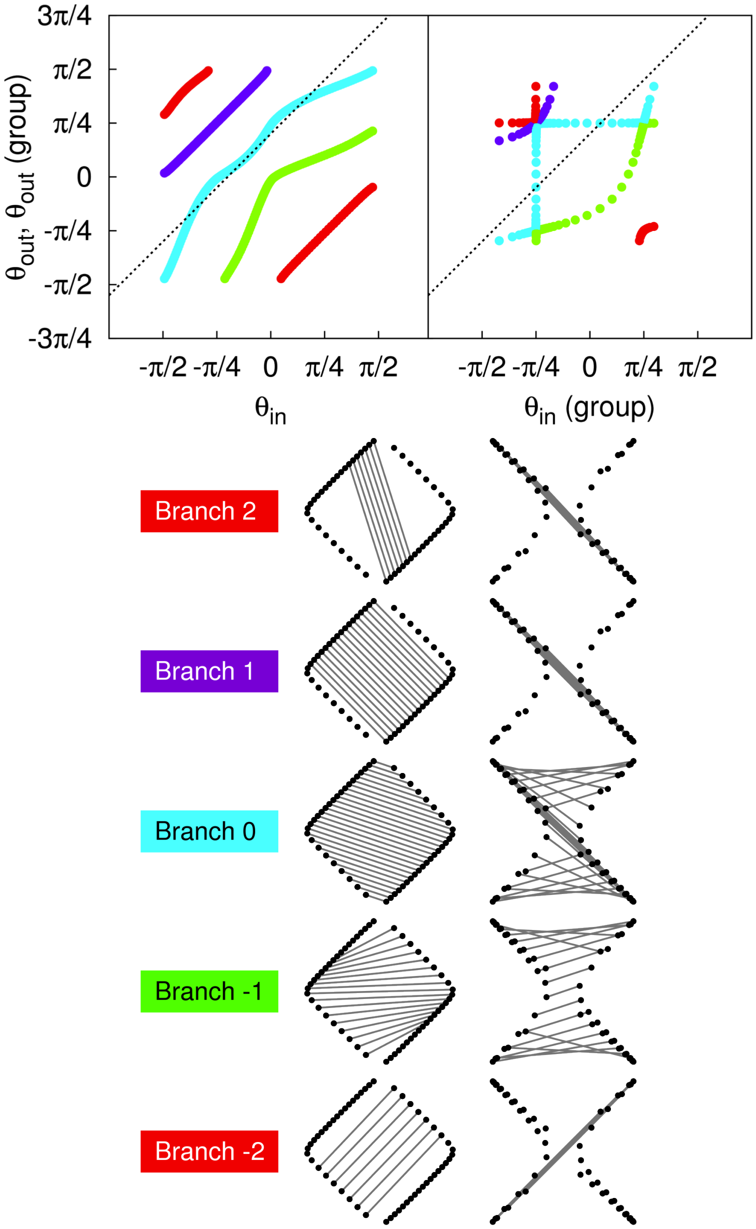

Figure 3.5.2: Top: The scattering modes for a system with an 18° cut, with 50 vertical unit cells and at energy $E = 3.95t$. On the left, results are shown in terms of phase velocity, and on the right results are shown in terms of group velocities. Specularity conditions are shown in the dotted lines. Each branch is indicated by color. Bottom: For each branch in the scattering matrix, the incoming and outgoing modes are shown as points in k-space (left) and group-velocity space (right). Each point in the top figure corresponds to a line connecting two modes. For this representation, we use a system with only 10 vertical unit cells to visually resolve individual reflections.

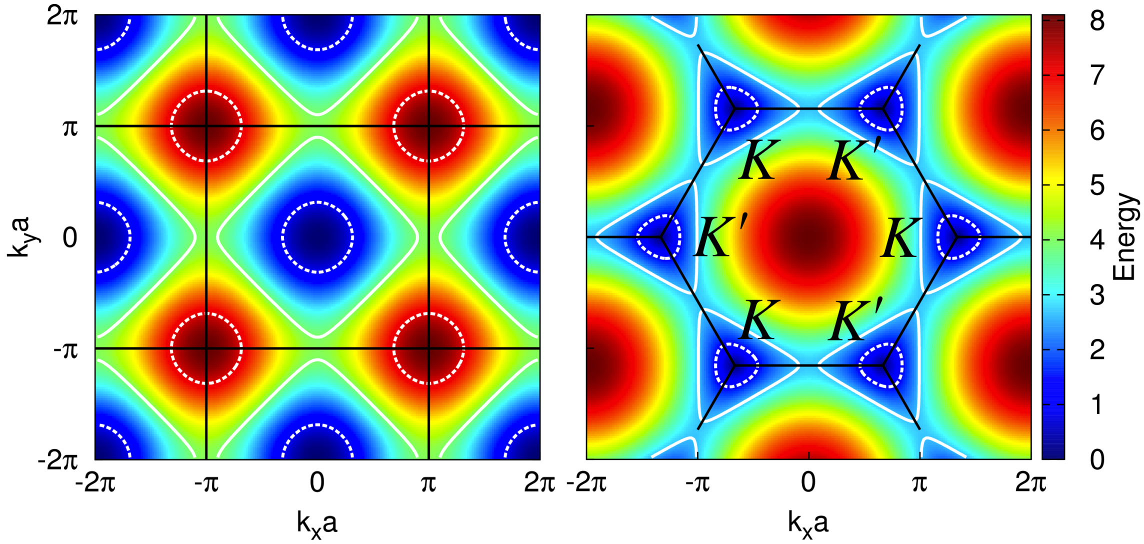

Figure 3.5.3: The two-dimensional dispersion relation for the square (left) and honeycomb lattices (right) demonstrate strong group-velocity warping at high energies. In dashed, the dispersion relations for $E = 0.9t$, $7.1t$ (left) and $0.5t$ (right) are nearly circular, while their neighbors near the band edge $E = 3.9t$ (left) and $0.98t$ (right) show strong warping.

that this branch always correlates to equal angles of incidence. This can be seen in the warping at higher energies of the central, specular branch (Branch 0) in Fig. 3.5.2 from the dotted line.

If one is interested not in the scattering of plane waves but semiclassical particles, it is necessary to examine the group-velocity vectors $\nabla_{\mathbf{k}} E\left(\mathbf{k}\right)$ associated with the wavevector of each asymptotic mode, since these are stronger indications of classical dynamics. Warping in group-velocity (See Sec. 3.6) can further distort the angles of incidence for possible scattering pairs, as shown in the right-hand column of Fig. 3.5.2.

We corroborate our results using a Gaussian beams at lower energies on the 18° cut, which is produced using a coherent wavepacket $|\mathbf{r}_0, \mathbf{k}_0, \sigma\rangle$ where $\mathbf{k}_0$ satisfies the

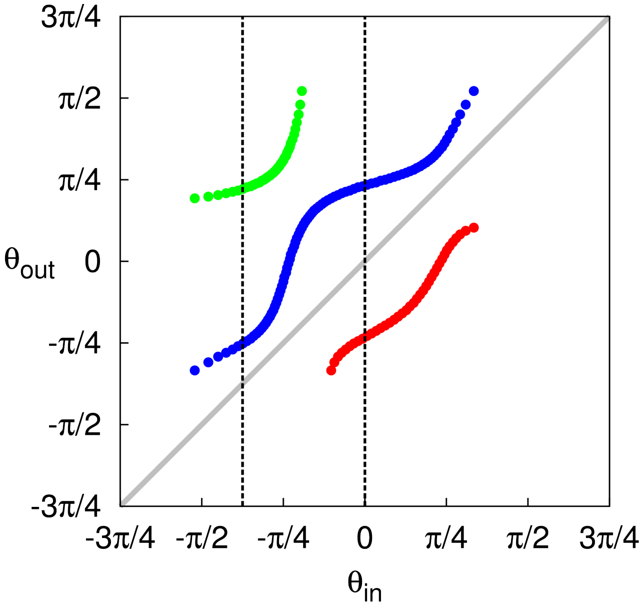

Figure 3.5.4: The internal Bragg relationship for a square lattice with an 18° cut as depicted in Figs. 3.5.5 and 3.5.1, computed using a scattering matrix on a square-lattice with 50 vertical unit cells at energy $E = 2.5t$. The identity line is shown in grey. The two incoming group-velocity angles from Fig. 3.5.5 of 0° and $-40°$ are shown in vertical black dashed lines. The specular line is shown in blue, and the upper and lower branches are shown in green and red respectively.

dispersion relation at energy E_0, and a set of eigenstates $\{\psi_E\}$ for a system, each of which is associated with an eigenenergy E. The wavefunction that results is written as

$$\Psi = \sum_E \langle \psi_E | \mathbf{r}_0, \mathbf{k}_0, \sigma \rangle \, \psi_E. \tag{3.5.1}$$

Because of the uncertainty of the wavepacket, only wavefunctions at energies close to E_0 contribute to the sum. Thus, only a finite range centered around E_0 must be considered.

It is important to choose the spread of the coherent state wisely. Too large a coherent state restricts the set of eigenstates that contribute to the sum, giving unclear results. Too small a coherent state does not provide enough information to resolve

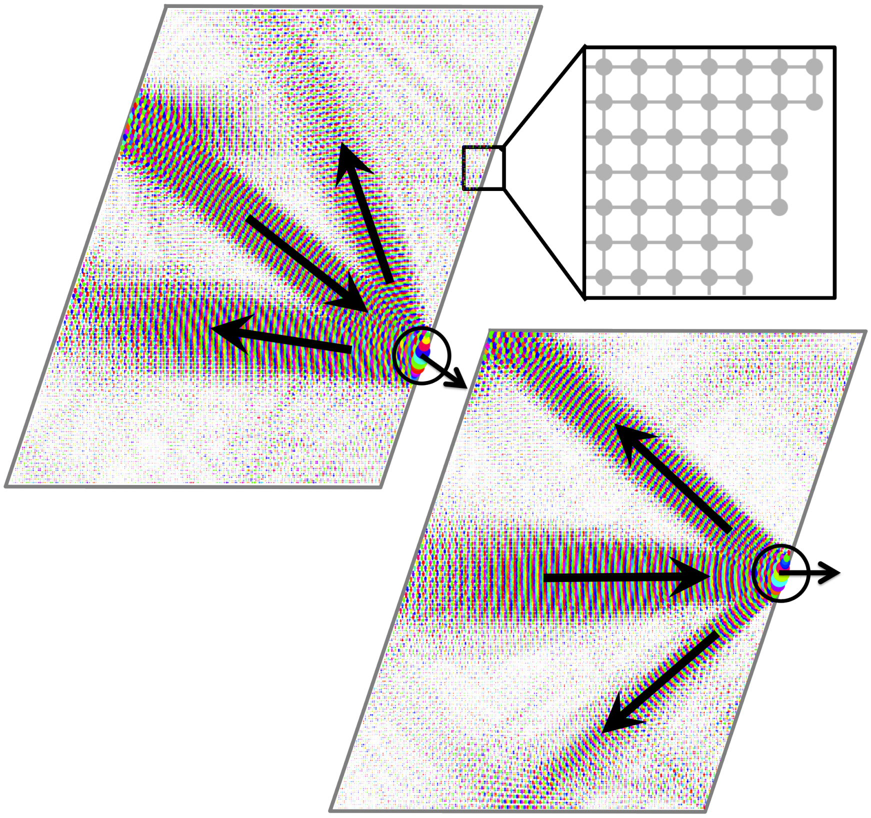

Figure 3.5.5: Two Gaussian Beams are shown, constructed by summing the set of closed-system eigenstates in the energy range $2.48 < E < 2.52$ weighted by Eq. 3.5.1, using a coherent state with momentum uncertainty $\Delta k/k = 5\%$ that sits on the right-hand boundary (black circles) with specified momentum (small black arrows). The system is a square lattice cut at an 18° angle (inset). The incoming group-velocity angle is set to 0° at top and $-40°$ at bottom.

features of the beam. In Fig. 3.5.5 a compromise is chosen at $\Delta k/k = 5\%$, which provides a sufficient range of eigenstates to make a clear beam.

The classical paths suggested by the Gaussian beams in Fig. 3.5.5 must all travel through the position $\mathbf{r}_0$ with momentum $\hbar\mathbf{k}_0$ (Eq. 3.5.1) defined by the coherent state for each beam. In both top and bottom figures, the coherent state lies along the right-hand boundary, although the wavevectors for each coherent state differs. Because the breadth of a coherent state grows in time when it propagates, each beam focuses at the coherent state, and spread from its center.

In Fig. 3.5.4, we present the reflection matrix for the 18° cut at $E = 2.5t$, which corresponds with the Gaussian beam in Fig. 3.5.5. The two incoming beams from Fig. 3.5.5 are represented by vertical dashed lines in Fig. 3.5.4. Each intersects the graph at the three locations: along the identity line for the incoming beam, along the blue specular line for an outgoing beam, and along one of the Bragg branches for the other outgoing beam. Our predictions are strongly validated by Fig. 3.5.5.

The test wavepacket used to create the Gaussian beam has a spread that is only 6 unit cells across, meaning that only a few surface defects can produce substantial Bragg scattering. The ubiquity of this effect has implications for ray-tracing methods, which bridge classical and quantum explanations for phenomena such as fractal conductance fluctuations[45, 46, 47] and caustics[48, 49] and encourages a re-examination ray-splitting[50] and other hypothetical edge effects[51, 52].

3.6 Results for the Honeycomb Lattice

The classical dynamics of lattice Hamiltonians depend on the band structure of the system. While the number of orbitals in the unit cell determines the number of distinct bands[9], warping in the band structure can produce additional valleys. In the square square lattice, only one band exists because there is one orbital per unit cell, but warping gives rise to an additional set of pseudo-particles called holes which exist above $E = 4t$ (see the contour lines in Fig. 3.5.3 near the corners of the Brillouin zone).

Holes can be treated like particles if the local origin of the valley is subtracted from the wavevector associated with each mode to closely parallel the group-velocity vector. Our calculations (not shown) show that this modification produces identical scattering matrices for both sets of pseudo-particles under the transformation $E_h = 8t - E_p$.

In the honeycomb lattice, two orbitals in the unit cell give rise to two bands that are isolated in energy by the Dirac point at $E = 0t$. Because of warping, two inequivalent valleys, indicated by K and K' in Fig. 3.5.3, co-exist in the energy range $-t < E < t$. These valleys are famous in graphene since they exhibit a linear as opposed to parabolic dispersion relation near the Dirac point[8]. The fact that the two valleys of the honeycomb lattice exist in the same band means it is possible to scatter between them without invoking large potentials[9].

In Fig. 3.6.1, we show the internal Bragg branches for the honeycomb lattice cut at 3° (See Fig. 3.1.1d) as a parallel to internal Bragg diffraction for the square lattice in Fig. 3.5.2. Armchair edges at 0° cuts only produce reflections between the K' and K valleys, and even though the 3° honeycomb cut produces a near-armchair edge,

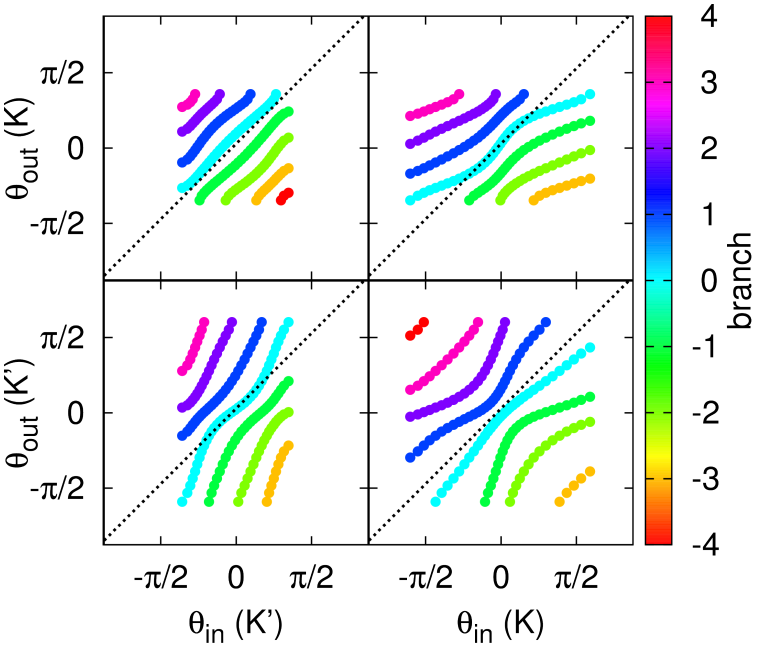

Figure 3.6.1: Internal Bragg relationships for the 3° cut on a honeycomb lattice (See Fig. 3.1.1d) at $E = 0.8t$. Specularity conditions are shown in the dotted line. Even though this is a nearly armchair edge (which normally only exhibits inter-valley scattering), Bragg diffraction can induce other forms of valley scattering.

its jaggedness is actually able to scatter within the same valley as well. For such a shallow cut and at such high energies, many Bragg branches are available to the system.

It's worth noting that the incoming wavevectors in the K' valley and outgoing wavevectors in the K valley are strongly restricted for this system at $E = 0.8t$, as indicated in Fig. 3.6.1. This is a result of group-velocity warping, which permits a smaller range of wavevectors to produce group-velocity vectors pointing towards or away from the cut for these valleys.

For the graphene system, asymptotic modes are orthogonal for the 30° cut, making it possible to examine different reconstructions of the zig-zag edge. In this section, we examine the "re-zag" edge studied by Ostaay et al.[15, 16] (see Fig. 3.6.2). While

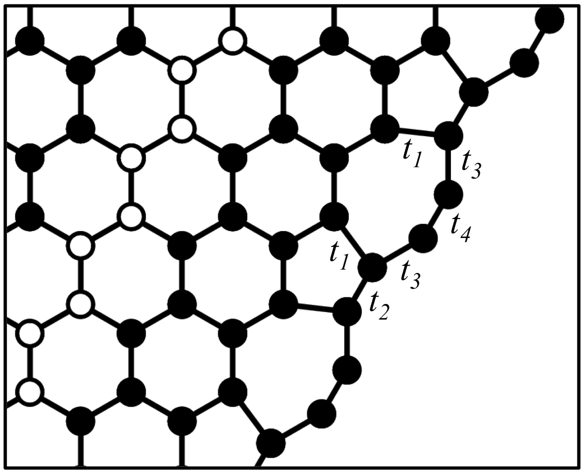

Figure 3.6.2: Hamiltonian for the reconstructed zig-zag edge in graphene. Perturbations to the hopping energies are indicated by $t_{1\ldots4}$. The asymptotic unit cell is identical to that used for any 30° in graphene, as indicated in white.

the hopping parameters at different sites should vary for the re-zag edge, we set all hopping parameters to $t_{1\ldots4} = t$ in order to compare our results against the original authors.

At low energies, we corroborate the findings of Ostaay et al.[15, 16], who found only intra-valley scattering for this system. The most salient consequence of varying the hopping parameters is instead a shift in the energies of localized edge states[12, 53, 16].

Our results at low energy are identical to the zig-zag edge. At higher energies, however, it is possible for the incoming wavelength to be comparable to the distance between adjacent unit cells of the re-zag edge. At these energies, Bragg diffraction allows the re-zag edge to exhibit *inter*-valley scattering. In Fig. 3.6.4, we show the scattering matrix for the re-zag edge at $E = 0.8t$, which exhibits *stronger* inter-valley scattering than intra-valley scattering for certain incoming angles. By comparison, the pure zig-zag reflection matrix at this energy (Fig. 3.6.3) still only shows intra-valley scattering

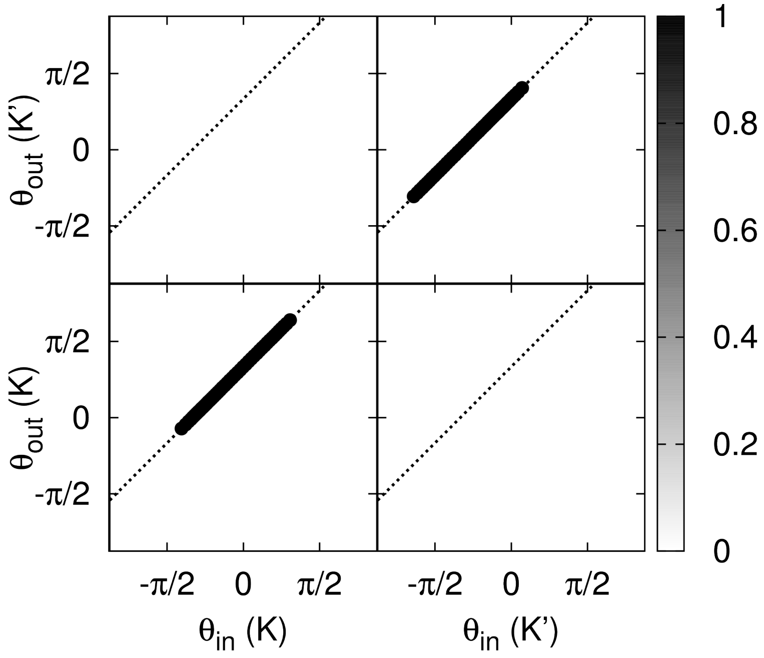

Figure 3.6.3: Scattering matrix for the zig-zag boundary in graphene at $E = 0.8t$ and 150 unit cells. This boundary only reflects within the same valley, so that incoming wavevectors in one valley reflect onto wavevectors of the same valley. Each reflection occurs along the dashed specularity line.

In Fig. 3.6.5 we show two Gaussian beam wavefunctions for a K'-valley coherent state centered on a zig-zag edge (a) and the re-zag edge (b). To determine the valley of each reflected beam, we use the Husimi map technique introduced later in the thesis (See 5, not shown). While the zig-zag edge only scatters back into the K' valley at an angle, the re-zag edge instead reflects most of the beam into the other K valley, and directly to the left (grey arrows). These results perfectly corroborate Fig. 3.6.4, where we have added a vertical dashed line to reflect the initial conditions of the Gaussian beam in Fig. 3.6.5b.

In Fig. 3.6.5 we show two Gaussian beam wavefunctions for a K'-valley coherent state centered on a zig-zag edge (a) and the re-zag edge (b). To determine the valley

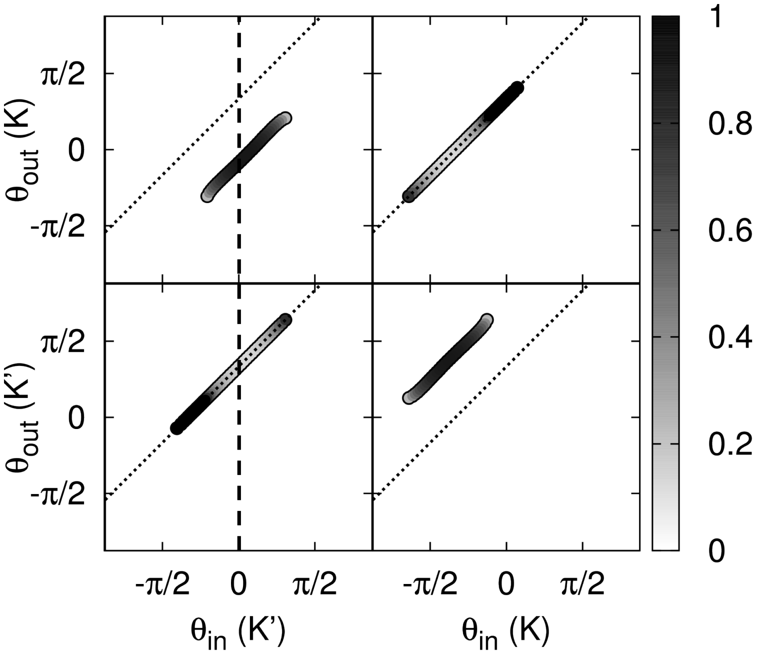

Figure 3.6.4: Scattering matrix for the reconstructed zig-zag boundary at at $E = 0.8t$ and 150 unit cells. Specular reflection conditions are shown in the dotted line. Like the zig-zag edge, each wave reflects onto another of the same valley. However, due to internal Bragg diffraction, at some incoming angles the plane wave reflects far more in the other valley. The vertical dashed line correlates to the initial conditions of the Gaussian beam in Fig 3.6.5b.

of each reflected beam, we use the Husimi map technique introduced later in the thesis (See 5, not shown). While the zig-zag edge only scatters back into the K' valley at an angle, the re-zag edge instead reflects most of the beam into the other K valley, and directly to the left (grey arrows). These results perfectly corroborate Fig. 3.6.4, where we have added a vertical dashed line to reflect the initial conditions of the Gaussian beam in Fig. 3.6.5b.

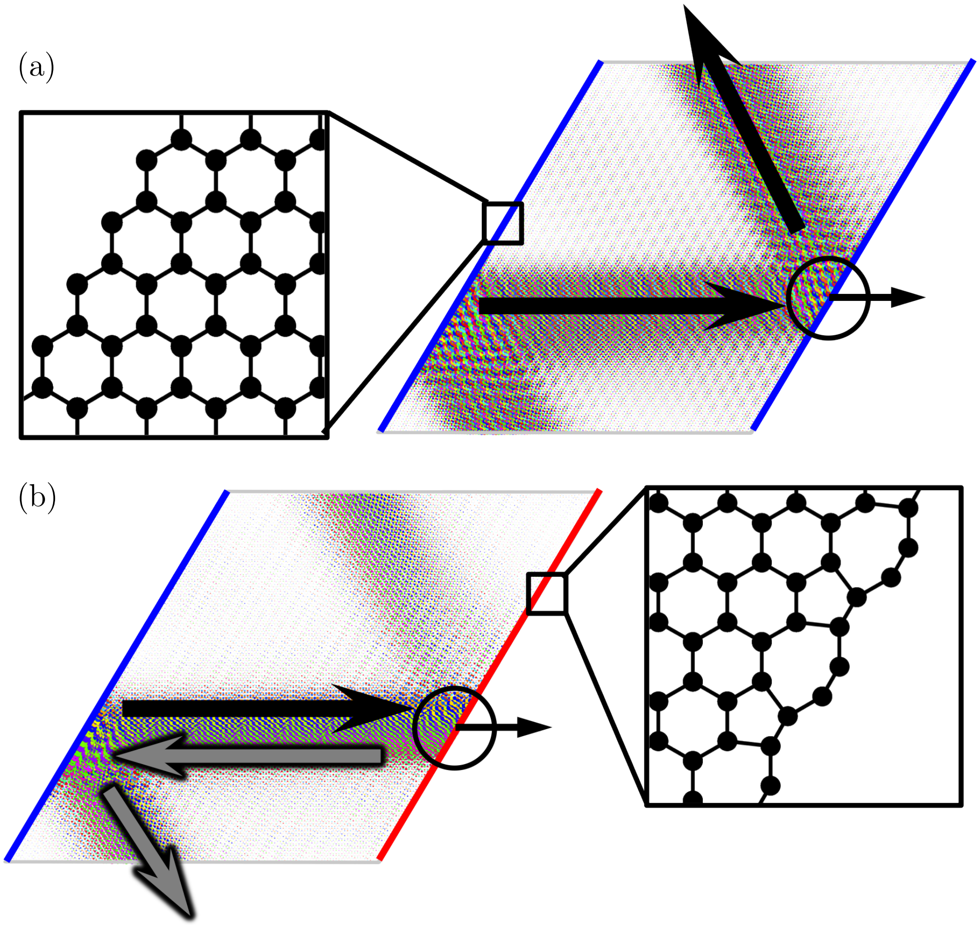

Figure 3.6.5: Gaussian beams are shown for two skew-periodic graphene systems, with zig-zag boundaries in blue and the reconstructed zig-zag boundary in red (see insets). The same coherent state from the K' valley is used to generate both beams (black circle) and points to the right. Since the zig-zag boundary is a pure intra-valley scatterer, the incoming K' valley reflects specularly into the same valley (top), but due to internal Bragg scattering, the re-zag boundary reflects instead into the K valley (grey arrows, bottom).

Chapter 4

The Husimi Map

The probability flux, or probability current, is introduced in quantum mechanics textbooks as a deterministic operator that can be calculated, but its connection to experiment is often left to the reader's imagination. The flux operator, whose expectation over the wavefunction gives the traditional flux $\mathbf{j}\left(\mathbf{r},\mathbf{p}\right)$, is defined as

$$\hat{j}_{\mathbf{r}} = \frac{1}{2m}\left(\left|\mathbf{r}\right\rangle\left\langle\mathbf{r}\right|\hat{p} + \hat{p}\left|\mathbf{r}\right\rangle\left\langle\mathbf{r}\right|\right), \tag{4.0.1}$$

where m is the mass of a particle in the system, and $\mathbf{r}$ and $\mathbf{p}$ the position and momentum. The concept of "flux at a point" seems paradoxical because we say something about momentum while also knowing position precisely. This raises the question: Can the flux even be measured?

On the other hand, probability flux vanishes on stationary states for systems with time-reversal symmetry. This is a shame, since strong semiclassical connections between trajectory flow and quantum eigenstates lie completely hidden in the universal value of 0 for the flux. Consider the example in Fig. 4.0.1, where the strong influence of classical orbits is seen in the scarred eigenstate. For this bound system, the flux is

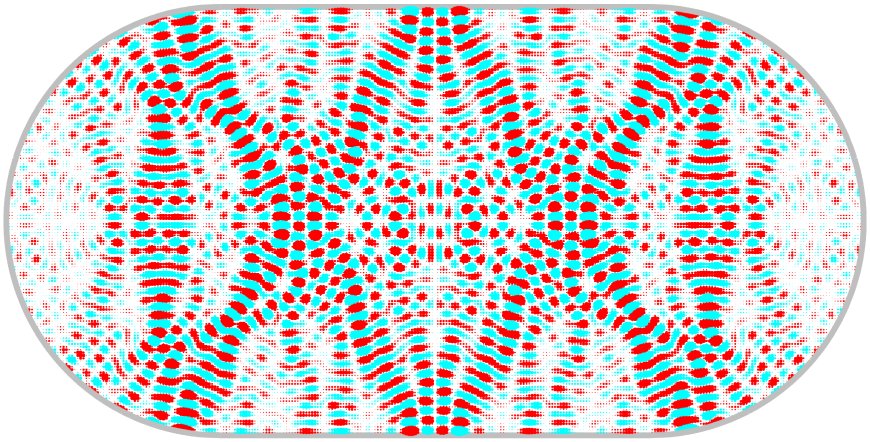

Figure 4.0.1: A scarred eigenstate of the stadium billiard problem is a particle in a box with the shape shown, revealing the strong influence of classical orbits. The traditional flux provides no help: it is uniformly 0 inside the billiard.

always zero, but when it is coupled to a continuum, flux becomes useful as a tool for examining its dynamics, even though information about the dynamics clearly exists before the coupling. Is it possible to bridge this gap?

By using coherent state projections, we can reveal the meaning of the flux operator *and* see how to extend it to become much more useful. The experimental equivalent of a flux map has not been discussed because it is effectively impossible to measure – determining the flux, even at a single point, requires an infinite number of measurements. Instead, we offer an experimentally feasible extension of the flux operator based on the Husimi projection[54], which we show is equivalent to the traditional flux (Eq. 4.0.1) in the limit of infinitesimal coherent states. Because the Husimi projection is able to work away from this limit and on a wider variety of systems, it is able to bridge the gap between stationary and scattering states.

When many Husimi projections are sampled across a system, they produce a Husimi *map* which is a powerful tool for interpreting the semiclassical behavior of wavefunctions. In addition to showing the locations and directions of classical trajectories suggested by a wavefunction, Husimi maps can also quantify how boundaries and external fields affect those trajectories. In this chapter, we resolve issues with the flux operator using the Husimi projection, and demonstrate Husimi maps on a variety of systems with and without external fields. We then show how to use Husimi maps to interpret flux through various open devices.

4.1 Measurement and the Flux Operator

4.1.1 The Gaussian Basis

Several discussions connecting the flux to experimental measurement exist in the literature[55, 56, 57]; here we offer an alternative view. We begin by identifying the eigenstates of the flux operator and giving them a physical interpretation.

When discussing uncertainty, the Dirac basis implicit in Eq. 4.0.1 introduces singularities which we can avoid by replacing the delta functions with the Gaussian basis defined as

$$\langle \mathbf{r} | \, \mathbf{r}_0, \sigma \rangle = \left(\frac{1}{\sigma\sqrt{2\pi}} \right)^{d/2} e^{-(\mathbf{r}-\mathbf{r}_0)^2/4\sigma^2}, \tag{4.1.1}$$

where d is the number of dimensions in the system. The Gaussian function becomes a delta function as $\sigma \to 0$. In the Gaussian basis, the flux operator is

$$\hat{\mathbf{j}}_{\mathbf{r}_0,\sigma} = \frac{1}{2m} \left(|\mathbf{r}_0, \sigma\rangle \langle \mathbf{r}_0, \sigma| \, \hat{\mathbf{p}} + \hat{\mathbf{p}} \, |\mathbf{r}_0, \sigma\rangle \langle \mathbf{r}_0, \sigma| \right). \tag{4.1.2}$$

The eigenstates, projected onto each orthogonal spatial dimension i, are obtained using the eigenvalue equation

$$\hat{j}_{\mathbf{r}_0,\sigma,i}\left|\lambda_{\sigma,i}\right\rangle = \lambda_{\sigma,i}\left|\lambda_{\sigma,i}\right\rangle, \tag{4.1.3}$$

which has a solution of the form

$$\left|\lambda_{\sigma,i}\right\rangle = \left|\mathbf{r}_0,\sigma\right\rangle + a\hat{p}_i\left|\mathbf{r}_0,\sigma\right\rangle. \tag{4.1.4}$$

Using the two equations

$$\left\langle \mathbf{r}\left|\hat{\mathbf{p}}\right|\mathbf{r}_0,\sigma\right\rangle = i\hbar\sigma^{-2}\left(\mathbf{r}-\mathbf{r}_0\right)e^{-(\mathbf{r}-\mathbf{r}_0)^2/4\sigma^2} \tag{4.1.5}$$

and

$$\left\langle \mathbf{r}_0,\sigma\left|\hat{\mathbf{p}}\right|\mathbf{r}_{0,}\sigma\right\rangle = 0, \tag{4.1.6}$$

we can write

$$\hat{j}_{\mathbf{r}_0,\sigma,i}\left|\lambda_{\sigma,i}\right\rangle = \frac{1}{2m}\left(a\left\langle\hat{p}_i^2\right\rangle_\sigma\left|\mathbf{r}_0,\sigma\right\rangle + \hat{p}_i\left|\mathbf{r}_0,\sigma\right\rangle\right). \tag{4.1.7}$$

Further, it is useful to find the conditions on $\lambda_{\sigma,i}$ that allow Eq. 4.1.7 to be written in the form of Eq. 4.1.3,

$$\lambda_{\sigma,i} = \frac{a}{2m}\left\langle\hat{p}_i^2\right\rangle_\sigma;\lambda_{\sigma,i} = \frac{1}{2ma}. \tag{4.1.8}$$

Since $\left\langle\hat{p}_i^2\right\rangle_\sigma = \frac{\hbar^2}{4\sigma^2}$, we can determine the value of $a = \pm\frac{2\sigma}{\hbar}$ and from that we obtain the two eigenvalues

$$\lambda_{\sigma,i,\pm} = \pm\frac{\hbar}{4m\sigma}. \tag{4.1.9}$$

The eigenstates take the form

$$\left\langle\mathbf{r}\right|\left.\lambda_{\sigma,i,\pm}\right\rangle = \left\langle\mathbf{r}\right|\left.\mathbf{r}_0,\sigma\right\rangle \pm \frac{i}{\sigma}\mathbf{e}_i\cdot\left(\mathbf{r}-\mathbf{r}_0\right)\left\langle\mathbf{r}\right|\left.\mathbf{r}_0,\sigma\right\rangle, \tag{4.1.10}$$

where $\mathbf{e}_i$ is the unit vector along spatial dimension i. Eq. 4.1.10 is a linear combination of two functions: the Gaussian (Eq. 4.1.1) and its derivative. Projection of a wavefunction onto the first term can be interpreted as measuring its probability amplitude at point $\mathbf{r}_0$, and projection onto second term as measuring its derivative along the i^{th} spatial dimension at the point $\mathbf{r}_0$.

4.1.2 Flux Expectation Value in the Gaussian Basis

To determine the expectation value of the flux operator, we begin by labeling the excited states of the harmonic oscillator at position $\mathbf{r}_0$ oriented along the i^{th} spatial dimension

$$\begin{aligned}
\langle \mathbf{r} | \, 0 \rangle &= \langle \mathbf{r} | \, \mathbf{r}_0, \sigma \rangle \\
\langle \mathbf{r} | \, 1 \rangle &= \frac{\mathbf{e}_1 \cdot (\mathbf{r} - \mathbf{r}_0)}{\sigma} \langle \mathbf{r} | \, \mathbf{r}_0, \sigma \rangle \\
\langle \mathbf{r} | \, 2 \rangle &= \sqrt{\frac{1}{2}} \left(\frac{(\mathbf{e}_1 \cdot (\mathbf{r} - \mathbf{r}_0))^2}{\sigma^2} - 1 \right) \langle \mathbf{r} | \, \mathbf{r}_0, \sigma \rangle \\
&\vdots \quad .
\end{aligned} \tag{4.1.11}$$

These states form a complete set in which the flux operator can be explicitly expressed, using a zero-indexed matrix, as

$$\hat{\jmath}_{\mathbf{r}_0,\sigma,i} = \begin{pmatrix} 0 & +i\lambda & 0 & \cdots & 0 \\ -i\lambda & 0 & 0 & \cdots & 0 \\ 0 & 0 & 0 & \cdots & 0 \\ \vdots & \vdots & \vdots & \ddots & \vdots \\ 0 & 0 & 0 & \cdots & 0 \end{pmatrix} \tag{4.1.12}$$

where $\lambda = \lambda_{\sigma,i,+} = \frac{\hbar}{4m\sigma}$. There are additional sets of harmonic oscillators orthogonal to the above states which are centered at points other than $\mathbf{r}_0$ also with zero components in the flux matrix

The complete set of eigenstates $|\lambda_1\rangle, |\lambda_2\rangle\, |\lambda_3\rangle, \ldots$ of the flux operator expressed in terms of excited states of the harmonic oscillator are solved for

$$\begin{pmatrix} +1 \\ -i \\ 0 \\ \vdots \end{pmatrix}, \begin{pmatrix} +1 \\ +i \\ 0 \\ \vdots \end{pmatrix}, \begin{pmatrix} 0 \\ 0 \\ 1 \\ \vdots \end{pmatrix}, \cdots \tag{4.1.13}$$

with eigenvalues $-\lambda, \lambda, 0, \ldots$. Measurement by the flux operator collapses the wavefunction onto one of these eigenstates, the infinite majority of which are in the degenerate zero-eigenvalue subspace spanning all excited states of the harmonic oscillator above $|1\rangle$. Only the first two eigenstates, confirmed in Eq. 4.1.10, yield non-zero flux values, which, as we have already shown, tend towards positive and negative infinity as $\sigma \to 0$.

When expanding the flux expectation value, we can use the complete eigenbasis to show that

$$\begin{aligned} \left\langle \psi \left| \hat{j}_{\mathbf{r}_0,\sigma,i} \right| \psi \right\rangle &= \left\langle \psi \left| \hat{j}_{\mathbf{r}_0,\sigma,i} \sum_{i=1}^{\infty} \right| \lambda_i \right\rangle \left\langle \lambda_i \middle| \middle| \psi \right\rangle \\ &= \lambda \left| \langle \psi | \, \lambda_1 \rangle \right|^2 - \lambda \left| \langle \psi | \, \lambda_2 \rangle \right|^2 . \end{aligned} \tag{4.1.14}$$

From Eq. 4.1.10, it can be shown that the contributions from $|\langle \psi | \, 0 \rangle|^2$ and $|\langle \psi | \, 1 \rangle|^2$ cancel themselves due to the opposite sign of the eigenvalues, and only the cross-term $\langle \psi | \, 0 \rangle^* \langle \psi | \, 1 \rangle - \langle \psi | \, 0 \rangle \langle \psi | \, 1 \rangle^*$ remains. This form is directly related to the commonlyfound expression of the flux at point $\mathbf{r}_0$ as

$$\mathbf{j}_{\mathbf{r}_0}\left(\Psi(\mathbf{r})\right) = \frac{\hbar}{2mi}\left(\Psi^*(\mathbf{r}_0)\boldsymbol{\nabla}\Psi(\mathbf{r}_0) - \Psi(\mathbf{r}_0)\boldsymbol{\nabla}\Psi^*(\mathbf{r}_0)\right). \tag{4.1.15}$$

By Eqs. 4.1.10 and 4.1.9, we can write the expectation value as

$$\begin{aligned} \left\langle \psi \left| \hat{j}_{\mathbf{r}_0,\sigma,i} \right| \psi \right\rangle &= \frac{i\hbar}{4m\sigma^2}[\langle \psi \left| \mathbf{e}_i \cdot (\mathbf{r}-\mathbf{r}_0) \right| \mathbf{r}_0, \sigma \rangle \langle \psi | \, \mathbf{r}_0, \sigma \rangle^* \\ &\quad - \langle \psi \left| \mathbf{e}_i \cdot (\mathbf{r}-\mathbf{r}_0) \right| \mathbf{r}_0, \sigma \rangle^* \langle \psi | \, \mathbf{r}_0, \sigma \rangle]. \end{aligned} \tag{4.1.16}$$

The traditional flux operator arises from the limit $\sigma \to 0^+$, at which point the two terms in Eq. 4.1.10 become the delta function and its derivative, while the flux values of the first two eigenstates become

$$\lim_{\sigma \to 0^+} \lambda_{\sigma,i,\pm} = \pm\infty. \tag{4.1.17}$$

In addition, there are an infinite number of other eigenstates with zero eigenvalues.

Traditionally, measurements of the flux correspond to the application of the operator and averaging the results. A single application of the flux operator at a particular point in space $\hat{j}_{\mathbf{r}_0,i}$ almost always results in zero, but occasionally in an immensely positive or negative value. It is thus necessary to perform the averaging over an infinite number of measurements to obtain an expression equivalent to the textbook flux.

4.1.3 Connection to Coherent States

The physical meaning of coherent states is straightforward: they describe a semiclassical particle minimizing the product of position and momentum uncertainties. The projection of many coherent states onto a wavefunction over a range of mean positions has come to be called a "Husimi map"[54, 58, 59]. The traditional flux and Husimi measures coincide for small Gaussian spreads, as we now show.

The coherent state is defined as

$$\langle \mathbf{r}|\, \mathbf{r}_0, \mathbf{k}_0, \sigma\rangle = \left(\frac{1}{\sigma\sqrt{\pi/2}}\right)^{d/2} e^{-(\mathbf{r}-\mathbf{r}_0)^2/4\sigma^2 + i\mathbf{k}_0\cdot\mathbf{r}}, \tag{4.1.18}$$

which is a Gaussian envelope over a plane wave $e^{i\mathbf{k}_0\cdot\mathbf{r}}$. Its inner product with a generic wavefunction $\psi(\mathbf{r})$ is

$$\langle \psi|\, \mathbf{r}_0, \mathbf{k}_0, \sigma\rangle = \left(\frac{1}{\sigma\sqrt{\pi/2}}\right)^{d/2} \int \psi(\mathbf{r})\, e^{-(\mathbf{r}-\mathbf{r}_0)^2/4\sigma^2 + i\mathbf{k}_0\cdot\mathbf{r}} d^d r. \tag{4.1.19}$$

Observing that the phase $e^{i\mathbf{k}_0\cdot\mathbf{r}_0}$ is arbitrary, we can Taylor expand the exponential function in the limit of $\mathbf{k}_0\sigma \ll 1$ to produce

$$\begin{aligned}\langle \mathbf{r}|\, \mathbf{r}_0, \mathbf{k}_0, \sigma\rangle &\approx \left(\frac{1}{\sigma\sqrt{\pi/2}}\right)^{d/2} e^{-(\mathbf{r}-\mathbf{r}_0)^2/4\sigma^2} \left(1 + i\mathbf{k}_0\cdot(\mathbf{r}-\mathbf{r}_0)\right) \\ &\approx \langle \mathbf{r}|\, \mathbf{r}_0, \sigma\rangle + i\mathbf{k}_0\cdot(\mathbf{r}-\mathbf{r}_0)\langle \mathbf{r}|\, \mathbf{r}_0, \sigma\rangle . \end{aligned} \tag{4.1.20}$$

Note that the dispersion relation for the free-particle continuum is a circle with radius $k_0 = \frac{\sqrt{2mE}}{\hbar}$, which doesn't depend on the orientation of $\mathbf{k}_0$. The second term in Eq. 4.1.20 is thus proportional to the second term in Eq. 4.1.10 for $\mathbf{k}_0$ projected along the i^{th} dimension. The similarity in form between Eq. 4.1.20 and Eq. 4.1.10 allows us to relate the flux expectation value from Eqs. 4.1.16 and 4.1.16 to coherent state projections as

$$\begin{aligned}\lim_{\sigma k_0\to 0}\left\langle \psi \left| \hat{j}_{\mathbf{r}_0,\sigma,i} \right| \psi \right\rangle &= \frac{\hbar k_0}{4m\sigma^2}[|\langle \psi|\, \mathbf{r}_0, k_0\mathbf{e}_i, \sigma\rangle|^2 \\ &\quad - |\langle \psi|\, \mathbf{r}_0, -k_0\mathbf{e}_i, \sigma\rangle|^2], \end{aligned} \tag{4.1.21}$$

where $\mathbf{e}_i$ is the unit vector along spatial dimension i. The traditional flux *vector* is approximated by taking measurements along each orthogonal direction by rotating $\mathbf{e}_i$.

By the well-known uncertainty relation

$$\Delta x \propto \frac{1}{\Delta k} \propto \sigma, \tag{4.1.22}$$

taking $\sigma \to 0$ results in coherent state measurements with infinite uncertainty in k-space, and zero uncertainty in real space. This is the limit where the traditional flux operates.

4.2 Definition of the Husimi Projection

The properties of coherent states make them a suitable basis for expanding the flux operator to a measurable definition, which we call the Husimi function[54]. It is defined as a measurement of a wavefunction $\psi(\mathbf{r})$ by a coherent state, or "test wavepacket", written as

$$\mathrm{Hu}\left(\mathbf{r}_0, \mathbf{k}_0, \sigma; \psi(\mathbf{r})\right) \;\; = \;\; \left|\langle\, \psi |\, \mathbf{r}_0, \mathbf{k}_0, \sigma \rangle\right|^2 . \tag{4.2.1}$$

Weighting each of these measurements by the wavevector produces a Husimi vector; plotting all Husimi vectors at a point produces the full Husimi projection. These projections are the sunbursts in Fig. 4.2.1, which shows Husimi projections for the wavefunctions

$$\begin{aligned} \Psi_{\mathrm{A}}(\mathbf{r}) &= e^{i\mathbf{k}_1 \cdot \mathbf{r}} \\ \Psi_{\mathrm{B}}(\mathbf{r}) &= \cos\left(\mathbf{k}_1 \cdot \mathbf{r}\right), \end{aligned} \tag{4.2.2}$$

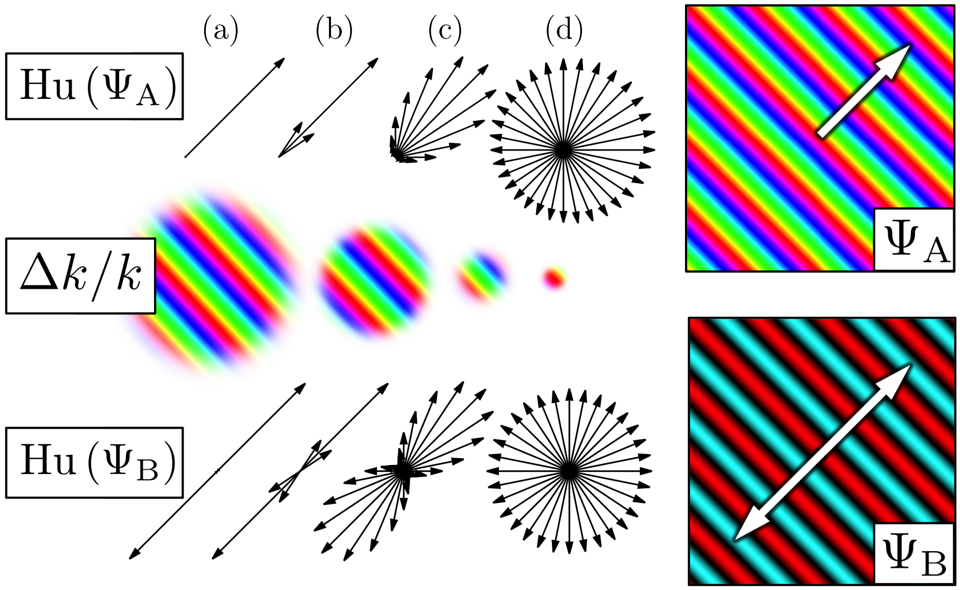

Figure 4.2.1: Husimi vectors for 32 equally-space points in k-space, are shown at left for two wavefunctions at right: the complex plane wave (Ψ_{A}) and the cosine wave (Ψ_{B}) defined in Eq. 4.2.2. The uncertainty for each projection corresponds to $\Delta k/k = 2\%(\mathrm{a}), 10\%(\mathrm{b}), 50\%(\mathrm{c}), 250\%(\mathrm{d})$, corresponding to smaller wavepacket spreads (middle) and less distinction between independent measurements (top and bottom). Above, we represent the coherent wavepacket spread using schematic circles; in general, we indicate the spread precisely using double-arrows.

where $\mathbf{k}_1$ points towards the upper-right. We show the wavevectors that generate each state in the white arrow overlay.

Both wavefunctions are pure momentum states which are not spatially localized, and constitute the building blocks for the wavefunctions addressed in this paper. The plane wave Ψ_{A} is relevant to magnetic field states discussed in Section 4.3.2. The cosine wave Ψ_{B} corresponds to time-reversal symmetric wavefunctions discussed in Sections 4.3.1 and 4.3.3. Both Ψ_{A} *and* Ψ_{B} are important for scattering wavefunctions presented in Section 4.4 which exhibit a mixture of both properties.

Because of the large momentum uncertainty for small σ, coherent state projections merely reproduce the probability amplitude $|\psi(\mathbf{r})|^2$ in all directions of $\mathbf{k}_0$, as seen in Fig. 4.2.1d. The flux emerges as a small residual which can be retrieved by summing each coherent state projection weighted by $\mathbf{k}_0$. We call this quantity the vector-valued Husimi flux,

$$\mathbf{Hu}\left(\mathbf{r}_0, \sigma; \psi(\mathbf{r})\right) = \int \mathbf{k}_0 \left|\langle \psi | \, \mathbf{r}_0, \mathbf{k}_0, \sigma \rangle\right|^2 d^d k_0. \tag{4.2.3}$$

In Appendix A, we show that as $\sigma \to 0$, the contributing points in the integral over k-space reduce to just the orthogonal directions. In this limit, we can write the Husimi flux as

$$\begin{aligned} \lim_{\sigma \to 0} \mathbf{Hu}\left(\mathbf{r}_0, \sigma; \psi(\mathbf{r})\right) \quad \propto \quad & \sum_{i=1}^{d} \mathbf{e}_i [\left|\langle \psi | \, \mathbf{r}_0, k_0 \mathbf{e}_i, \sigma \rangle\right|^2 \\ & - \left|\langle \psi | \, \mathbf{r}_0, -k_0 \mathbf{e}_i, \sigma \rangle\right|^2], \end{aligned} \tag{4.2.4}$$

where $\mathbf{e}_i$ is the unit vector along the i^{th} orthogonal direction, and we sum over d dimensions. By Eq. 4.1.21, both sides of Eq. 4.2.4 are proportional to the traditional flux measured at point $\mathbf{r}_0$ so that

$$\left\langle \psi \left| \hat{\mathbf{j}}_{\mathbf{r}_0} \right| \psi \right\rangle \propto \lim_{\sigma \to 0} \mathbf{Hu}\left(\mathbf{r}_0, \sigma; \psi\right). \tag{4.2.5}$$

For larger σ, reduced momentum uncertainty allows for substantial variation in the coherent state projections between different directions of $\mathbf{k}_0$. This can be seen in Fig. 4.2.1 as uncertainty is reduced and uniform sunbursts (d) contract into lobes (c), and finally to unambiguous vectors (a-b). At all uncertainties, the zero flux that appears in time-reversal symmetric states can be interpreted as the perfect canceling out of coherent state projections along each direction in k-space. The equal participation of counter-propagating flux is absent in Ψ_A and evident in Ψ_B as a reflected sunburst.

While we reduce momentum uncertainty for larger coherent states, we sacrifice spatial resolution. In the intermediate regime, we can use Husimi projections to map the local phase space of a wavefunction. By taking snapshots of the local phase space at many points across a system for larger σ, we can process the result to produce a map of the classical trajectories that correspond to a given wavefunction. These visualizations are known as "Husimi maps"[54, 60, 58, 59]. Like the traditional flux map, Husimi maps can be integrated over lines and surfaces to reveal net current.

Husimi maps also have implications for experiments since they could be measured in a fashion similar to angle-resolved photo-emission spectroscopy (ARPES)[61, 62, 63, 64], which is currently used to obtain measurements of the dispersion relation in a solid. In the ARPES setup, a focused photon beam on a sample kicks off electrons in the valence band. The energy of the photo-emitted electrons incorporates both their bonding energies, which can be averaged over, and their kinetic energy, which depends on the angle of the beam with respect to the sample surface.

The ARPES response function behaves similarly to coherent state projections with $\mathbf{k}_0$ proportional to the beam angle. By rotating the beam angle around the same point of intersection, the response in different directions provides the momentum distribution of the wavefunction at that point. Perturbations from the known dispersion relation can then be inserted into Eq. 4.2.3 to obtain the flux expectation value.

While a narrow beam would make it possible to measure the flux vector at the

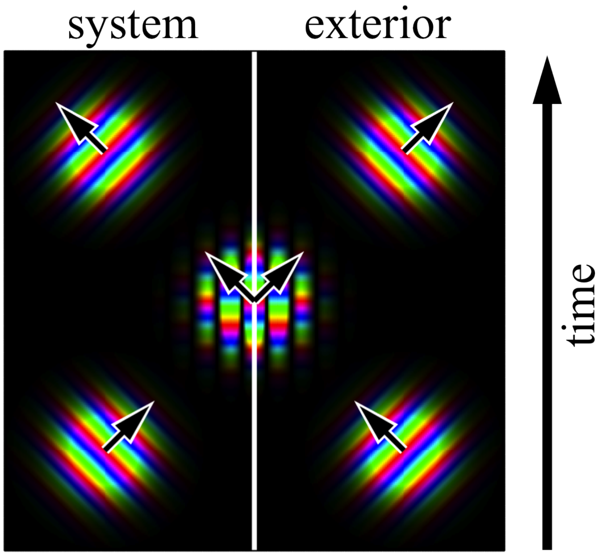

Figure 4.2.2: A coherent state within the system (lower-left) bounces off the system boundary (middle) and reflects into a coherent state with a different wavevector (upper-right). This can also be imagined with the boundary replaced by an image wavepacket (lower-right). When the original wavepacket bounces off the boundary, instead the image wavepacket simply passes through it. In this way, the incoming wavepacket scatters into an outgoing wavepacket, which was originally the image wavepacket.

intersection point, it will be difficult to distinguish the occasional large perturbation measurements from noise. However, wider beams would capture additional terms from the Taylor expansion of the coherent state in Eq. 4.1.20, producing more reliable perturbation measurements. Applying the technique at many points across the sample would then provide the Husimi map and an approximation to the flux map.

A question arises regarding the handling of boundaries in the system, beyond which the wavefunction goes to zero. Our definition causes Husimi projections within distance σ of the boundary to reduce in magnitude. If one imagines a coherent state interacting with a boundary, we can replace the boundary by an image wavepacket (See Fig. 4.2.2). In this case, bouncing off the boundary amounts to scattering between wavepackets with different wavevectors. The reduction in the Husimi projections near the boundaries therefore reflects wavepacket scattering, making it possible to use Husimi maps to compute scattering metrics along the boundary, such as angular deflection in Section 4.2.2.

To produce the Husimi map, we sample Husimi projections along a grid in spatial coordinates, since it is easier to plot, straightforward to interpret, and allows for computing metrics like angular deflection (see Section 4.2.2). However, other schemes may be preferred. In Fig. 4.3.2, for example, we sample along classical trajectories to emphasize the quantum-classical correspondence. While this paper addresses two-dimensional systems, Husimi projections are equally applicable for higher-dimensional systems.

4.2.1 Multi-Modal Analysis

The Husimi projections in Fig. 4.2.1 reveal that even a single plane wave produces a range of Husimi vectors because of the finite spread of the wavepacket. Can distinct trajectories intersecting at a point be distinguished unambiguously? If the dominant plane waves at a point are sufficiently separated in k-space that the momentum uncertainty of the coherent state can resolve between them, we can retrieve them numerically using the Multi-Modal Algorithm (Algorithm 4.1). This analytical tool can be especially useful for time-reversal symmetric systems where both the traditional flux and the Husimi flux are identically zero.

Figs. 4.2.3 demonstrates the algorithm on the pure momentum state

$$\Psi_{\mathrm{C}}(\mathbf{r}) = \alpha \cos\left(\mathbf{k}_1 \cdot \mathbf{r}\right) + \beta \cos\left(\mathbf{k}_2 \cdot \mathbf{r}\right), \tag{4.2.6}$$

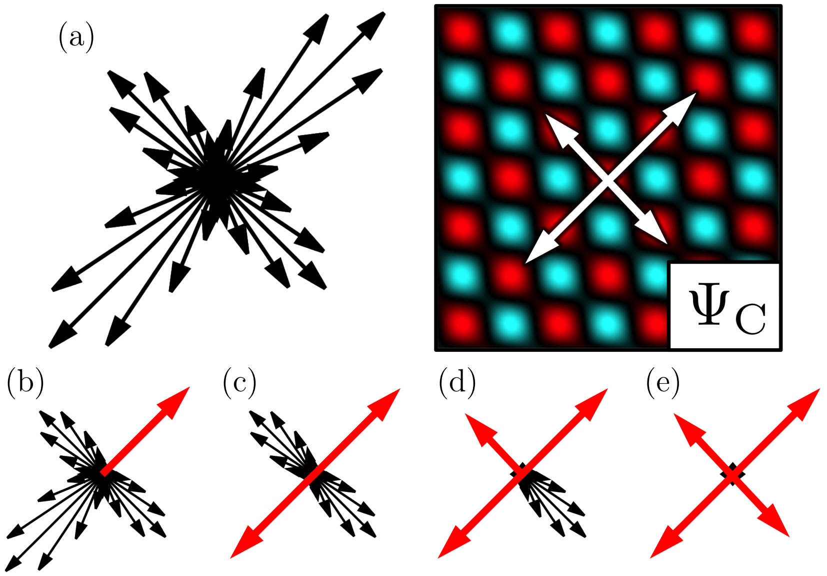

Figure 4.2.3: Husimi vectors for 32 equally-space points in k-space are shown (a) for the double cosine waves (Ψ_C) from Eq. 4.2.6. The uncertainty for each projection corresponds to $\Delta k/k = 30\%$. As the multi-modal algorithm (Algorithm 4.1) loops through each iteration (b-e), a trajectory is matched and then subtracted from the full Husimi projection, until all major trajectories are approximated by their appropriate values.

where $\mathbf{k}_1$ points towards the upper-right and $\mathbf{k}_2$ points towards the upper-left. We set $\alpha = 1$ and $\beta = 0.8$. In Fig. 4.2.3a, the Husimi projection is shown with a sizable uncertainty of $\Delta k/k = 30\%$. Parts b-e iterate through the *for* loop in steps 1-6 of the Multi-Modal Algorithm. At each iteration, the most dominant plane wave in the sunburst is modeled and then subtracted from the projection. This is repeated until all major plane waves have been approximated.

If the dominant trajectories intersecting at a point have sufficiently divergent momenta, not only does the algorithm do an excellent job of modeling them, it can even compute how many there are. In general, we stop the loop in Step 7 after a certain number of iterations to make clearer figures.

Algorithm 4.1 Multi-Modal Analysis

1. A set of Husimi templates on N wavevectors $\{\mathbf{k}_j\}$ is created for the wavefunctions $\Psi = e^{i\mathbf{k}_i^{\text{test}}\cdot r}$ generated by the M wavevectors $\{\mathbf{k}_i^{\text{test}}\}$. Both sets of wavevectors lie along the dispersion contour. Each template can be stored as a vector of values $\mathbf{u}_i$ of length M where each member corresponds to the Husimi function along the wavevector $\mathbf{k}_j$.
2. Writing the Husimi projection as the vector $\mathbf{v}$, a metric is computed $d_i = \mathbf{v}\cdot\mathbf{u}_i$ for each Husimi template.
3. The maximum of the set $\{d_i\}$ is determined, and both the wavevector $\mathbf{k}_i^{\text{test}}$ and the dot product d_i are stored.
4. The contribution of the trajectory with wavevector $\mathbf{k}_i^{\text{test}}$ is determined by the re-weighted vector $\mathbf{u}_i\frac{d_i}{\mathbf{u}_i\cdot\mathbf{u}_i}$.
5. The re-weighted template vector is subtracted form the projection, that is, $\mathbf{v}\to\mathbf{v}-\mathbf{u}_i\frac{d_i}{\mathbf{u}_i\cdot\mathbf{u}_i}$.
6. All elements of $\mathbf{v}$ which are now negative are set to zero.
7. Steps 1-6 are repeated until the metric d_i dips below a threshold.
8. The set of vectors $\{d_i\mathbf{k}_i^{\text{test}}\}$ are used to approximate the Husimi projection

On the other hand, when there are a number of trajectories of equal weight whose momenta cannot be resolved by the coherent state, Algorithm 4.1 can produce unexpected results. An example of unresolved trajectories is seen in the points sampled along the perimeter of Fig. 4.3.1a and in the central regions of Figs. 4.3.1b-d and 4.3.2. In these cases, the Multi-Modal Algorithm approximates overlapping trajectories by first choosing their average, and then contributing additional trajectories on either side.

Even when the traditional flux is non-trivial, as in Fig. 4.3.5 and magnified in Fig. 4.3.6a, it can only produce an average of the trajectories at a point. For this reason the multi-modal analysis improves upon the flux operator even when the flux is non-zero, since the paths indicated by the flux map can be misleading. For example, in Sec. 4.3.2, we compare the trajectories highlighted by the flux to the classical paths and the multi-modal analysis for the same system.

4.2.2 Angular Deflection and Boundary Effects

The Husimi map makes it possible to compute other quantities tied to the underlying classical dynamics of a quantum wavefunction. This chapter focuses on one: angular deflection, which shows where system boundaries and external fields deflect classical trajectories from straight paths. Other metrics appear in Chapter 5.

We begin by considering the Husimi function for one point in k-space measured at equally-spaced points on a grid that covers the system. The scalar field yields a spatial map of the presence of an individual trajectory angle, and fluctuations in the map indicate points where classical paths deflect away from and towards the angle. Summing the results for all wavevectors along the contour line defined by system energy in the dispersion relation, we can derive a measurement of angular deflection $Q\left(\mathbf{r};\Psi\right)$ written as

$$Q_{\text{ang.}}\left(\mathbf{r};\Psi\right) = \int D_{\text{abs.}}(\mathbf{r},\mathbf{k};\Psi) k d^d k. \tag{4.2.7}$$

$D_{\text{abs.}}\left(\mathbf{r},\mathbf{k};\Psi\right)$ is the absolute Gaussian-weighted divergence of the Husimi map for wavevector $\mathbf{k}$, written as

$$D_{\text{abs.}}\left(\mathbf{r},\mathbf{k};\Psi\right) = \int \sum_{i=1}^{d} \left| \frac{\text{Hu}\left(\mathbf{k},\mathbf{r}';\Psi\right) - \text{Hu}\left(\mathbf{k},\mathbf{r};\Psi\right)}{\left(\mathbf{r}'-\mathbf{r}\right)\cdot\hat{e}_i} \right| \exp\left[\frac{\left(\mathbf{r}'-\mathbf{r}\right)^2}{2\sigma^2}\right] d^d r'. \tag{4.2.8}$$

where we sum over the d orthogonal dimensions each associated with unit vector $\hat{e}_i$.

Using the Husimi map to measure angular deflection has close ties to its initial introduction as a measurement state for building phase diagrams[54]. It is possible, for instance, to use the divergence of the Husimi map for each wavevector to compute a state's Poincare map[65] without requiring numerical ray-tracing algorithm to propagate in time. This form of the Husimi map has been used to examine the angle of impact against a coordinate along the boundary[65] to study chaotic behavior in stadium billiards[66, 67].

Angular deflection is useful for examining the role of boundaries and external potentials in forming the shape and properties of a given wavefunction. This chapter will examine these effects in Sections 4.3.1, 4.3.2, and 4.3.3.

When modeling a wavefunction using coherent states, questions arise around how to handle boundaries. For instance, as the coherent state extends beyond the system, part of its amplitude fails to contribute to the Husimi function. This causes Husimi maps to diminish in magnitude within a distance σ of the boundary. Should the projections near the boundary be compensated to account for this effect?

For this thesis, we have elected not to, on grounds that keeping the original definition of the Husimi function consistent across the entire system provides a more-accurate analysis. It is also under this basis that angular deflection can be properly defined.

4.3 Examples in Closed Systems

This section examines eigenstates of closed systems that are generated using the tight-binding finite-difference Hamiltonian as defined in Subsection 1.1.2 and the standard sparse eigensolvers.

4.3.1 Eigenstates of the Circular System

The circular well is an ideal system for demonstrating the Husimi map since their classical dynamics are simple and can be analytically determined.

The Schrodinger equation can be written in radial form as

$$\frac{d^2R(r)}{dr^2} + \frac{1}{r}\frac{dR(r)}{dr} + \left(k^2 - \frac{m^2}{r^2}\right) R(r) = 0. \tag{4.3.1}$$

Solutions to this equation are simultaneous eigenstates of energy and angular momentum, and thus possess the good quantum numbers n (number of nodes in the radial direction) and m (number of angular nodes). Fig. 4.3.1a-c shows three such states, the first with $n = 0$, the second with $n \gg m$, and the third with $n \approx m$. The Husimi map in each shows the clear distinction between angular and radial components of the wavefunction, and how they correlate with classical paths with similar properties (further discussion of the classical correspondence can be found[68]).

To examine the harmonic oscillator state in Fig. 4.3.1d, the Husimi projection at each point must be modified. For the circular well, the dispersion relation is $\hbar k = \sqrt{2mE}$, but due to the harmonic potential, it changes to $\hbar k(\mathbf{r}) = \sqrt{2m(E - V(\mathbf{r}))}$. This means that a different sweep in k-space must be made at each point to produce an accurate Husimi map. Fig. 4.3.1d shows such a state with $V(\mathbf{r}) = V_0 r^2$.

The Husimi vectors in Figs. 4.3.1c align to suggest straight trajectories, but the vectors in Fig. 4.3.1d do not, suggesting the presence of curved paths. Moreover, projections near the boundaries of both systems indicate that the paths of the circular

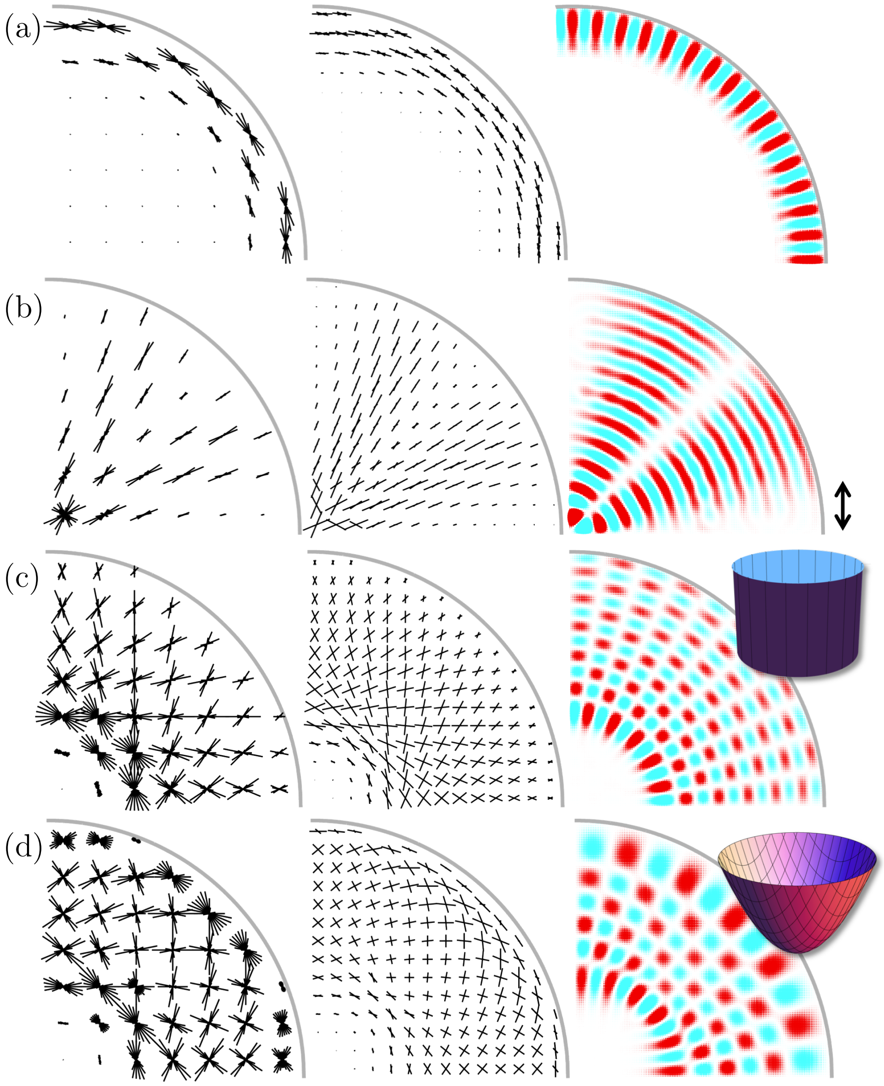

Figure 4.3.1: Husimi maps (left), multi-modal analysis (middle), and the wavefunction (right) are shown for eigenstates of the circular well (a-c) and the harmonic oscillator (d). Double-arrows at far right indicate the spread of the coherent state which is $\Delta k/k = 10\%$. The states in (c) and (d) correspond to the classical paths in Figs. 4.3.2a and b respectively.

well bounce off the boundary with a consistent and acute angle, while they graze the edge of the harmonic oscillator.

Because there are so many trajectories occurring simultaneously, however, it is difficult to evaluate how closely the Husimi map corresponds to an individual classical path. In this chapter and later in Chapter 5, we have chosen to sample the Husimi projections at equally-spaced points along a grid, which makes it possible to compute quantities such as the angular deflection. If we instead sample along one of the classical paths corresponding to the state, we find a set of Husimi vectors which align themselves perfectly with the classical path. We show these two approaches in Figs. 4.3.2a and 4.3.2b, which correspond to the wavefunctions in Figs. 4.3.1c and 4.3.1d respectively.

Each Husimi projection in Fig. 4.3.2b contains an additional set of Husimi vectors which don't align with the path. These vectors can be understood by considering that wavefunctions for the circular well and harmonic oscillator actually correspond to infinitely many such paths rotated in space due to the circular symmetry of these systems, which we indicate in Fig. 4.3.2c. The "cross-hatching" patterns in Fig. 4.3.2a-b arise because two rotated classical paths intersect at any point.

Towards the center of the system, a large number of paths come into close proximity. Even though an infinitesimal point is intersected by only two paths, the finite spread of the coherent state is sensitive to other paths nearby, giving rise to Husimi projections showing a large number of trajectories with similar angles. These points in a wavefunction can violate assumptions of the multi-modal analysis in Section 4.2.1. As a result, the multi-modal analysis in Figs. 4.3.1c and 4.3.1d does not produce the

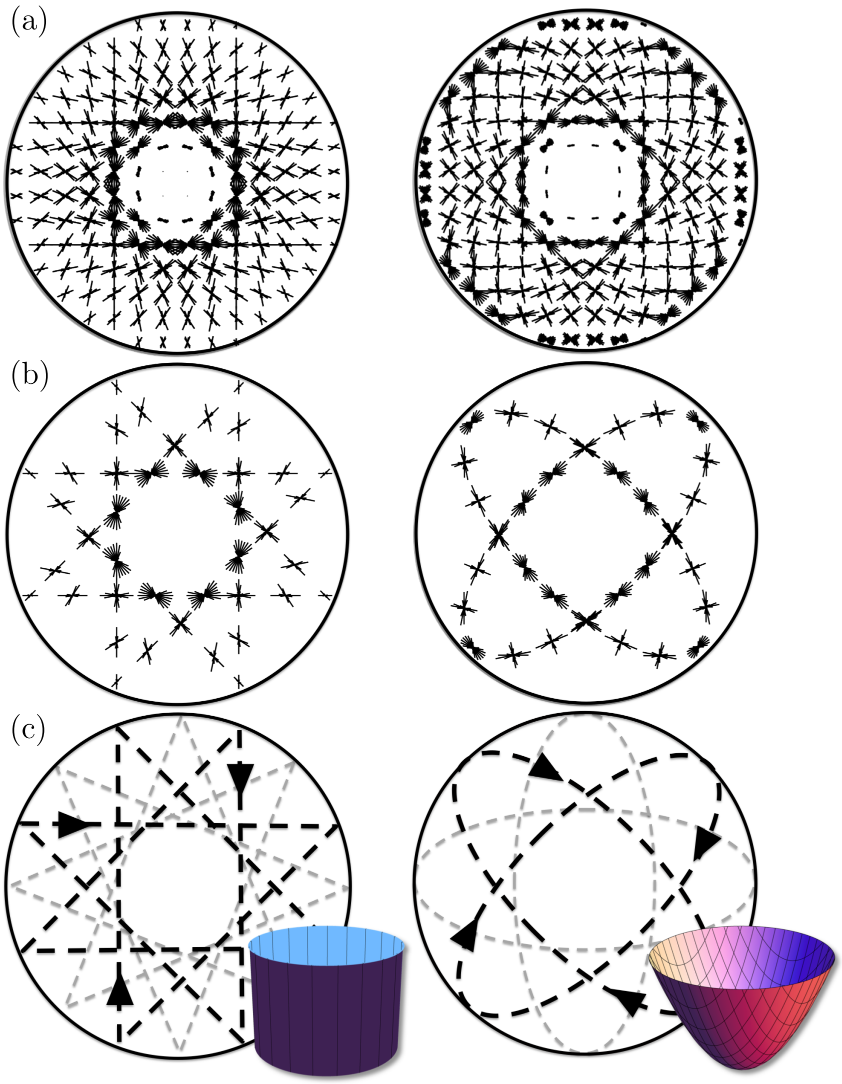

Figure 4.3.2: Where the Husimi map is sampled in space can dramatically alter its appearance. In part (a), the Husimi map is shown for the two eigenstates in Fig. 4.3.1c-d, where Husimi projections are sampled along a grid. In part (b), projections are instead sampled along classical paths that correspond to the wavefunction. Because of rotational symmetry, however, the wavefunction is actually created by the sum of many rotations of such paths, as indicated in part (c).

original paths, but their average and approximations on either side.

4.3.2 Magnetic Field

Systems without time-reversal symmetry can also be studied with the Husimi technique as shown below for systems in the presence of a magnetic field. To properly reflect these states, both the momentum operator in Eq. 4.0.1 and the momentum term $i\mathbf{k}_0 \cdot \mathbf{r}_0$ in Eq. 4.2.3 must be modified to reflect the canonical transformation

$$\mathbf{p} \to \mathbf{p} - q\mathbf{A}/c, \tag{4.3.2}$$

where the magnetic potential $\mathbf{A}$ is defined below.

To apply magnetic fields to our Hamiltonian, we use the Peierls substitution[69], wherein the magnetic field contributes a phase to the hopping potential t in Eq. 1.1.12 according to

$$t_{ij} = t \exp\left[i\phi\right], \phi = q\mathbf{A} \cdot (\mathbf{r}_i - \mathbf{r}_j)/\hbar, \tag{4.3.3}$$

where $\mathbf{r}_i$ is the position vectors of the site corresponding to the i^{th} column of the Hamiltonian, $\hbar$ is Planck's constant, and q is the electron charge. Calculations in Subsection 4.3.2 assume that the magnetic field is perpendicular to the plane on which the system sits and is bounded by a cylinder centered on the system's center. The radius of this column is chosen to be greater than the size of the system. Accordingly, the gauge of the magnetic potential for an out-of-plane magnetic field is defined such that

$$\mathbf{A}(\mathbf{r}) = \frac{\mathbf{e}_\theta}{2\pi r} \int B_z dxdy, \tag{4.3.4}$$

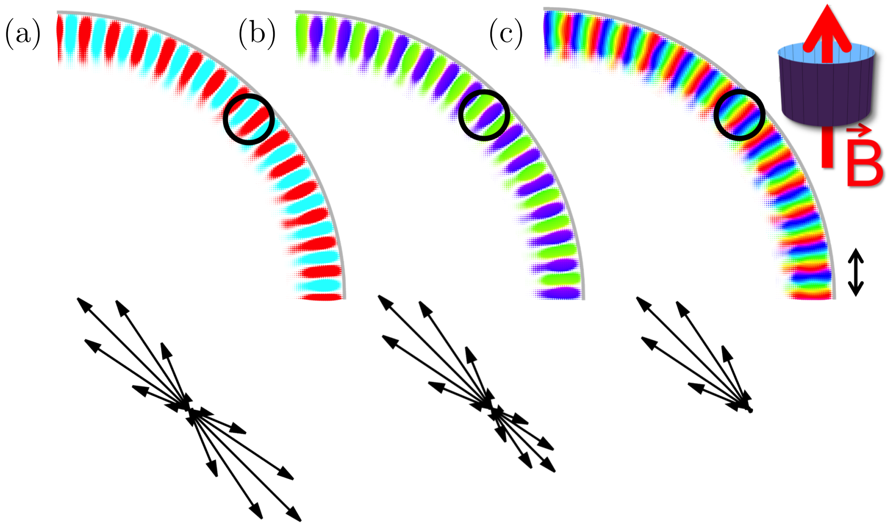

Figure 4.3.3: The eigenstates are plotted for the upper-right-hand corner of a circular system with Dirichlet boundary conditions. The Husimi projection below is taken from the point indicated by the black circle. The uncertainty for each projection is 10% and each wavefunction has a similar energy (the same number of wavelengths along its perimeter). The magnetic fields for each row are $B_0 = 0$(a), 1.5×10^{-7}(b), and $1.5 \times 10^{-6}\frac{\hbar}{qa^2}$(c). The Husimi projection reflects the lifting of time-reversal symmetry in a gradual process that emphasizes one lobe over the other as the magnetic field is increased.

where the integral is over a disc centered on the origin and limited by radius r.

The cyclotron radius can be determined by the relation

$$r = \frac{\hbar k}{B_0 q}. \tag{4.3.5}$$

For a free particle, $\hbar k = \sqrt{2mE}$, giving

$$\frac{r}{a} = \frac{\sqrt{2mE}}{B_0 q a^2}. \tag{4.3.6}$$

This means that at $E = 0.2\frac{\hbar^2}{ma^2}$, a magnetic field strength of $B_0 = 2 \times 10^{-3}\frac{\hbar}{qa^2}$ is sufficient to produce a cyclotron radius that is 2/3 of the system radius. This relation is used to predict the cyclotron radius for all calculations in this section.

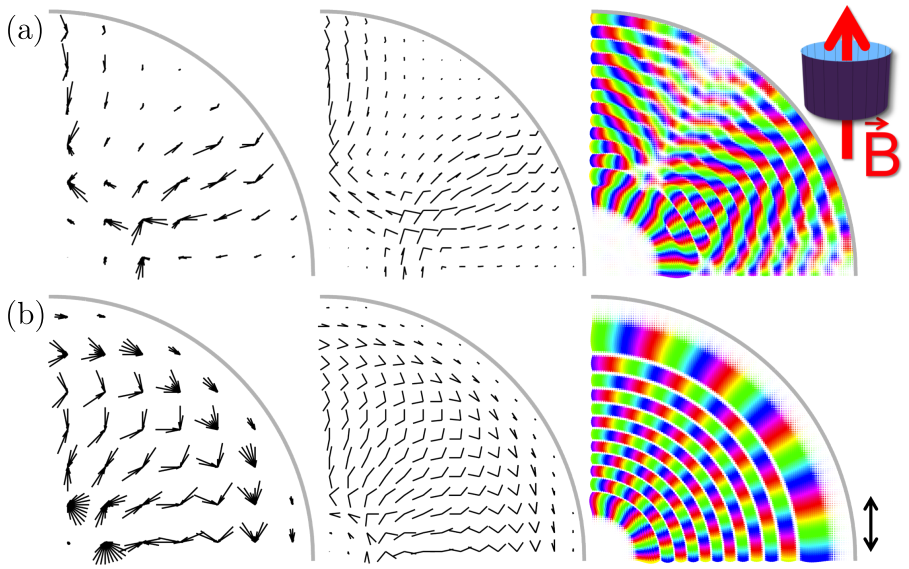

Figure 4.3.4: Husimi map (left), multi-modal analysis (middle), and the wavefunction (right) are shown for two eigenstates of the circular well with magnetic field vectors coming out of the plane. The magnetic field strength is set so that the cyclotron radius is approximately 1/2(a) and 1/3(b) of the the system radius. Double-arrows at far right indicate the spread of the coherent state which is $\Delta k/k = 10\%$. These states correspond to the classical paths discussed in Fig. 4.3.5.

In Fig. 4.3.3, the Husimi projection reveals that as we increase the strength of the magnetic field from zero, the phase difference between counter-propagating paths grows, which is proportional to the flux. This is expressed in the Husimi projection as one of the lobes shrinks to zero while the wavefunction shifts from real to complex values.

Results for large magnetic fields, such as when the cyclotron radius is smaller than the system size, are presented in Fig. 4.3.4. The classical trajectories for these systems are circular with radii corresponding to the cyclotron radius, which the Husimi map is perfectly capable of revealing. In Fig. 4.3.5, the full classical paths corresponding to each state are depicted, and correlate strongly with the Husimi map with the canonical transformation.

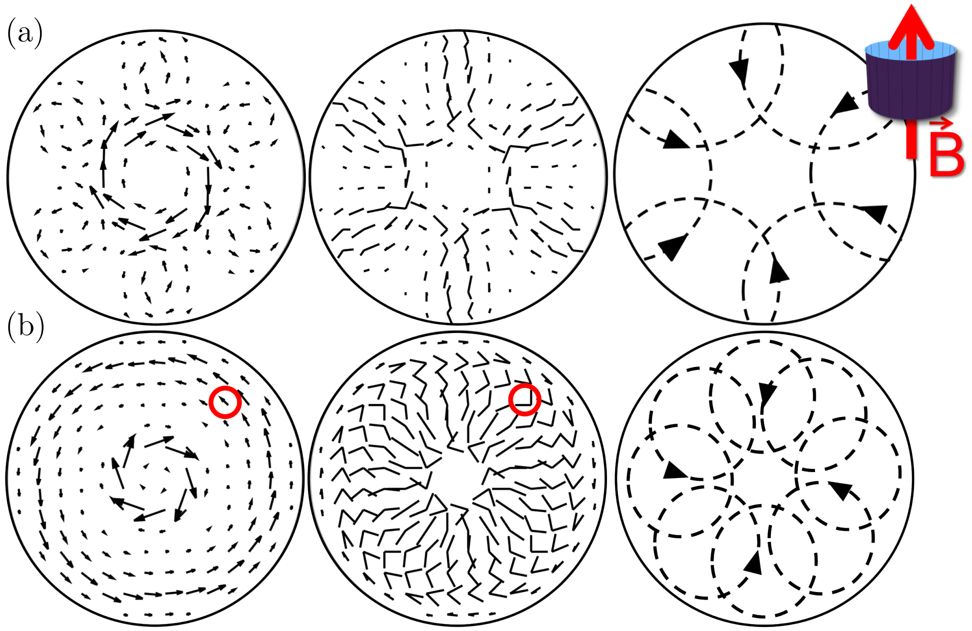

Figure 4.3.5: The flux map, multi-modal analysis, and classical paths are shown for the states represented in Fig. 4.3.4(a-b). The traditional flux correlates strongly with Husimi flux (Eq. 4.2.3) but fails to show the classical paths suggested by the wavefunction. Red circles correspond to magnified views in Fig. 4.3.6.

The Husimi projection can obtain information about the dynamics of the system that is lost in the conventional flux analysis. In Fig. 4.3.6, magnified views from the flux operator, multi-modal analysis, and full Husimi map corresponding to the red circles in Figs. 4.3.4 and 4.3.5 are shown. We model this point in the wavefunction according to the pure momentum state

$$\Psi_{\mathrm{D}}(\mathbf{r}) = e^{i\mathbf{k}_3\cdot\mathbf{r}} + e^{i\mathbf{k}_4\cdot\mathbf{r}}, \tag{4.3.7}$$

where $\mathbf{k}_3$ and $\mathbf{k}_4$ are indicated by the white arrows. While the multi-modal analysis is able to properly identify two independent trajectories, the flux merely averages them. The left column of Fig. 4.3.5, which shows the flux map, integrated with a Gaussian kernel corresponding to the coherent state used to generate the Husimi map,

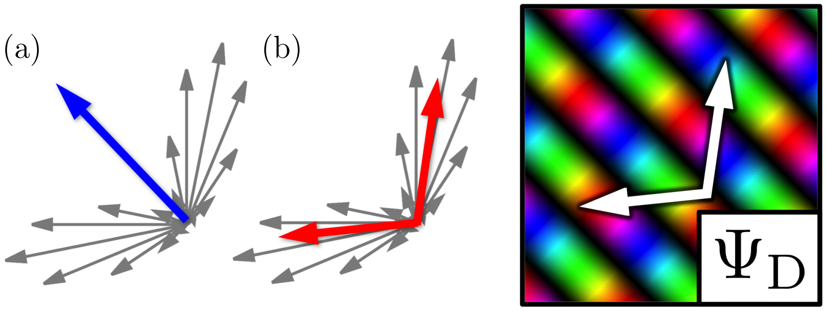

Figure 4.3.6: Husimi vectors for 32 equally-space points in k-space are shown in grey for the double plane waves Ψ_{D} defined in Eq. 4.3.7. The uncertainty corresponds to $\Delta k/k = 30\%$. The flux operator (a) averages the trajectories, but the multi-modal analysis (b) accurately reflects them. Ψ_{D} is representative of the points circled in red in Fig. 4.3.5.

is consequently unable to represent the classical paths (right column). In contrast, the multi-modal analysis in the middle column indicates these paths with remarkable fidelity.

4.3.3 Stadium Billiard Eigenstates

The dynamics of the circular stadium are integrable while those of the Bunimovich stadium[70] are chaotic. As a result, their dynamics have been featured prominently in previous studies [71, 72, 73, 74, 75, 65] .

Fig. 4.3.7 shows three Husimi maps for a billiard eigenstate. The wavelength at the energy of the eigenstate is much shorter than the size of the system, allowing well-defined scars to form, which are spawned by modestly unstable and rare (among all the chaotic orbits) classical periodic orbits[76].

For Fig. 4.3.7a, an extended coherent state is used to generate the Husimi map, so that many fine features of the wavefunction are washed out. Only the scar path

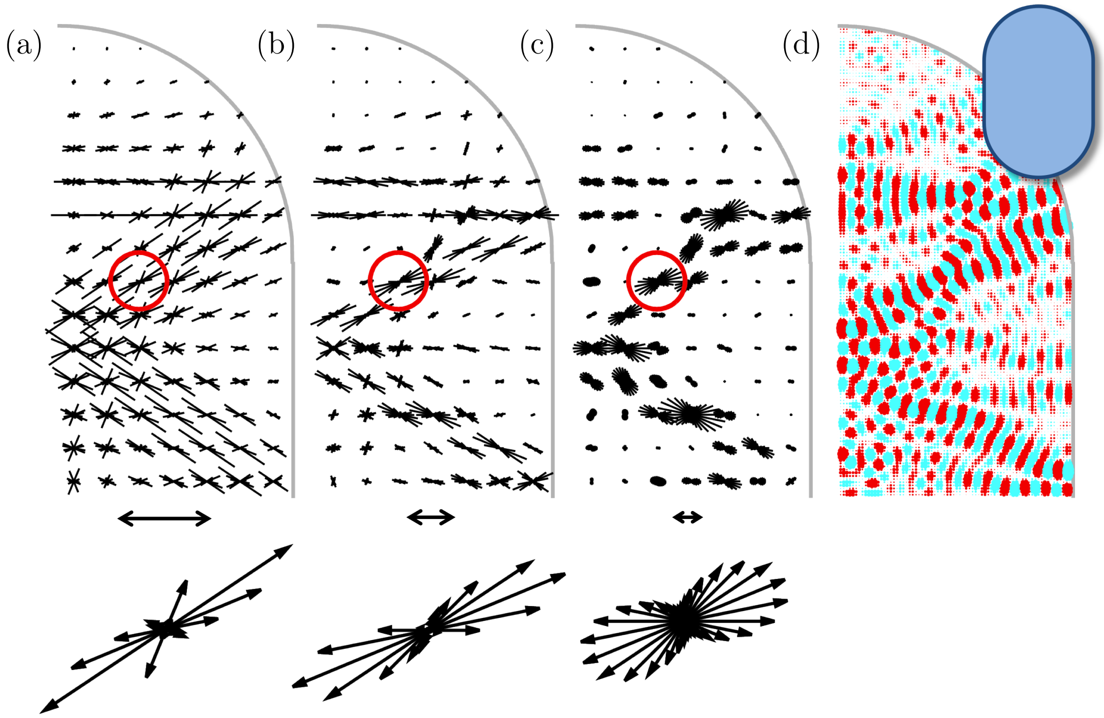

Figure 4.3.7: Husimi maps for the scarred stadium billiard eigenstate (d, from Fig. 3.0.1) are shown. Each map uses a different spread of the measurement wavepacket. The spread is indicated by the double-arrows on the bottom, with relative uncertainties of $\Delta k/k = 5\%$(a), 20%(b), and 50%(c). A single Husimi projection, circled in red, is magnified at the bottom of each representation.

(seen as a rotated “v” pattern in the depiction) is clearly visible. The sharply peaked Husimi sunburst reflects both the low momentum uncertainty of the Gaussian used and the strong dominance of the periodic orbit pathway in the eigenfunction.

Compare this to the Husimi map in Fig. 4.3.7c which is generated by a small coherent state with larger momentum uncertainty. Here, each Husimi projection is more ambiguous, and local variations in the wavefunction probability amplitude have a large impact on the representation, making it very sensitive to the sampling of the visualization. The trajectories implied by the map no longer continue from one projection to its neighbors and appear strongly irregular since the distance between each sampling point is several times larger than the coherent state.

In general, a compromise can be made by choosing an intermediate momentum uncertainty, as shown in the Husimi map presented in Fig. 4.3.7b. Trajectories are fairly well-resolved, and local variations are easy to follow. Coherent states of this size provide the clearest representation of semiclassical paths.

Even at low energies, where the wavelength is comparable to the size of the system, stadium billiards provide another angle on the utility of the Husimi map. Unlike the circular system, in which the trajectories adding up at a particular point are fairly regular and predictable, any point in a stadium billiard eigenstate is rife with many unpredictable trajectories, making the Husimi map an ideal tool for lifting the veil on the underlying classical dynamics.

Fig. 4.3.8 considers three eigenstates of the closed stadium billiard Hamiltonian. For each calculation, the size of the coherent state is kept constant, but because the energy of these eigenstates changes, so does the corresponding uncertainty for each Husimi projection. This can be seen by the increase in precision as plots go up in energy, as well as the reduction of angular deflection in the bulk (which acquires small positive values in the top figure due to uncertainty, not because there is actual deflection at these points).

To the unaided eye, the wavefunctions in Fig. 4.3.8 do not appear to emphasize a few classical trajectories like the high-energy stadium state in Fig. 4.3.7, especially since at such low energies the system only accommodates a few wavelengths along its diameter. In the Husimi map, however, it is quite clear that a very limited set of classical trajectories are largely responsible for these wavefunctions, suggesting that

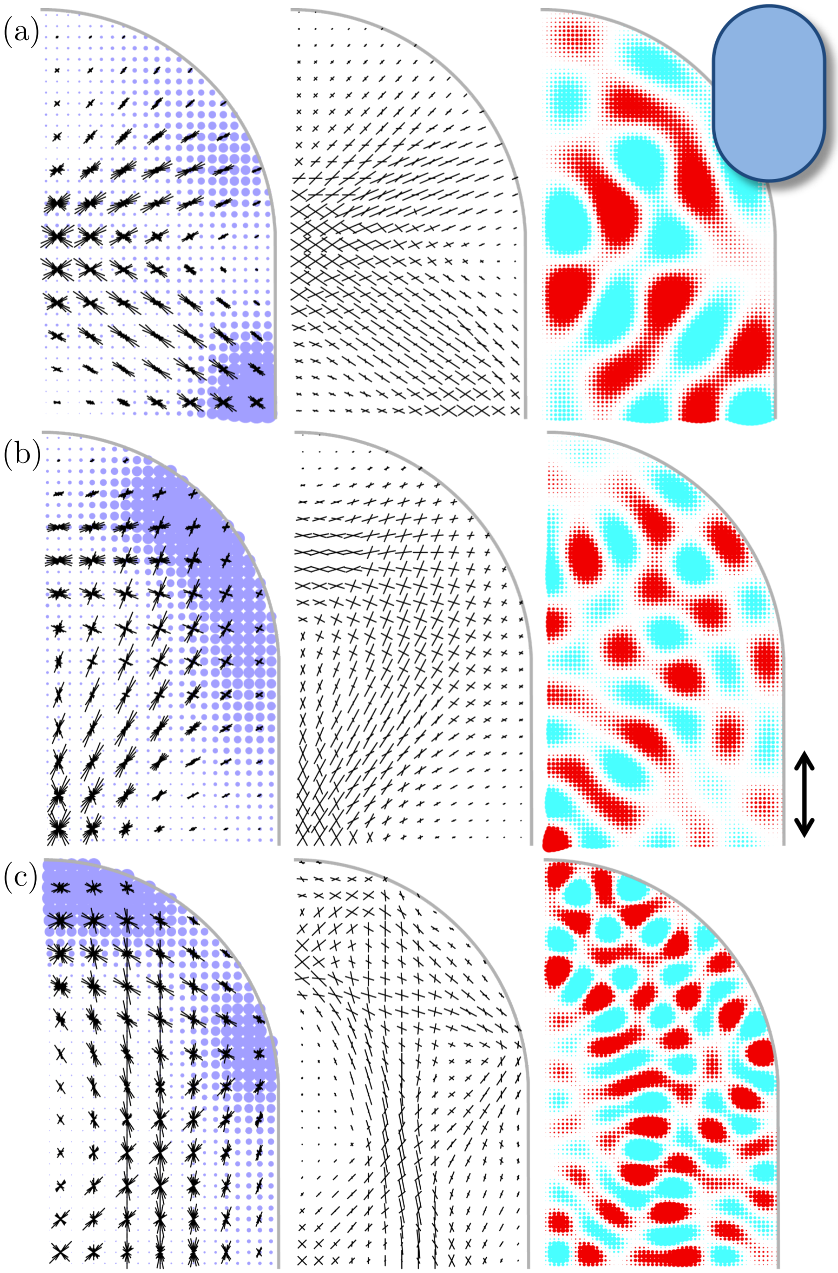

Figure 4.3.8: Three eigenstates of the stadium billiard system with Dirichlet boundary conditions are shown at three increasing energies. The Husimi map (left), multi-modal analysis (middle) and wavefunction (right) are shown. Angular deflection is indicated in blue, and the double arrows indicate the test wavepacket spread of $\Delta k/k = 20\%$(a), 15%(b) and 10%(c).

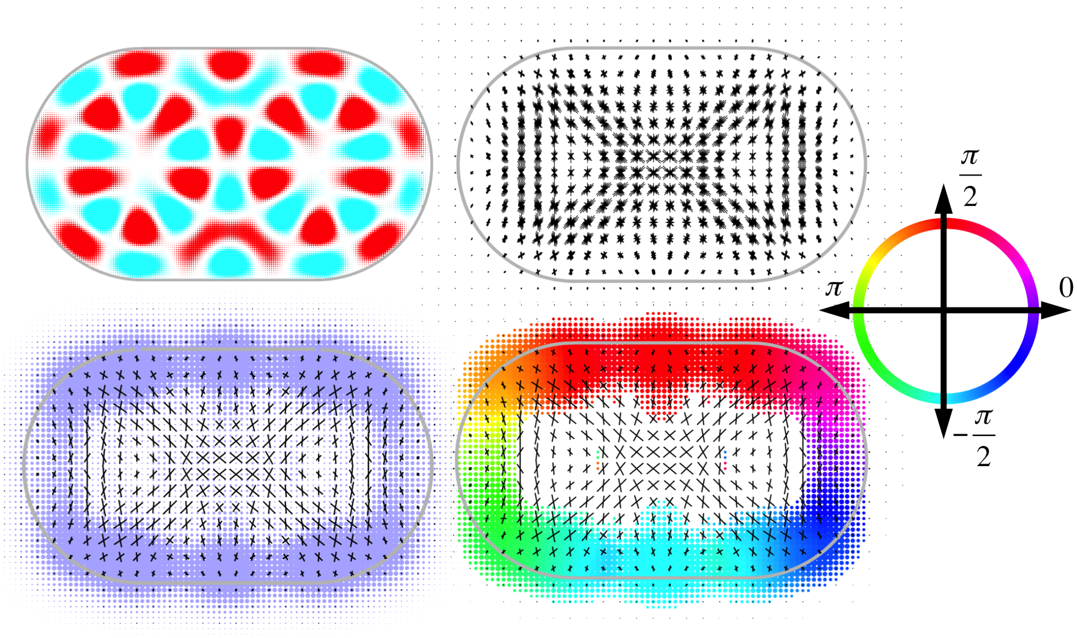

Figure 4.3.9: Another eigenstate from the system in Fig. 4.3.8 is shown, with the wavefunction (upper-left), extended Husimi map (upper-right), and multi-modal analysis (both lower-left and lower-right). Angular deflection is shown in blue. In the lower-right, the average incident scattered wavevector is indicated in color, corresponding to the color-wheel at the far-right.

Husimi projections could be used to study the properties of low-energy scar states[76].

Points with high angular deflection show which parts of the system boundary are responsible for the creation of each state, and indicate where adiabatic changes in the boundary conditions are most likely to affect the state[77, 78]. This can be imagined as a quantum force on the boundary. Because the size of the coherent state used to generate each Husimi map is kept constant, the angular deflection penetrates into the bulk to the same extent for each state. However, the locations of high angular deflection along the boundary form a unique fingerprint for each state.

Elaborating on Sec. 4.2.2 and Fig. 4.3.8, we show another eigenstate from the same system but at a lower energy. To properly define the angular deflection, and later divergence, all Husimi maps in this thesis are actually calculated over the system and all points outside it within 3σ of the system boundary, although we only plot points that fall within the system. As a result, angular deflection, which is a gestalt metric of coherent-state scattering, is concentrated along the boundary, and penetrates both within and without the system. As mentioned in Sec. 4.2.2, we can coordinate the scattered angles at each point. In the lower-right of Fig. 4.3.9, we color the angular divergence by the average absolute incoming angle. This correlates strongly with the absolute angle of the boundary, as expected for specular reflection. At higher energies, other relationships in scattering angles may emerge as a result of internal Bragg diffraction (See Sec. Section 3.5), although we do not explore them in this thesis.

4.4 Flux Through Open Systems

The previous section used the Husimi map to examine the semiclassical dynamics of closed systems directly from their wavefunctions, providing substantial benefits over the flux operator which is either zero or averages over local trajectories. Moreover, the spread of the coherent state used to generate the Husimi map gives it the flexibility to examine dynamics at a variety of scales, while the flux operator is confined to the limit of infinitesimal spread. In its traditional guise (Eq. 4.0.1), the flux operator is most often employed in scattering problems which arise when a closed system is coupled to an environment. Is it possible to connect the semiclassical dynamics of the closed system to the open system using the extended Husimi flux?

In this section, we demonstrate how the Husimi flux can help interpret the traditional flux and deepen our understanding of transport across a device. We first consider sub-threshold resonance for a waveguide that is slightly widened along a short section. This simple system reveals a rich set of phenomena for which the Husimi flux proves ideal as an analytical tool, since the Husimi map can provide insight where the flux and wavefunction cannot. We then move onto flux through a strongly constricted device, and show how the Husimi map can help us understand the nature of flux vortices, and cut through them to reveal the direct channel of transport.

4.4.1 Sub-Threshold Resonance

In an unperturbed waveguide, transport occurs through transverse modes which open for transport when the system energy exceeds the transverse energy of the mode. At these energies, the transmission function exhibits distinct plateaus as seen in Fig. 4.4.1, where the plot of the transmission for a wide(narrow) waveguide is presented in red(blue).

If a small section of a narrow waveguide is widened, the transverse energy of each mode diminishes in the wider section. Thus, for each mode, there is a range of energies bounded above by its transverse energy in the unperturbed waveguide, and below by its energy in the wider region. In this energy range, the mode can reside in the wider region but cannot propagate through the narrower leads. This forces it into a quasi-bound state which is trapped in the wider region and is only weakly coupled to the environment, causing a striking peak in the density of states. In the quasi-bound state, the particle bounces vertically between the walls of the perturbed

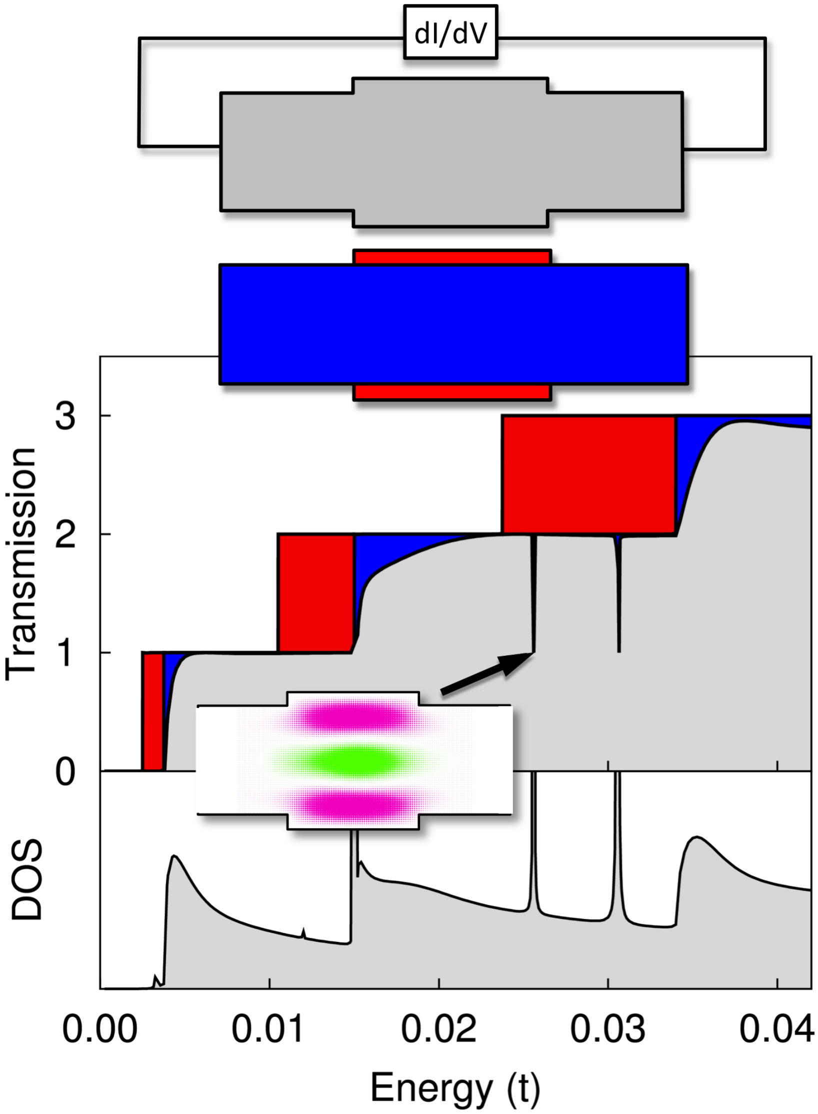

Figure 4.4.1: Top: An infinite waveguide schematic shown with a slight bulge in the middle (grey). This can be modeled as two waveguides of different widths (blue and red). Bottom: In an infinite waveguide, the transmission curve has a series of plateaus as each transverse mode opens up (blue transmission curve). In a wider waveguide, each mode opens up at lower energies (red curve). If only a small segment of the waveguide is widened, then sub-threhold resonances occur in between the energies of the narrow and wide waveguides (grey transmission curve). These correlate with sub-threshold resonant states which peak in the density of states (DOS) at those energies (grey curve). Energy is given in units of t where $4t$ is the band edge.

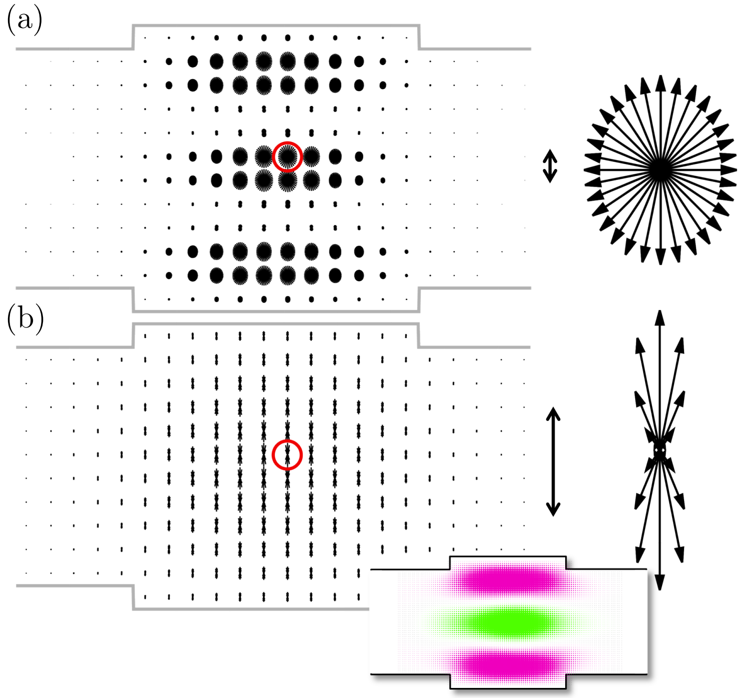

Figure 4.4.2: The full Husimi map for the resonant state (see inset) is plotted with $\Delta k/k = 100\%$ (a) and $\Delta k/k = 20\%$ (b). The spread of the test wavepacket is indicated by double-arrows. A single Husimi projection (circled in red) for each map is magnified at right. The vector sums of each map are shown in Figs. 4.4.4b.

region and is unlikely to escape.

At certain energies, a particle propagating in a lower energy mode corresponding to the narrow section interacts with the wider region and becomes trapped in the quasi-bound state. This causes the quasi-bound state to hybridize with the propagating mode and interfere with the transmission in this device, as seen in Fig. 4.4.1. The suppression of transmission appears as a pair of sharp dips, accounting for symmetric and antisymmetric versions of the quasi-bound state. Since it is the hybridized state which inhabits the system at resonance, we refer to it as the resonant state.

Since a resonant state “traps” the wavefunction at a specific energy, it creates a striking peak in the density of states (see Fig. 4.4). As a result, the resonant state can be easily identified among the eigenvectors of the density matrix computed using Eq. 1.3.23, since it will be associated with the largest eigenvalue near the resonance energy. When discussing resonant wavefunctions, it will be assumed that we are using a density matrix near the resonance energy and examining the eigenvector associated with the largest eigenvalue (and measurement probability) at that energy. This makes it possible to distinguish the resonant wavefunction from other modes which are propagating through the system but are unaffected by the resonance.

We compute the wavefunction of the resonant state corresponding to the first transmission dip in Fig. 4.4.1. Fig. 4.4.2 shows the full Husimi map for this wavefunction, using coherent states with uncertainties of $\Delta k/k = 100\%$ (a) and 20% (b). The individual projections correspond strongly to the cosine-wave projections in Fig. 4.2.1. Spatial variations in the Husimi map decrease as the size of the coherent state increases, as in Fig. 4.3.7.

The full Husimi map is visually identical between the quasi-bound state and the resonant state, which is expected since the resonant state is a hybrid of the quasi-bound state and only slightly perturbed by the propagating mode. However, the flux of the quasi-bound state is zero, but exhibits characteristic vortices in the resonant state. Moreover, as the energy is increased across resonance, the wavefunction doesn't substantially change in appearance, while the flux patterns alter dramatically. At first these behaviors appear to contradict the Husimi map, but we can show that the flux patterns correlate with subtle changes in the Husimi maps which we can retrieve by adding all their vectors.

We can begin to understand these subtle changes by examining the fundamental

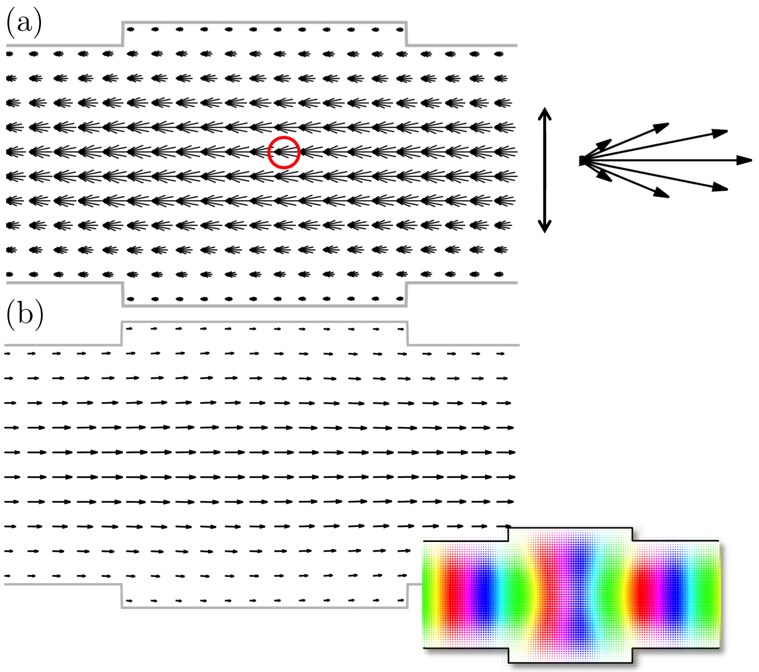

Figure 4.4.3: The full Husimi map for fundamental mode wavefunction (see inset) from the waveguide in Fig. 4.4.1 is plotted in (a), at an energy well above resonance ($E = 0.02745$ in arbitrary units scaled to Fig. 4.4.1). The uncertainty for this map is $\Delta k/k = 20\%$. At right, a magnified view of the projection circled in red. In (b), the Husimi flux is shown. This is the mode which hybridizes with the resonance state to produce Figs. 4.4.2 and 4.4.4.

mode. The full Husimi map far away from resonance, shown in Fig. 4.4.3 for a moderate coherent state, corresponds to the complex plane wave in Fig. 4.2.1. In the Husimi flux, the left-to-right flow appears unchanged within the central region of the system. The flux operator for this mode, not shown, is similar. In contrast, the vector-sum and the flux of the bound state is always zero. So what happens when it interacts with the fundamental mode to produce the resonant state?

In Fig. 4.4.4 we address this question by showing the traditional flux, wavefunction, and the Husimi flux above (a), at (b), and below (c) resonance. The flux operator is integrated over a Gaussian kernel corresponding to a coherent state spread

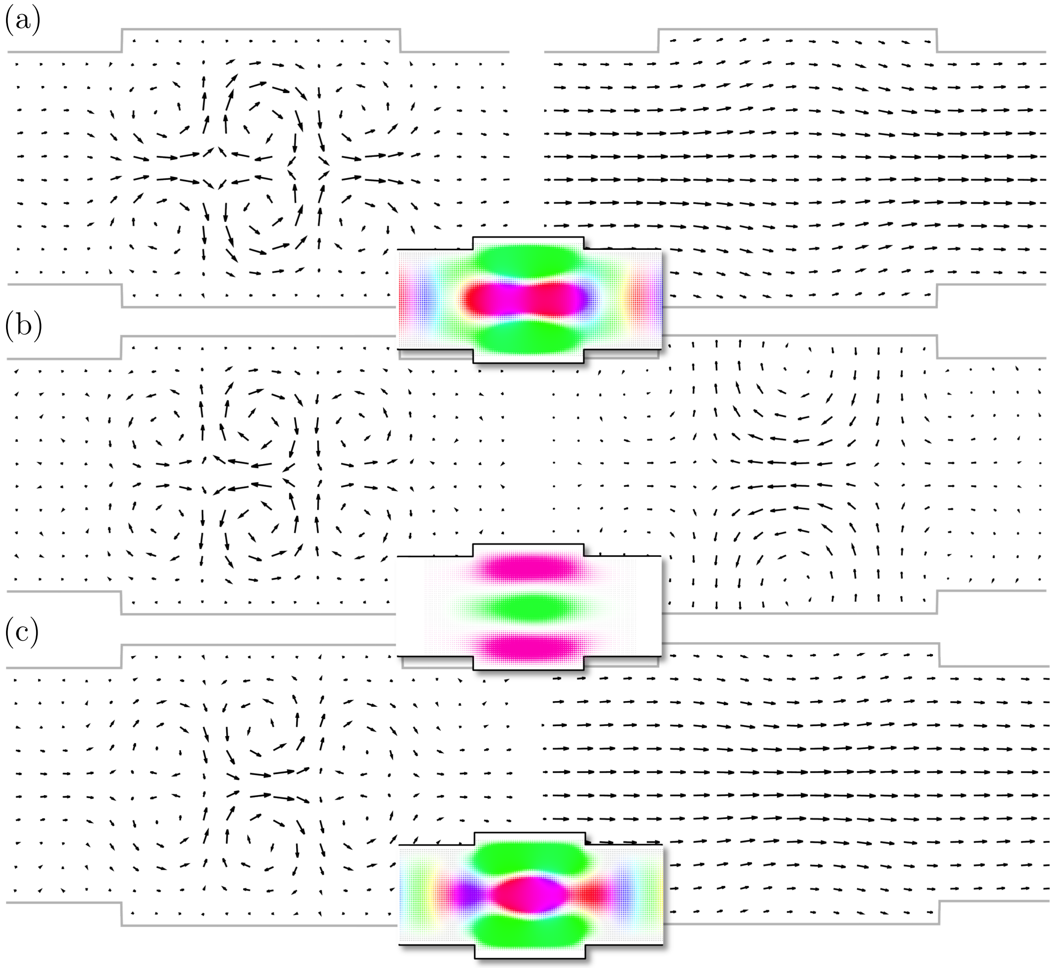

Figure 4.4.4: The traditional flux (left column) and the Husimi flux (right column) are shown for the resonance state in Fig. 4.4.1 slightly above resonance (a, $E = E_{\text{res.}} + 0.00005$), at resonance (b, $E = E_{\text{res.}}$) and slightly below resonance (c, $E = E_{\text{res.}} - 0.00005$). The coherent state for the Husimi map corresponds to $\Delta k/k = 0.2$. The transmission function at each energy corresponds to $T = 1$(a), 0(b), and 1(c). Even though the full Husimi maps at each energy are indistinguishable from Fig. 4.4.2, their vector additions (Husimi flux) vary substantially. Energies are in arbitrary units, scaled to Fig. 4.4.1.

of $\Delta k/k = 100\%$, and is visually identical to the Husimi flux with the same coherent state spread.

In the flux operator, we see the characteristic vortex patterns which flip above and below resonance, as expected when the bound state shifts through a phase of π over resonance. Moreover, while it is clear that the presence of the fundamental mode is stronger away from resonance, the wavefunction representation at all three energies is quite similar to the bound state. Similarly, probability flux is strongly localized in the center of the system, and it is unclear how the vortices correlate with the fact that transmission goes to zero on resonance.

In the Husimi flux, however, the correlation is obvious. At all three energies, vortices cancel out and leave behind the drift velocity of the mode. Above and below resonance, the Husimi flux is quite similar to the fundamental mode in Fig. 4.4.3, and the left-to-right flow extends through the semi-infinite leads, although there are slight changes in the central region. *At resonance,* however, the vortices no longer interfere to produce flow from left-to-right, but instead to produce flow from *right-to-left.* This drift velocity interferes with the transmitting mode to produce *zero* flow in leads, and therefore, zero transmission.

In other words, the classical dynamics of the resonance indicate a *subtle* shift in the overall contribution of classical trajectories which give rise to the resonance. The vortex pattern in the flux operator shows the small residual summation of these trajectories, but in fact the trajectories are dominated by the vertical bouncing motion from Fig. 4.4.2, as indicated by the wavefunction. Because these trajectories so strongly cancel each other out, the residual becomes exquisitely sensitive to the contribution from the fundamental mode.

Using the flux operator alone, the residual dominates, and using the wavefunction alone, the bouncing mode dominates. By examining at an intermediate scale using the Husimi map, however, we can complete the semiclassical correspondence and examine the drift velocity at resonance for this system.

4.4.2 Transport Through Other Geometries and the Nature of Flux Vortices

Because the σ parameter defines the spatial spread of the coherent states used to generate a Husimi map, we can use it to probe flux maps at arbitrary scales. In Fig. 4.4.5a, we show the probability flux for a scattering wavefunction in a large square block geometry that is associated with a mode of full transmission. This geometry is changed from the previous subsection so that: 1) Its dimensions are much larger than the characteristic wavelength at the energies we examine, 2) the leads are shifted vertically from the center towards the bottom-left and upper-right, and 3) the center is obstructed to constrain transport through the central region. As a result, classical paths related to transport in this system must reflect off the boundaries many times to propagate from the left to the right lead.

Transmission for a given mode in this system averages around one-half throughout the spectrum we examine. This is a result of the fact that all classical paths in this system must exit either through the incoming lead or the outgoing lead – whether it does or not is sensitive to the initial conditions, as indicated by the raplidly fluctuation transmission function for each mode.

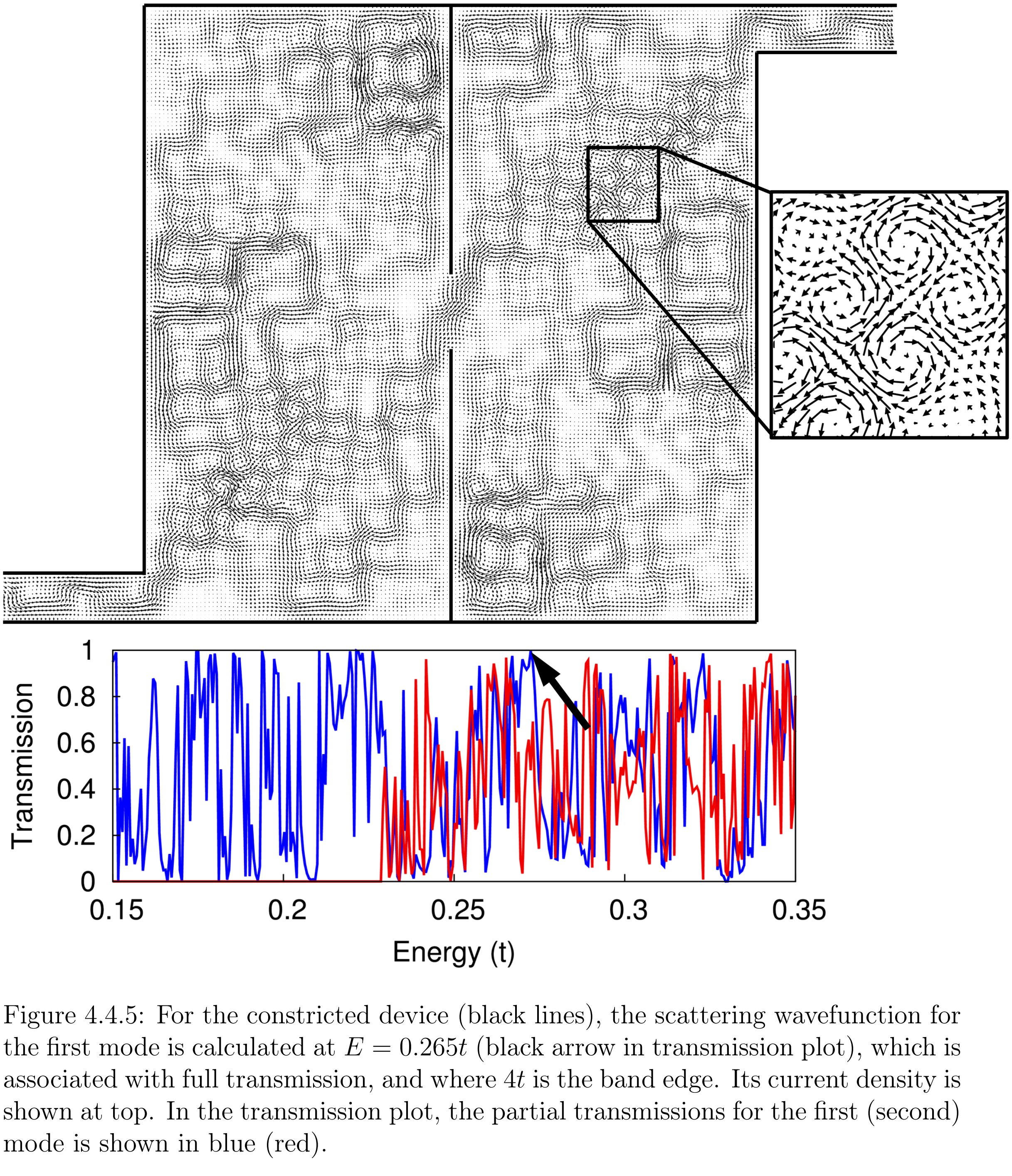

Figure 4.4.5: For the constricted device (black lines), the scattering wavefunction for the first mode is calculated at $E = 0.265t$ (black arrow in transmission plot), which is associated with full transmission, and where $4t$ is the band edge. Its current density is shown at top. In the transmission plot, the partial transmissions for the first (second) mode is shown in blue (red).

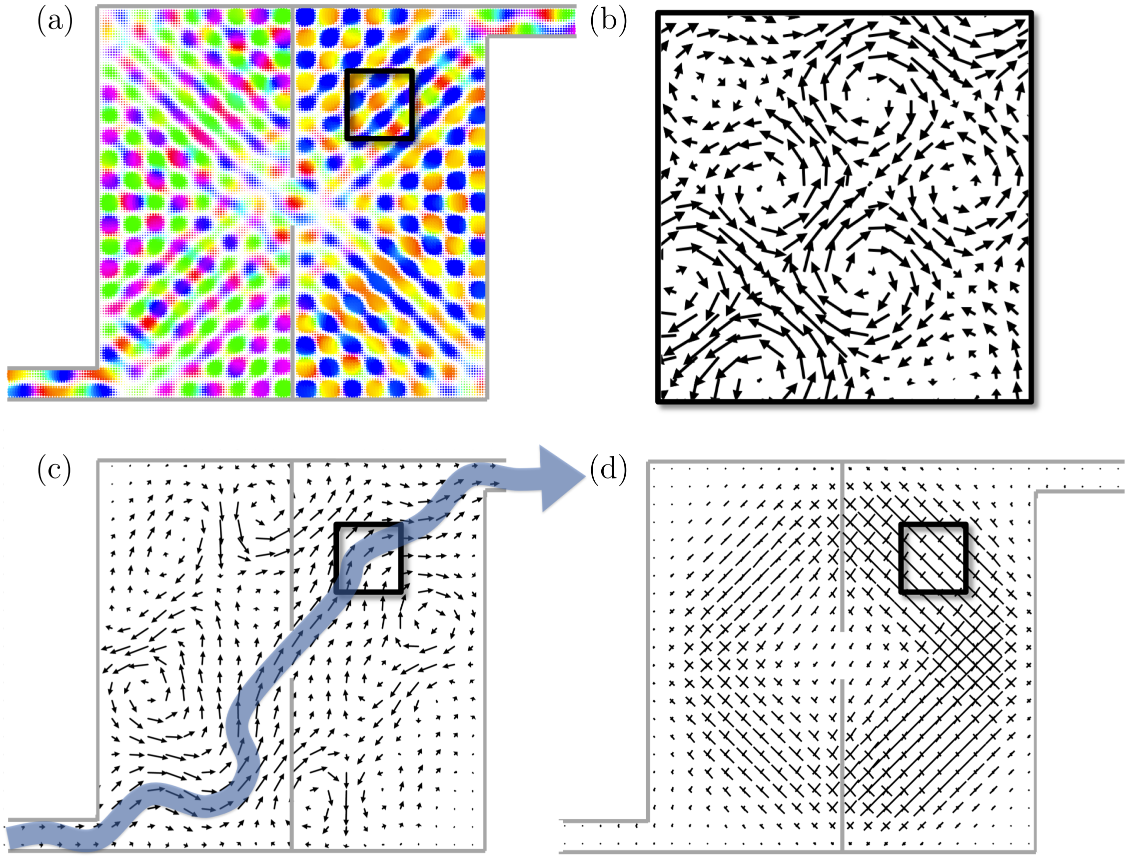

Figure 4.4.6: The scattering wavefunction associated with the current in Fig. 4.4.5 is shown with the wavefunction representation (a), the Husimi flux (c) and multi-modal analysis (d) for a coherent state spread of $\Delta k/k = 10\%$, indicated by the double arrows. The traditional flux from the part of the system indicated by the black squares is magnified (b).

In Fig. 4.4.5, we have selected a wavefunction that achieves full transmission, as indicated by the black arrow in the transmission function. Sure enough, the flux map shows a strong outgoing current to corroborate this fact. The bulk, however, is flush with many small vortices, which are magnified in the inset. The smallest vortices are of the same size but can combine to form larger vortices of various sizes; the salient feature is that many appear in pairs like those in the inset.

In Fig. 4.4.6, we show the wavefunction, a magnified view of the traditional flux,

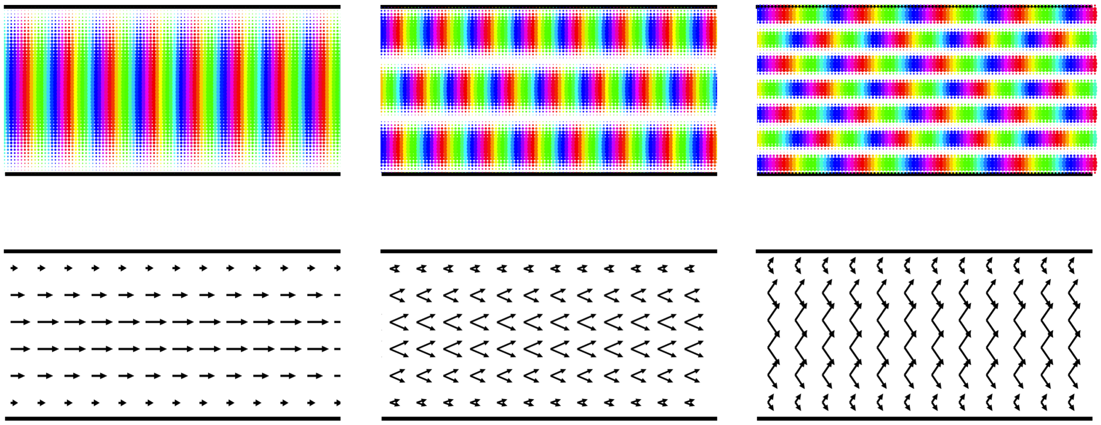

Figure 4.4.7: The scattering wavefunction associated with distinct modes of a wide unperturbed waveguide at $E = 0.26t$ are shown at top, with the multi-modal analysis at bottom. Each mode is associated with a pair of trajectory angles. As the number of horizontal nodal lines increases, and as energy increases, these angles become increasingly vertical. See also Fig. 3.4.2 for a quantitative analysis of the 45° cut.

the full Husimi flux, and the multi-modal analysis for this scattering state. In the wavefunction, nodal lines appear to fall along the 45° diagonals, which is corroborated by trajectories favoring those diagonals in the multi-modal analysis. This arises because all boundary conditions are vertical or horizontal walls; since each mode of the unperturbed waveguide leads is associated with a distinct pair of trajectory angles (See Fig. 4.4.7), the vertical and horizontal walls therefore reflect all trajectories back onto the same pair rotated at 45 degrees. At the energy we have selected, the pair of trajectory angles for the incoming mode are at perfect 45° diagonals, so that their rotations from reflecting off the walls also point along the diagonals, giving rise to strong standing waves.

In Fig. 4.4.6b, it is clear that transport occurs primarily through a narrow channel we call the conductance pathway with the majority of arrows pointing from the lower-left to the upper-right corners. By comparison, the full traditional flux map

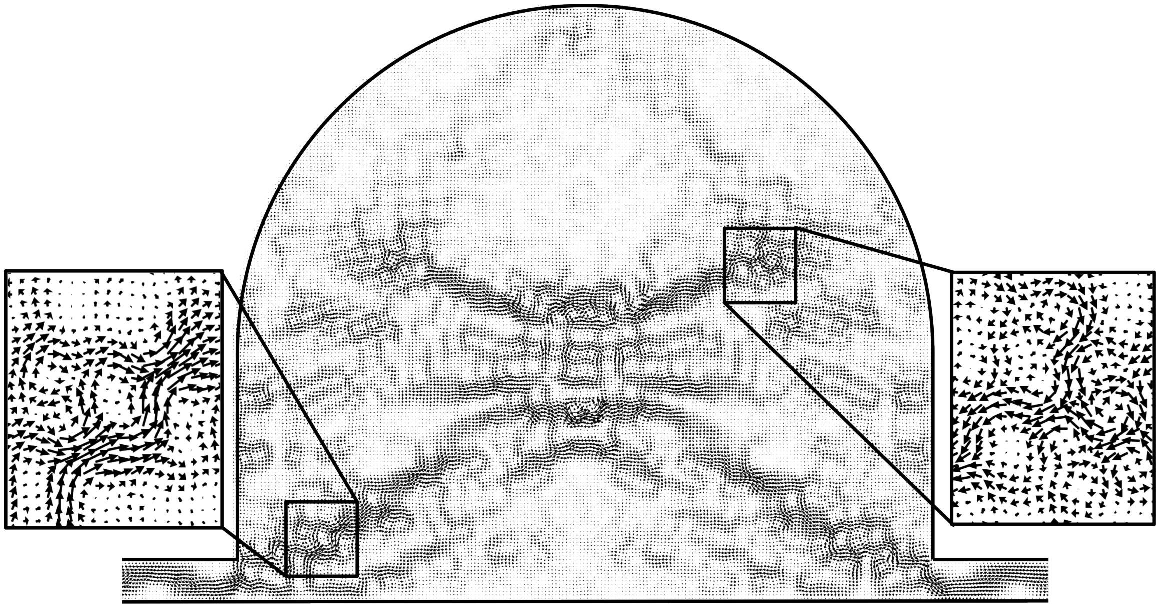

Figure 4.4.8: For the half-stadium (black lines), a full-transmission scattering wavefunction is calculated at $E = 0.495t$. Its current density is shown.

in Fig. 4.4.5 is rife with vortices throughout the entire system, dramatically limiting our ability to identify overall flow. The conductance pathway does not have to be classical, since it is an aggregate phenomenon from many other classical trajectories; as a result, it is able to curve in the bulk without external forces. As the pathway moves against many other perpendicular classical paths indicated in the multi-modal analysis, pairs of vortices form on either side[1]. These vortex pairs also arise in subthreshold resonance as the left-to-right conductance pathway passes through perpendicular trajectories in the perturbed waveguide (See Fig. 4.4.4 and the surrounding discussion).

In Figs. 4.4.5 and 4.4.6, there are a huge number of trajectories within the bulk that equally contribute to the wavefunction, resulting in many flux vortices. By

---

[1] Although the vortex pairs in Figs. 4.4.4 and 4.4.6 resemble von Karman vortex shedding[79], their origin is quite different.

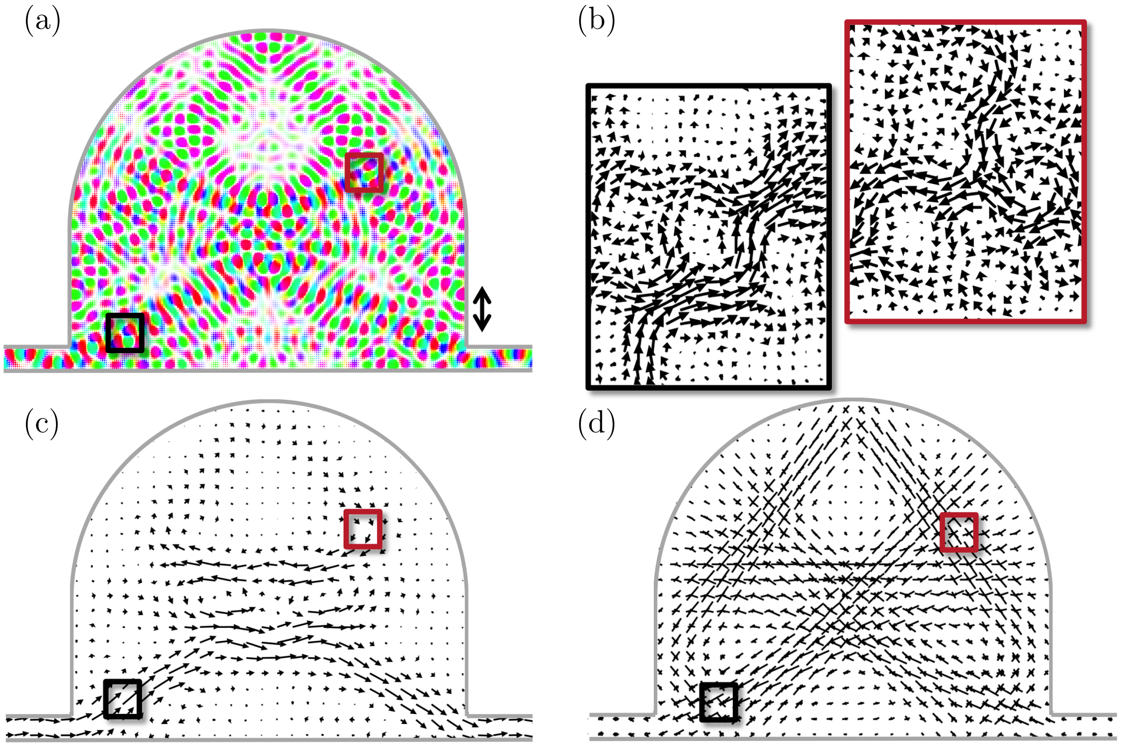

Figure 4.4.9: The scattering wavefunction associated with the current in Fig. 4.4.8 is shown with the wavefunction representation (a), the Husimi flux (c) and multi-modal analysis (d) for a coherent state spread of $\Delta k/k = 10\%$, indicated by the double arrows. The traditional flux from the part of the system indicated by the black and red squares is magnified (b).

applying the Husimi map with a large coherent state spread, we can pierce through local fluctuations to reveal the conductance pathway and appreciate the origin of flux vortices. What does the Husimi map tell us about flux in the other limit, where only a few classical trajectories dominate the wavefunction?

We address this question in Figs. 4.4.8, which shows the probability current for a full-transmission scattering state for a large half-stadium with two leads attached at its sides. Because scar orbits must self-loop but be otherwise unstable[76], scar states can only participate in transport when the leads attach at points that are slightly displaced from one of the orbit's reflection points. Otherwise, the classical orbit leaks out the system too quickly. The wavefunction in Fig. 4.4.9 shows strong scarring, and the multi-modal analysis corroborates the scarring with an identifiable classical orbit which just misses the leads.

Like the square device with obstructions in Fig. 4.4.6, flux also occurs most strongly along a narrow conductance pathway which, in this case, flows along the bottom of the device while deviating into the bulk at its middle. In addition, flux vortices occur throughout the system, making interpretation difficult without applying our methods. Unlike the square device, however, these vortices no longer form identifiable pairs. In the stadium state, classical paths do not intersect at 90° angles, but take on a variety of other oblique angles. As a result, the vortices take on forms that are consistent with the multi-modal Husimi map at each intersection. For instance, in the black inset, there is strong flow from bottom-left to upper-right, with other near-vertical flows forming vortices, and in the red inset, there are three primary flows propagating at 60° to each other, forming the triangular arrangement of vortices shown.

Chapter 5

The Husimi Map in Lattices

The previous chapter introduced a new interpretation of the flux operator

$$\hat{j}(\mathbf{r}) = \frac{1}{2m} \left(|\mathbf{r}\rangle \langle \mathbf{r}| \hat{p} + \hat{p} |\mathbf{r}\rangle \langle \mathbf{r}| \right) \tag{5.0.1}$$

as the limit of measurement by infinitesimally small coherent states, resulting in a new analytical tool called the Husimi map. This chapter extends the formalism of the Husimi map from the continuous free-particle system to crystals and lattices.

Even though the extended wavefunction of an electron in a crystal is also continuous, the potential imposed by the nuclei can sometimes be modeled by replacing the continuum with localized wavefunctions centered at individual tight-binding lattice sites. These individual wavefunctions combine to form a model of the entire wavefunction, which now defines their envelope function, dramatically simplifying calculations and making it possible to model much larger systems. In this model, Eq. 5.0.1 describes not the probability flow at an infinitesimal point, but the flow of probability in and out of the localized wavefunction at a single site.

Lattice systems can behave very differently from continuous systems. For instance, the orientation of the group velocity vector, which dictates classical dynamics, can strongly diverge from the phase velocity, which was the initial foundation of the Husimi projection. At higher energies, the group-velocity space can be strongly restricted, permitting classical trajectories only along certain directions. When these trajectories hit a boundary, internal Bragg diffraction can produce additional nonclassical ray reflections.

Here we explore two-dimensional square and honeycomb lattices; extension to three-dimensional systems is straightforward. Honeycombs induce an additional phenomenon: the presence of multiple bands and valleys, by which different classes of pseudo-particles can propagate and interfere. While the flux operator is unable to reflect any of these behaviors, with proper modifications, the Husimi projection can handle them with ease. Moreover, Husimi maps can help produce novel insights into the interactions among multiple particle types in the system.

5.1 Effects of Group Velocity on the Husimi Projection

In Chapter 4, each Husimi function is weighted by the wavevector of the coherent state to produce a visual guide to the classical dynamics of the system. Summing all the vectors equates to the flux operator (Eq. 4.2.3) when the coherent states are sufficiently small. This equivalence holds in lattices, however, the direction and magnitude of the group velocity $\boldsymbol{\nabla}_{\mathbf{k}} E\left(\mathbf{k}\right)$ can strongly diverge from the wavevector.

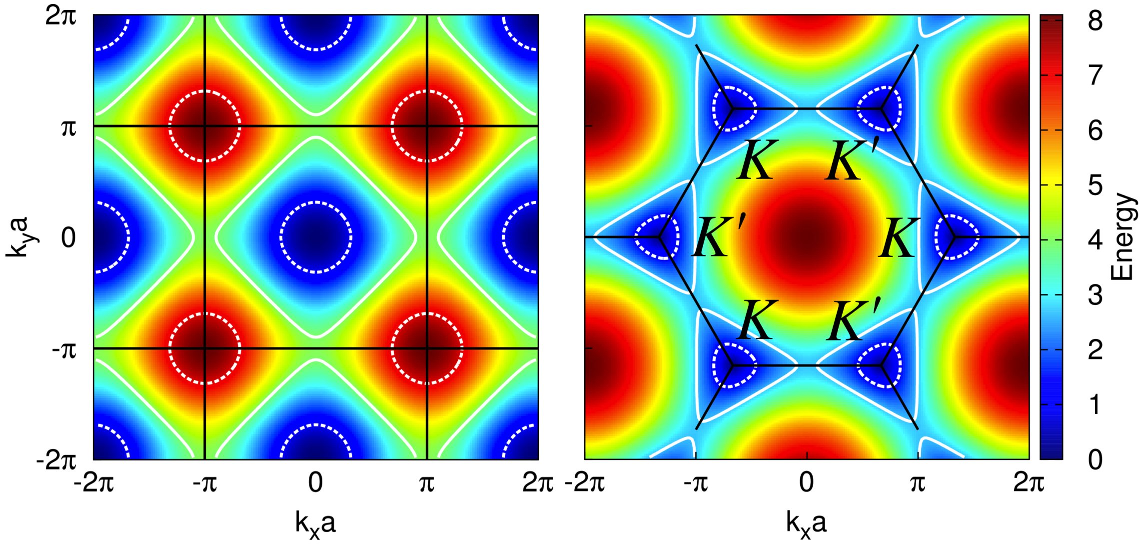

Figure 5.1.1: The two-dimensional dispersion relation for the square (left) and honeycomb lattices (right) demonstrate strong group-velocity warping at high energies. In dashed, the dispersion relations for $E = 0.9t$, $7.1t$ (left) and $0.5t$ (right) are nearly circular, while their neighbors near the band edge $E = 3.9t$ (left) and $0.98t$ (right) show strong warping.

Since a coherent state, which is now defined as an envelope function over localized wavefunctions, follows the group-velocity vector instead of its wavevector, it is necessary to weight the Husimi function by group-velocity vectors to indicate the classical dynamics. This suggests another shortcoming of the flux operator (Eq. 5.0.1) for understanding the dynamics of these systems.

At low energies, the square lattice closely approximates a free-particle continuous system so that this modification is minimal. At higher energies, however, the mapping from phase to group velocity can be strongly constricted. For example, at energies near the band edge of $E = 4t$, there are only four directions available to the group velocity in the square lattice, as shown in the contour line of Fig. 5.1.1.

To help the reader visualize this effect, we show group-velocity Husimi projec-

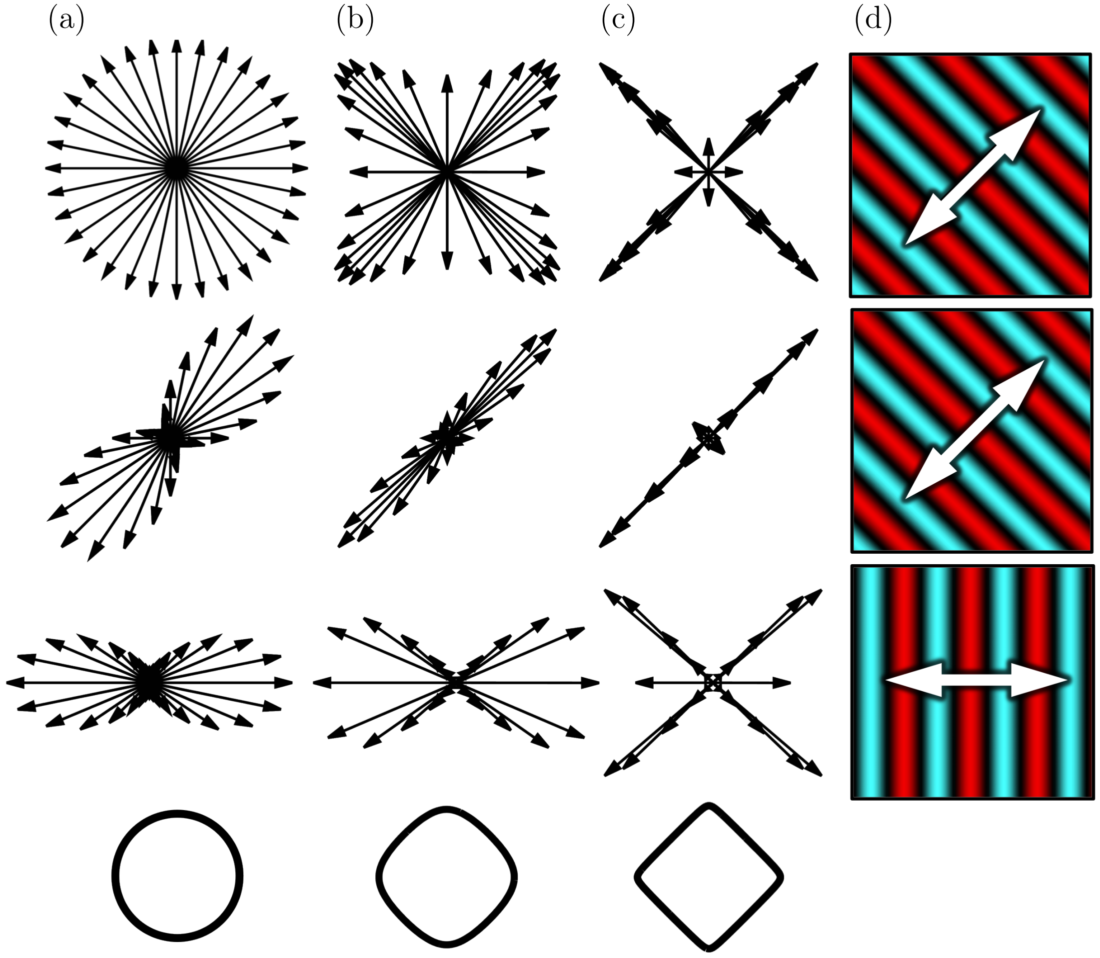

Figure 5.1.2: The group-velocity Husimi projection is strongly affected by warping at high energies (Fig. 5.1.1). Husimi projections are shown for the square lattice for the group-velocity representation at $E = 0.9t$(a), $3.0t$(b), and $3.9t$(c) with relative uncertainties of $\Delta k/k = 2$ (top) and 50% (middle and bottom). The dispersion relation contour at each energy is shown at the far bottom. The generating wavefunction ψ for each row is shown in (d). In the top and middle row the test wavefunction is a cosine wave pointing along the 45° diagonal, and in the bottom along the 0° horizontal.

tions at three representative energies in Fig. 5.1.2 for the square lattice. Thirty-two equally-spaced angles along a circle are chosen to represent the local momentum space. Wavevectors are chosen with these angles to satisfy the dispersion relation for a given energy.

At high enough energy, most classical trajectories in a system must follow the preferred directions determined by the dispersion relation, but the manner in which they do this may differ. This can be seen in Fig. 5.1.2 which examines two cosine-wave states with different wavevectors. As the energy of the system increases from left-to-right, group-velocity warping draws Husimi vectors, and the classical paths, towards four preferred directions. When the generating wavevector points along one of these directions, group-velocity warping merely sharpens the profile. When the generating wavevector points *in between* the preferred directions, as in the bottom row of Fig. 5.1.2, the classical trajectories are more strongly dependent upon the system energy.

If a system is modeled by the continuous Schrodinger equation, but sampled on a lattice, the effects of group-velocity warping can be avoided by increasing the number of sample points in the system (See Fig. 5.3.1). But for real-world lattice systems, the lattice spacing is not an adjustable parameter, and group velocity must be given careful attention.

Any quantity that measures the statistics of classical dynamics from the Husimi projection should be first computed using phase velocity, and then modified to reflect the group velocity. In the Multi-Modal Algorithm, for example, templates and matchings still occur using the phase-velocity Husimi projection to produce wavevectors describing individual trajectories. These results are then mapped onto group velocity by taking the local derivative of the dispersion relation.

5.2 Extensions Due to Band Structure

The number of bands for a lattice system is proportional to the number of tight-binding orbitals in the unit cell[9]. The square lattice we use has only one unique tight-binding orbital and only one band, but due to the warping in the band structure, there is an additional set of quasiparticles above $E = 4t$ (see the contour lines in Fig. 1.1.2 near the corners of the Brillouin zone). Because both sets of quasiparticles are separated by energy, they cannot scatter into each other.

In the honeycomb lattice, however, there are *two* unique orbitals in the lattice structure, yielding two bands that are isolated by energy: they only touch at the Dirac points at $E = 0t$. But more interestingly, the band structure warps each band to produce two inequivalent valleys, K and K', which are visible in Fig. 5.1.1. Unlike the square lattice, these two valleys co-exist in the energy range $-t < E < t$.

It might be tempting to obtain a representation of either valley in a graphene wavefunction by subtracting off a plane wave whose wavevector corresponds to the origin of either K or K' valley, leaving behind the residual $\mathbf{q} = \mathbf{k} - \mathbf{K}^{(\prime)}$. However, the simultaneous presence of quasiparticles in both valleys invalidates this idea.

On the other hand, since wavevectors for each valley are sufficiently separated in k-space, the Husimi projection can distinguish each valley unambiguously for most momentum uncertainties.[1] Because the two valleys in graphene are part of the same

---

[1] More complicated lattices can have additional bands, and any automated method for calculating

band, they are able to scatter into each other without large potentials[9]. When this occurs, the Husimi map exhibits quasiparticles in one valley funneling into a drain, and quasiparticles in the other valley emitting from a source at the same point, leaving behind a signature wherever there is inter-valley scattering.

For the square lattice, time-reversal symmetry is expressed in the Husimi projection by the fact that each Husimi vector is accompanied by another of equal magnitude but opposite direction. This causes the flux operator and Eq. 4.2.3 to return null results. The same is true for the honeycomb lattice, except that the range of wavevectors available at low energies point towards the K and K' valleys.

When Husimi vectors are weighted by the group-velocity and not phase-velocity, a different behavior emerges. In the honeycomb lattice, group-velocity doesn't correlate at low energies with $\mathbf{k}$ but $\mathbf{k} - \mathbf{K}^{(\prime)}$; examining the Husimi projection for each valley individually, it is no longer true that each Husimi vector is accompanied by its opposite. Rather, each valley is the time-reversal symmetric version of the other, allowing Husimi vectors in each valley to sum to non-trivial results.

We can represent this feature by using the Husimi flux, defined in Eq. 4.2.3 as

$$\mathrm{Hu}\left(\mathbf{r}_0, \sigma; \psi(\mathbf{r})\right) = \int \mathbf{k}_0 \left|\langle \psi | \, \mathbf{r}_0, \mathbf{k}_0, \sigma \rangle\right|^2 d^d k_0, \tag{5.2.1}$$

but instead weight the integrand by the group velocity $\boldsymbol{\nabla}_{\mathbf{k}} E\left(\mathbf{k}'\right)$ to obtain the group-velocity Husimi flux $\mathrm{Hu_g}\left(\mathbf{r}_0, \sigma; \psi(\mathbf{r})\right)$ equal to

$$\mathrm{Hu_g}\left(\mathbf{r}_0, \sigma; \psi(\mathbf{r})\right) = \int \boldsymbol{\nabla}_{\mathbf{k}} E\left(\mathbf{k}_0\right) \left|\langle \psi | \, \mathbf{r}_0, \mathbf{k}_0, \sigma \rangle\right|^2 d^d k_0, \tag{5.2.2}$$

which is used throughout this chapter.

Husimi maps for these systems have to take their mutual distance in k-space into account.

When a quasiparticle in one valley scatters into another in the honeycomb lattice, this appears as non-trivial divergence in the Husimi flux $\mathrm{Hu_g}\left(\mathbf{r}_0, \sigma; \psi(\mathbf{r})\right)$. We quantify this divergence according to

$$Q_{\text{div.}}\left(\mathbf{r};\Psi\right) = \int D\left(\mathbf{r},\mathbf{k}';\Psi\right)\boldsymbol{\nabla}_{\mathbf{k}}E\left(\mathbf{k}'\right)d^dk', \tag{5.2.3}$$

where $D\left(\mathbf{r},\mathbf{k};\Psi\right)$ is defined as the divergence of the Husimi map for one wavevector $\mathbf{k}$,

$$D\left(\mathbf{r},\mathbf{k};\Psi\right) = \int\sum_{i=1}^{d}\frac{\mathrm{Hu}\left(\mathbf{k},\mathbf{r}';\Psi\right)-\mathrm{Hu}\left(\mathbf{k},\mathbf{r};\Psi\right)}{\left(\mathbf{r}'-\mathbf{r}\right)\cdot\hat{e}_i}\exp\left[\frac{\left(\mathbf{r}'-\mathbf{r}\right)^2}{2\sigma^2}\right]d^dr'. \tag{5.2.4}$$

On the other hand, when a quasiparticle in one valley reflects off a boundary but does *not* scatter into the other valley, the divergence is zero, but the reflection can still be measured in the angular deflection of the Husimi map,

$$Q_{\text{ang.}}\left(\mathbf{r};\Psi\right) = \int\left|D_{\text{abs.}}(\mathbf{r},\mathbf{k}';\Psi)\boldsymbol{\nabla}_{\mathbf{k}}E\left(\mathbf{k}'\right)\right|d^dk', \tag{5.2.5}$$

where $D_{\text{abs.}}\left(\mathbf{r},\mathbf{k};\Psi\right)$ is defined as the *absolute* divergence of the Husimi function for one particular trajectory angle with a wavevector $\mathbf{k}$,

$$D_{\text{abs.}}\left(\mathbf{r},\mathbf{k};\Psi\right) = \int\sum_{i=1}^{d}\left|\frac{\mathrm{Hu}\left(\mathbf{k},\mathbf{r}';\Psi\right)-\mathrm{Hu}\left(\mathbf{k},\mathbf{r};\Psi\right)}{\left(\mathbf{r}'-\mathbf{r}\right)\cdot\hat{e}_i}\right|\exp\left[\frac{\left(\mathbf{r}'-\mathbf{r}\right)^2}{2\sigma^2}\right]d^dr'. \tag{5.2.6}$$

As a result, boundary points with large angular deflection are either inter-valley or intra-valley scatterers depending on the magnitude of divergence at each point.

5.3 Stadium Billiard Eigenstates

In Fig. 5.3.1, we begin by examining eigenstates from two closed stadium billiard systems with identical geometric parameters. Both systems are created using the

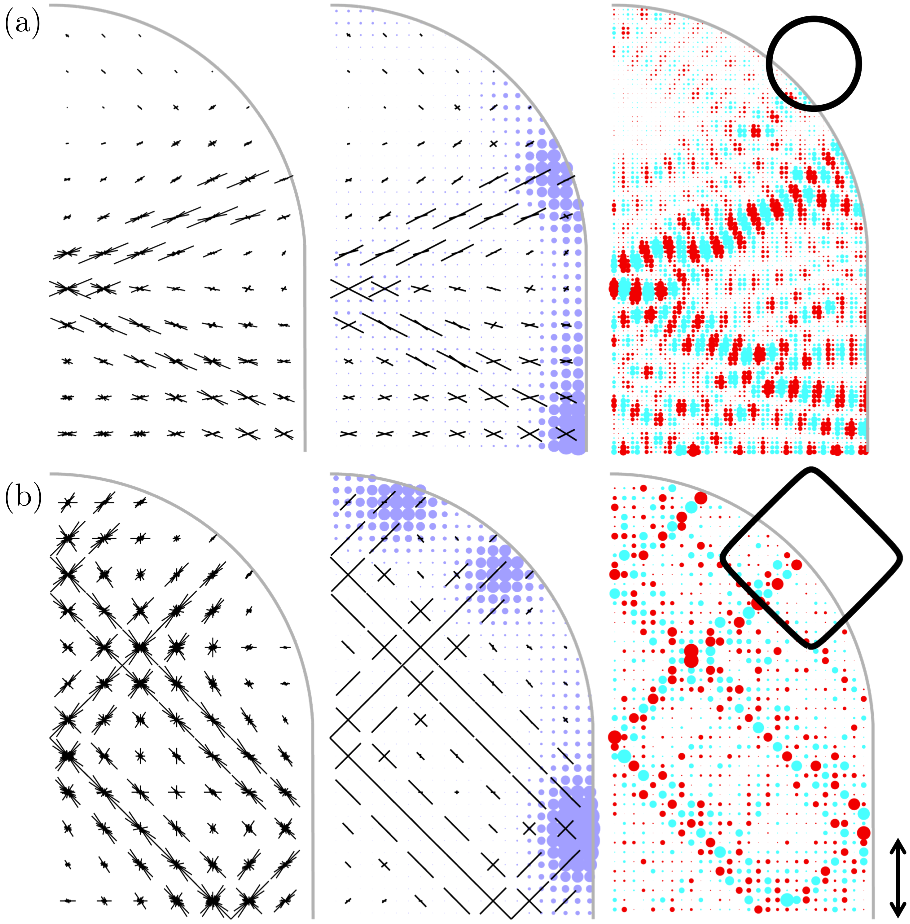

Figure 5.3.1: The full phase-velocity Husimi map (left), multi-modal analysis (middle) and wavefunction (right) are shown for two stadium eigenstates at energies $E_1 = 1.496t$ (a) and $E_2 = 3.982t$ (b) (the dispersion relation contour at each energy is shown in the insets). The uncertainty for each projection is set to $\Delta k/k = 10\%$, and the spread of the coherent state is indicated by double arrows on the right. Angular deflection (Eq. 5.2.6) is indicated in blue. Each eigenstate has similar characteristic wavelengths, but the lower eigenstate is sampled with half the linear resolution, causing its energy to go up and the group velocity to become more restrictive.

square-lattice tight-binding model, but the lattice constant in Fig. 5.3.1b is twice as large, so the system possesses far fewer sampling points.

As a result, keeping the characteristic wavelength constant raises the energy in the under-sampled system, causing strong effects from group-velocity warping. In Fig. 5.3.1b, an eigenstate of the under-sampled system is shown with energy $E_1 = 3.892t$, near the band edge. The energy for the finely-sampled system was chosen to reflect the same characteristic wavelength, which depends upon which direction in k-space is considered. Along the k_x-axis, the energy is bounded below by

$$\frac{E_2}{t_2} = -2\left(\cos\left(\frac{a_2}{a_1}\cos^{-1}\left[1 - \frac{E_1}{2t_1}\right]\right) - 1\right), \tag{5.3.1}$$

and at 45-degrees from the k_x-axis, it is bounded from above by

$$\frac{E_2}{t_2} = -4\left(\cos\left(\frac{a_2}{a_1}\cos^{-1}\left[1 - \frac{E_1}{4t_1}\right]\right) - 1\right). \tag{5.3.2}$$

By setting $\frac{a_2}{a_1} = \frac{1}{2}$ and $t_1 = t_2 = t$ an eigenstate was chosen with an energy near the average of the bounds at $E = 1.496t$.

It is immediately apparent that the Husimi map for the higher energy eigenstate in Fig. 5.3.1b emphasizes a few classical trajectories that are strongly restricted to the angles $\pm\frac{\pi}{4}$ and $\pi \pm \frac{\pi}{4}$, while the Husimi map for the lower-energy eigenstate (Fig. 5.3.1a) has a much broader selection of trajectory angles. Moreover, the trajectories in the higher-energy system are much clearer, which is consistent with having a restricted group-velocity space.

The Husimi map makes it possible to measure "angular deflection", which reflects how classical trajectories deviate from the straight line in response to the system. Angular deflection thus provides a map of where the boundaries or external potentials most strongly effect these dynamics, and can be interpreted as a force on the particle represented by the wavefunction.

Fig. 5.3.1 shows this quantity in blue, and it is concentrated on the boundary as expected. Because the resolution of angular deflection is limited by the spread of the coherent state used for Husimi sampling, the variance of the angular deflection along the boundary exhibits the same Gaussian distribution that is used for the test wavepacket. It is worth noting that without the proper modifications, angular deflection based on phase velocity shows non-trivial results in the bulk of the system even when there are no external fields.

This also suggests that modifications may be in order for other metrics for high-energy lattice systems. For instance, by coordinating the boundary divergence with each angle, one can automatically compute a state's Poincare map without requiring numerical ray-tracing algorithm to propagate in time. In Birkhoff coordinates[80, 81], the angle of impact is mapped against a coordinate along the boundary[65], and both fully quantum[66, 67] and classical[82] variations have become valuable tools in quantum chaos. By incorporating group-velocity considerations, these metrics may be improved.

Fig. 5.3.2a shows the Husimi map of the K' valley for a high-energy eigenstate in part (b) where the strong pull towards the three preferred group-velocities is evident. In parts (c) and (d), the multi-modal analysis for the K' and K valleys are shown. According to the time-reversal symmetric relation, the Husimi map for the K valley is the precise inverse of the K' valley. While the classical trajectories are evident in the wavefunction Fig. 5.3.2, the Husimi map identifies their orientation for each valley.

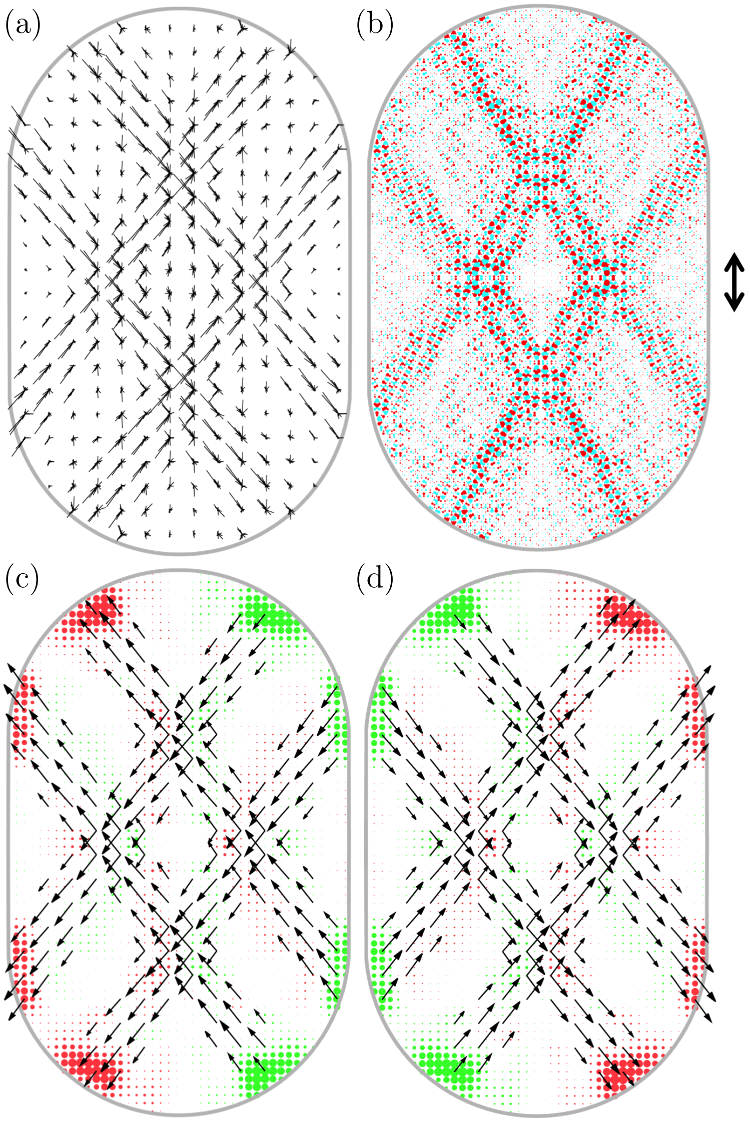

Figure 5.3.2: The full Husimi map around the K' valley(a), the wavefunction(b), the multi-modal analysis for the K' valley(c) and for the K valley(d) are shown for high-energy eigenstate of the honeycomb lattice at $E = 0.786t$. This system is a closed stadium billiard system with 20270 lattice points. The relative uncertainty in all calculations is $\Delta k/k = 20\%$ with the coherent state spread indicated by the double-arrows. Because of time-reversal symmetry, the Husimi maps in (c) and (d) are exact inverses of each other. Unlike the square lattice, the summing the Husimi vectors for each valley in a honeycomb lattice gives non-zero results for a closed system, giving rise to non-trivial divergences along the boundary where one valley scatters into the other (indicated in green for positive and red for negative).

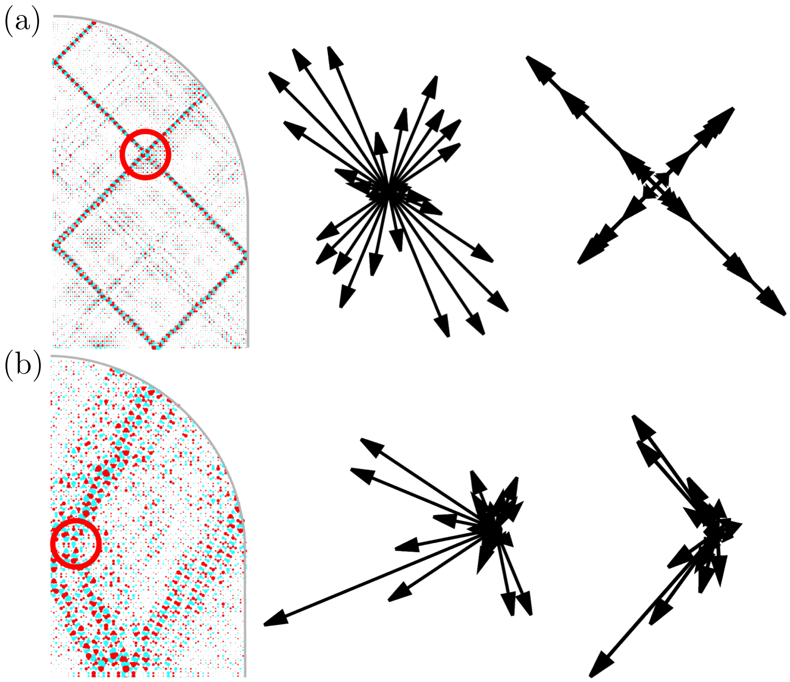

Figure 5.4.1: Two stadium eigenstates are shown for the square lattice (a) and the honeycomb lattice (b). The wavefunctions (left), phase-velocity Husimi (middle) and group-velocity Husimi (right) projections are shown for the points circled in red. Uncertainties for both projections are $\Delta k/k = 20\%$. Not only is there more spread to the phase-velocity projections, these projections also indicate markedly different trajectory paths than the group-velocity equivalents. Moreover, the group-velocity projections are more consistent with the paths indicated by the wavefunctions.

The total divergence appears in green and red in Figs. 5.3.2c and 5.3.2d corresponding to positive and negative values. These points are, in fact, sources and drains for each valley, and represent the inter-valley scattering points along the boundary. The results in Fig. 5.3.2 suggest that each classical trajectory in this wavefunction shares half of its existence in one valley, and half in the other.

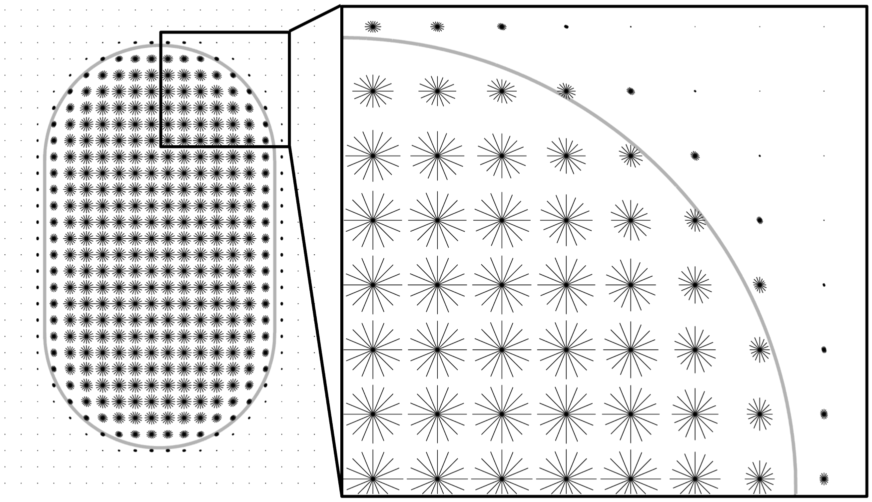

Figure 5.4.2: The extended Husimi maps for 16 angles are summed over hundreds of eigenstates near $E = 0.5t$ for the square lattice stadium billiard with a coherent wavepacket spread of $\Delta k/k = 10\%$. The magnified view shows that all points have equivalent Husimi projections, except along the boundary where directions parallel to the boundary are emphasized, consistent with Dirichlet boundary conditions.

5.4 Group Velocity Warping

Figs. 5.4.1 expands upon our findings in Figs. 5.3.1 and 5.3.2 by looking at the phase-velocity and group-velocity Husimi projections for eigenstates of the square and honeycomb lattices. As expected, the spread of each Husimi projection is dramatically reduced in the group-velocity representation, a consequence of group-velocity warping and consistent with Fig. 5.1.2. Moreover, a close examination reveals that phase-velocity Husimi vectors can point along surprisingly divergent angles from their trajectories, emphasizing the extent to which group-velocity warping establishes such states.

If it is possible to produce similar classical trajectories using a wider variety of phase-velocities for lattices at higher energies, then what is the distribution of either over all states of the system? We can provide an answer by summing the Husimi

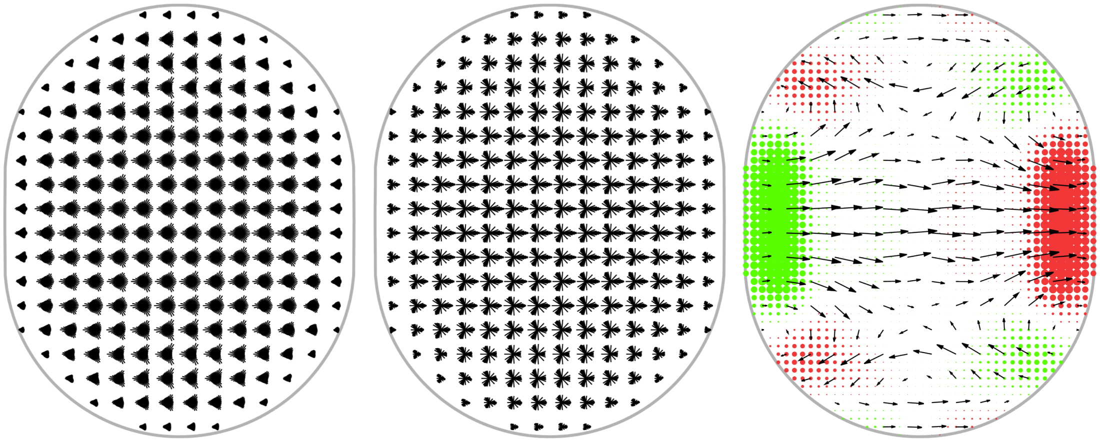

Figure 5.4.3: The Husimi map for 32 angles are summed over a hundred of eigenstates near $E = 0.72t$ for a small graphene billiard (the Huang system introduced in Subsection 5.6.1) with coherent state spread of $\Delta k/k = 30\%$. From left-to-right: the phase-space Husimi map, the group-velocity Husimi map, and the group-velocity Husimi flux, with divergence indicated in green (positive) and red (negative). Emphasized in the divergence are the two armchair boundaries on both sides which act as inter-valley scatterers, and smaller armchair edges at the corners of the system.

projections over a range of eigenstates. We find that with a sufficient range of eigenstates, neither phase-velocity nor group-velocity distributions vary across the bulk of the system, except along the boundaries. For the square-lattice billiards, directions parallel to boundaries are emphasized, which is consistent with Dirichlet boundary conditions (Fig. 5.4.2).

For the honeycomb lattice, inter-valley scattering points along the perimeter emphasize trajectories perpendicular to the boundary. For smaller honeycomb lattice billiards at higher energies, additional fluctuations emerge in the bulk in response to the locations of these inter-valley scattering points (see Fig. 5.4.3). These fluctuations emphasize trajectories that connect inter-valley scattering points, are strongly dependent upon the set of states chosen, and whether inter-valley scattering points can be connected by a path that falls along a preferred group-velocity direction. However,

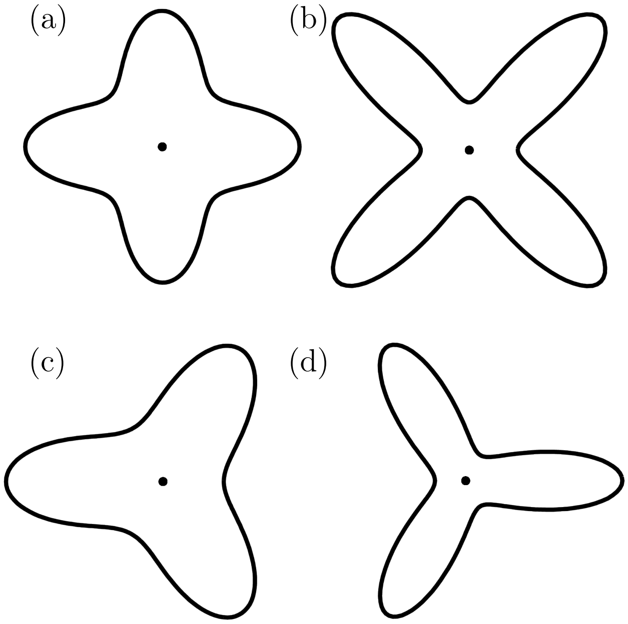

Figure 5.4.4: The distribution of Husimi vectors from the red circles in Fig. 5.4.1, summed over hundreds of eigenstates near $E = 3.5t$ for the square lattice and $E = 0.8t$ for the honeycomb lattice, with a coherent wavepacket spread of $\Delta k/k = 10\%$. Above, the phase-velocity in the square lattice (a), group-velocity in the square lattice (b), phase velocity for the K' valley in the honeycomb lattice (c), and group velocity for the K' valley in the honeycomb lattice (d). Husimi projections tend to emphasize phase velocities away from the preferred group-velocity directions (a,c), but not enough to overcome that preference in the group-velocity distribution.

these fluctuations are small enough that they do not substantially alter our results.

In Fig. 5.4.4, we show a representative distribution of the phase and group velocities for the systems from Fig. 5.4.1. These plots are produced by summing the Husimi vectors over many eigenstates of each system: For the square lattice, 600 states with energies $3.46t < E < 3.54t$ and for the honeycomb lattice, 300 states with energies $0.76t < E < 0.84t$. This is done for 256 wavevectors equally separated by angle, and then we apply a small Gaussian kernel of angle width $\pi/32$. Each Husimi vector is multiplied by the infinitesimal dk determined by the average distance to neighboring vectors in the sample, and each calculation takes place at the points circled in red in Fig. 5.4.1 with coherent spread of $\Delta k/k = 10\%$. The contour line in the dispersion relation is re-computed for each eigenstate to generate the coherent states for the Husimi projection. This is done to ensure that the steeper gradient of the dispersion relation near the preferred group velocities does not affect our results.

Fig. 5.4.4 shows that the distribution among phase velocities emphasizes directions *away* from the preferred directions in group velocity. For lattices at high energies, *neither* phase velocity *nor* group velocity are evenly distributed across all eigenstates.

5.5 The Nature of Scar-Like Patterns in High-Energy Eigenstates

The high-energy eigenstates from Fig. 5.4.1 exhibit an unusual behavior: the self-looping classical trajectories that are strongly emphasized in the wavefunctions do not exhibit specular reflection at the boundary. We clarify these reflections in the schematics in Fig. 5.5.1. Even though the absolute angles at each reflection point fall along the same diagonal, the *angles of incidence* vary substantially between the incoming and outgoing rays. In the honeycomb eigenstate (Fig. 5.5.1b), the reflection consists of scattering into the other valley and propagating in the exact opposite direction.

While the reflections of many trajectories in high-energy states violate specularity as a result of group-velocity warping, we have chosen the states in Figs. 5.4.1 and 5.5.1 specifically because these reflections behave in completely unexpected ways.

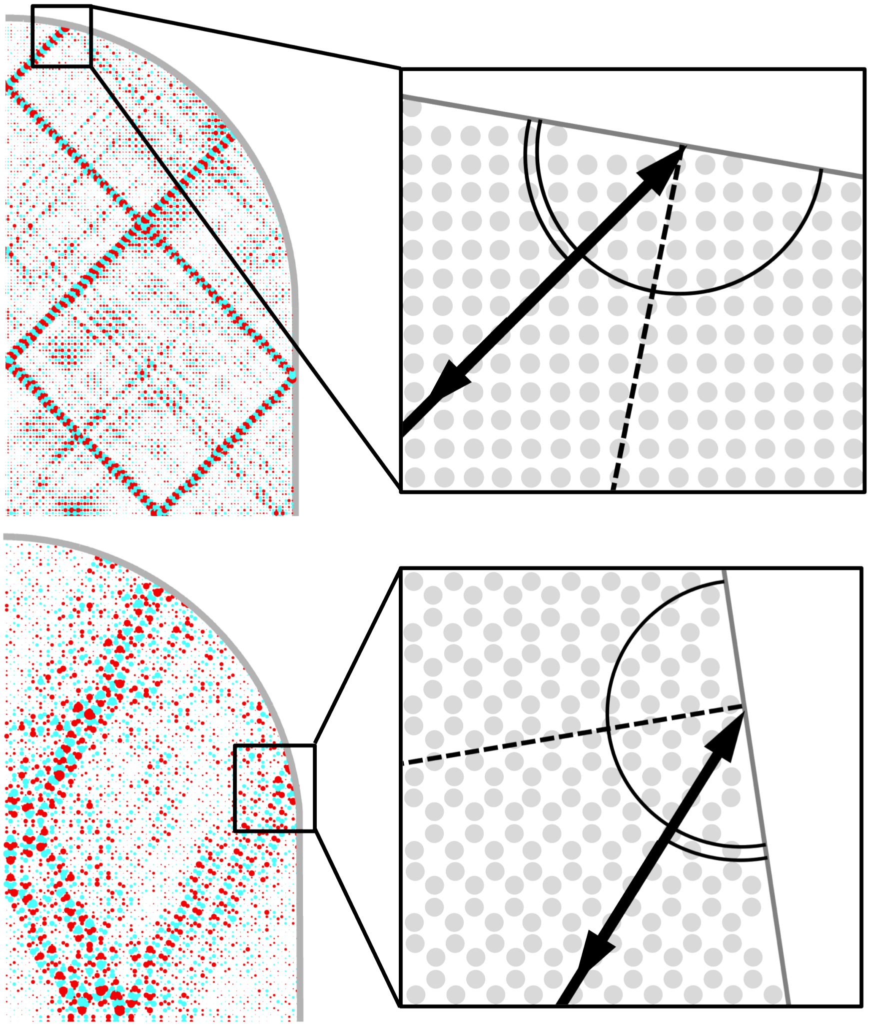

Figure 5.5.1: High-energy states in the square (a) and honeycomb (b) lattices can exhibit unusual behaviors, such as group-velocity warping and non-specular boundary reflections. The former can be seen in the wavefunction (left) by the restriction of trajectories to 45° diagonals for the square lattice (a) and the 60° diagonals for the honeycomb lattice (b). Non-specular reflections are magnified in the schematic (right). Even though the absolute incoming and outgoing angles for each point are the same angle, their angles of incidence (single and double arcs) are in fact strongly divergent.

Moreover, these surprising reflections occur only at certain points along the boundary where the lattice cut deviates from an axis of symmetry; specifically, they occur slightly off of clean cuts where jaggedness is most prominent. These reflections can be explained by internal Bragg diffraction, which we explore in depth in Section 3.5.

Combining group-velocity restriction and internal Bragg diffraction, we argue that the dense linear paths in the wavefunctions in Figs. 5.4.1 and 5.5.1 are indeed linked to classical rays which bounce back and forth approximately linearly; at one boundary the bounce is non-specular due to the cut of the edge and internal Bragg diffraction. For the honeycomb lattice, each bounce can be additionally associated with valley-switching. For both systems, these wavefunction enhancements are not strictly scars[76], which are generated by unstable classical periodic orbits in the analogous classical limit (group velocity) system. Instead, the wavefunction structures are more likely normal quantum confinement to stable zones in classical phase space.

At lower energies away from the band edge, but still high enough to experience group-velocity warping, it is also possible to invoke scar-like pattern using stable orbits. In Fig. 5.5.2, we show Husimi maps for two stadium billiard eigenstates in both the continuous regime (top) and the group-velocity warping regime (top). Both states show strongly linear classical paths for large enough coherent states, but at smaller coherent states, the Husimi projections for the lower-energy state wobble along the classical paths. This suggests different physical phenomena are contributing to the scar-like patterns in each state.

In fact, it is shocking that the scar pattern in the higher-energy state does not show similar interference patterns, since all classical paths that reflect off the circular

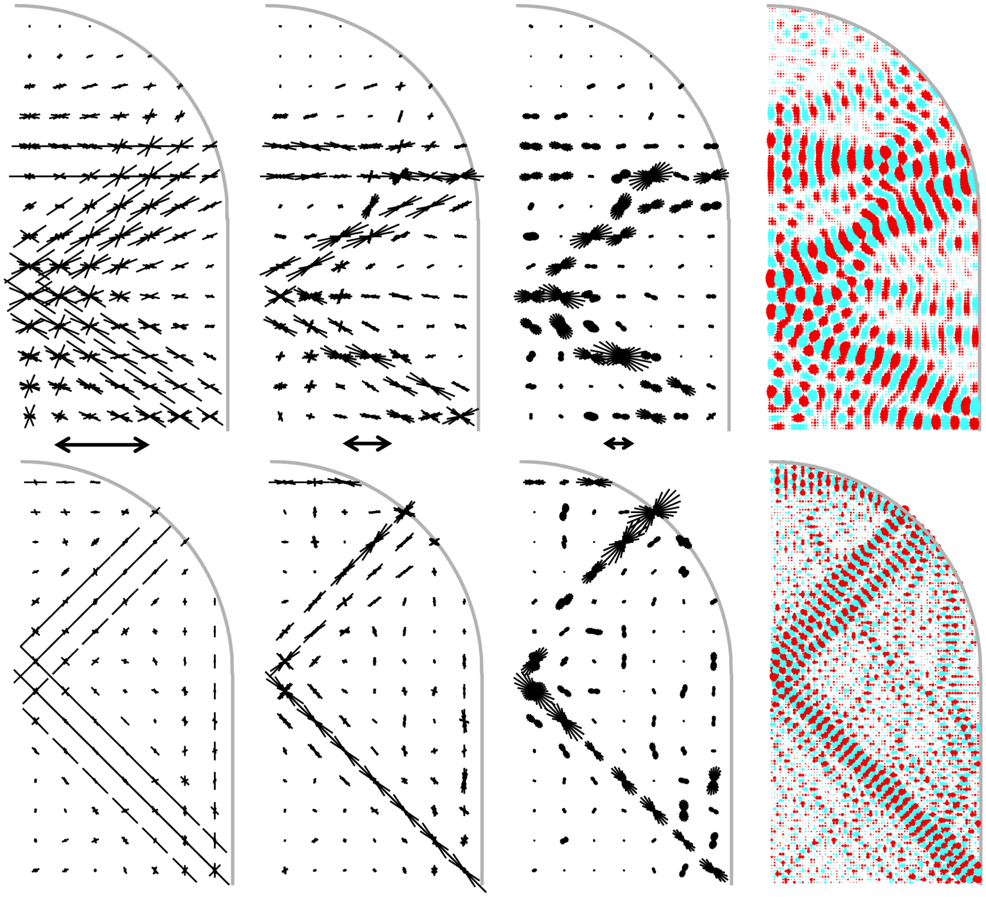

Figure 5.5.2: Phase-velocity Husimi maps for two stadium billiard eigenstates are shown. Each map uses a different spread of the measurement wavepacket. The spread is indicated by the double-arrows on the bottom, with relative uncertainties from left-to-right of $\Delta k/k = 5\%$, 20%, and 50%. At top, an eigenstate with energy $E = 1.1t$ (same as Figs. 3.0.1 and 4.3.7), and at bottom an eigenstate with energy $E = 3.01t$

boundaries are unstable in a stadium billiard. However, because of the gentle nudging of group-velocity warping at the energy $E = 3.01t$, previously unstable orbits can become stable, giving rise to the strongly self-reinforcing classical orbit seen. The nature of this phenomenon, and metrics of orbit stability as a function of energy in lattices deserve further study.

5.6 Additional Results in Graphene

Interest and experimental capabilities in graphene devices are growing[8, 83, 84, 85, 86, 87, 88, 89], but despite the success of the Dirac effective field theory for graphene[12], many of new technological proposals instead come from the more fundamental tight-binding approximation[90, 91, 92, 26]. This is because the atomistic model underlies the Dirac theory and easily breaks its assumptions, for instance by small scatterers[93, 94, 95, 96, 97], ripples[98], or edge types[99, 100, 101] – all of which promise technological applications. While such features can be modeled using scattering theory in the Dirac field, a robust approach which can handle them in an automatic and general fashion remains to be seen.

In this section, we use Husimi maps to deepen our understanding of relativistic scar states[41], edge states[12, 90, 92], and Fano resonances[43, 102, 103] in graphene. Fano resonances are an ideal case study for the Husimi map, not only because they are ubiquitous in theoretical predictions[104, 42] and experiments[105, 106, 107], but also because their behavior is well-understood on the mesoscale[27, 108, 109, 110, 111, 112, 103]. However, Fano resonances in *graphene* quantum dots are less well characterized[113, 114, 115, 116], and their understanding is important to building a comprehensive theory relating boundary conditions to bulk state behavior in graphene.

5.6.1 Boundary Conditions at High Energies

Fig. 5.6.1 shows Husimi maps for three eigenstates of a large closed-system stadium billiard with 20270 orbital sites at energies of $E = 0.974t(\text{a}), 0.964t(\text{b}),$ and $0.951t(\text{c})$. We have chosen these states because they exhibit very clear linear trajectories which exhibit characteristic trigonal warping (See Section 5.3).

Because just a few dominant classical paths are present in each wavefunction in Fig. 5.6.1 it is easy to observe the relationship between boundary types and scattering among the two Dirac valleys. We can measure inter-valley scattering by examining the divergence of the Husimi map as defined in Section 5.2. The divergence in the K' valley, seen in green and red (for positive and negative values, respectively) in Figs. 5.6.1 and 5.6.2, shows that inter-valley scattering points all lie along non-zig-zag boundaries. Plots for the K valley (not shown) are perfectly inverted, corroborating the time-reversal symmetry relationship between the two valleys.

In*tra*-valley scatterers, on the other hand, cause reflections that can be measured using angular deflection, but do *not* exhibit divergence. In Figs. 5.6.1 and 5.6.2, we plot the angular deflection in blue to compare to the divergence in green and red. Using this information, we can determine that for the wavefunction in Fig. 5.6.1a, all boundary scattering points are inter-valley scatterers, since all points of angular deflection exhibit divergence. The wavefunction in Fig. 5.6.1b, on the other hand, only exhibits divergence along the vertical sides of the stadium billiard: the horizontal top

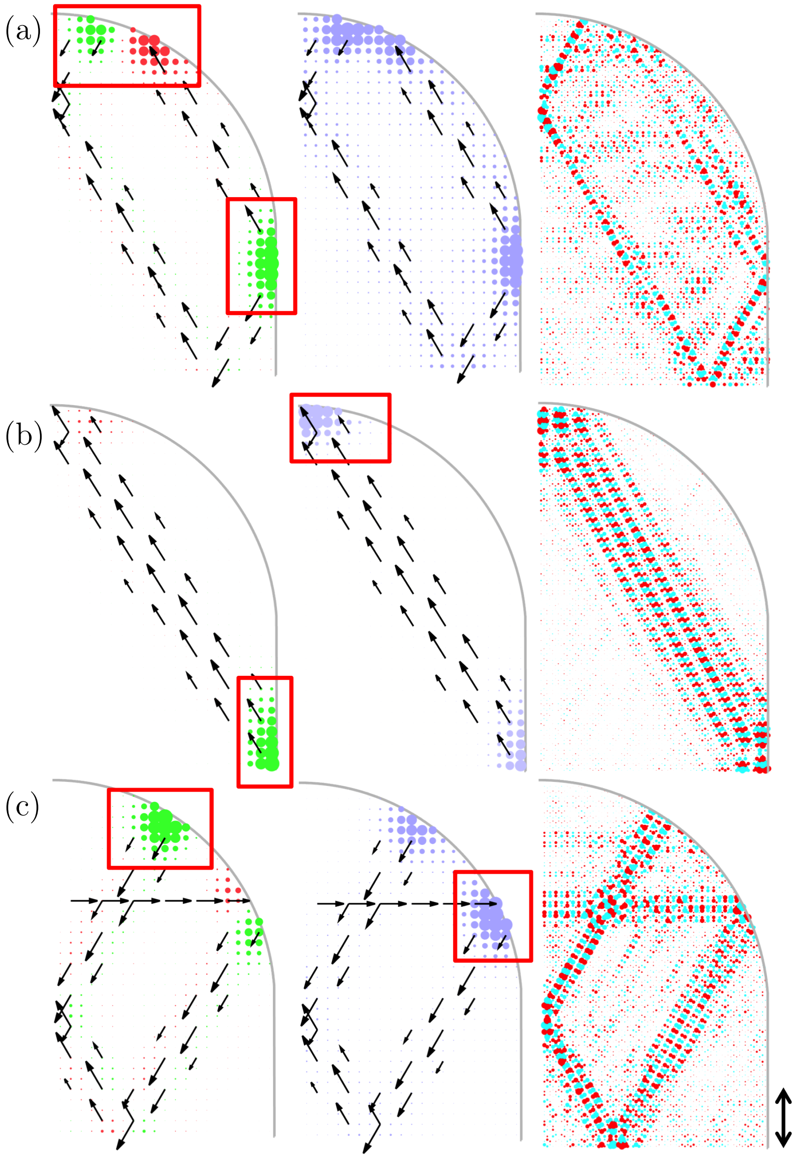

Figure 5.6.1: The Husimi map is plotted for three eigenstates of the closed graphene stadium billiard with 20270 orbital sites at energy $E = 0.974t(\text{a}), 0.964t(\text{b})$, and $0.951t(\text{c})$. All three calculations use coherent states with relative uncertainty $\Delta k/k = 30\%$, whose breadth is indicated by the double arrows on the right. Only the upper-right quarter of each stadia is shown. The multi-modal analysis for the K' valley (left) is shown alongside the wavefunction (right). The divergence of the Husimi map is shown in green (red) to indicate positive (negative) values. Angular deflection is shown in blue (Eq. 5.2.4). Red boxes indicate the magnified views in Fig. 5.6.2.

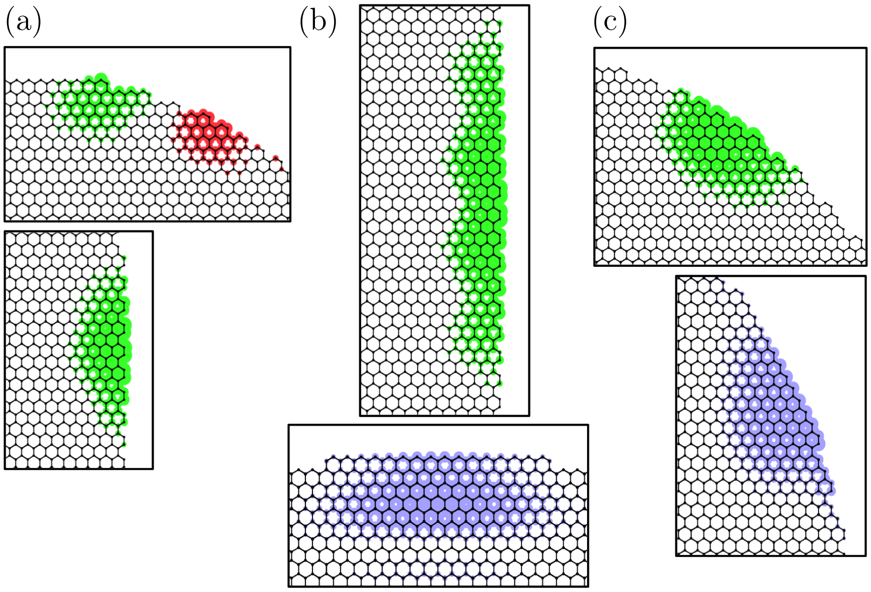

Figure 5.6.2: Magnified views of the divergence and angular deflection in Fig. 5.6.1 (red boxes) are shown and calculated at a higher resolution. The sources and drains in the K'-valley Husimi map are actually inter-valley scattering points, which occur along non zig-zag boundaries. In contrast, points of angular deflection that are *not* sources or drains correspond to *intra*-valley scatterers and occur along pure or nearly-pure zig-zag boundaries.

edge exhibits strong angular deflection but *no* divergence, and constitutes an *intra*-valley scatterer. Examining the magnified views in Figs. 5.6.2a and 5.6.2b, we see that inter-valley scatterers correspond to armchair edges, and the intra-valley scatterers belong to zig-zag edges, corroborating the findings at zero energy by Beenakker et al.[117]. Similar points of scattering can also be found in Figs. 5.6.1c and 5.6.2c.

Because of the time-reversal relationship between the two valleys, the severe restriction on group velocities, and the placement of zig-zag and armchair boundaries, no path at these energies exists *without* interacting with an inter-valley scatterer (data not shown). By comparison, it is not only possible but common to find states near the Dirac point that exhibit the opposite: all boundary conditions which are expressed belong to only *intra*-valley scatterers (See Subsection 5.6.2).

In comparison to Fig. 5.6.1, the eigenstate of the much smaller graphene stadium system in Figs. 5.6.3 does not appear to show isolated trajectories in its wavefunction representation. This isn't too surprising since this system can only accommodate five deBroglie wavelengths vertically, and three horizontally, severely restricting its ability to resolve such trajectories.

However, clear self-retracing trajectories are quite visible in the Husimi map in Figs. 5.6.3, with evident sources and drains inhabiting the boundary. This result suggests the underlying classical dynamics even for states which do not possess obvious interpretations from their wavefunction representation, and helps show why this state is able to form resonances. Because the paths indicated by the Husimi map are successful at marshaling the electron away from lateral boundaries, where the leads connect in the resonance state (see Sec. 5.6.3), this state is ideal for capturing and electron from a direct channel to form a long-lived resonance.

5.6.2 Interpreting States Near the Dirac Point

We now explore the properties of low-energy closed-system states in graphene, using the circular graphene flake and the distorted circular flake introduced by Wimmer et al.[53]. The placement of armchair and zig-zag boundaries is indicated in Fig. 5.6.4, which plays a significant role in the classical dynamics of these systems.

Because the effective wavevector $\mathbf{q} = \mathbf{k} - \mathbf{K}^{(\prime)}$ grows linearly with energy from zero at the Dirac point, the effective wavelength for graphene systems is much larger than equivalent continuous systems, making it difficult to conduct calculations with

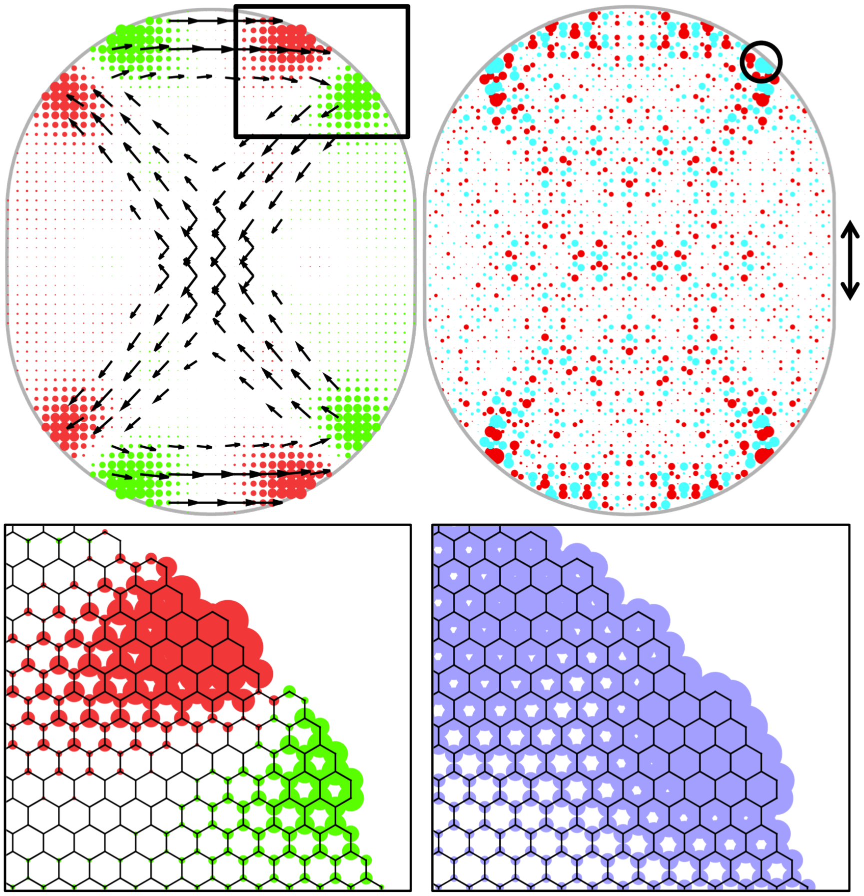

Figure 5.6.3: The closed-system eigenstate at $E = 0.72t$ responsible for the Fano resonance in Figs. 5.6.9 and 5.6.12 is shown. At top, the filtered Multi-Modal analysis is shown with relative momentum uncertainty $\Delta k/k = 30\%$ along with the wavefunction (right). The spread of the coherent state is indicated by the double arrows. At bottom, higher-resolution calculations of the divergence (green for positive, red for negative) and the angular deflection (blue) are shown against the graphene structure. The black circle indicates where the system boundary is perturbed in the original paper[41] as discussed in Section 5.6.3.

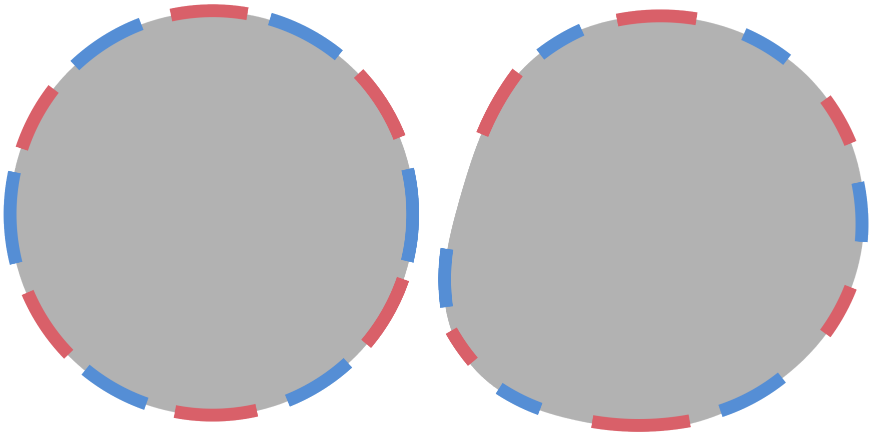

Figure 5.6.4: Schematic indicating the locations of armchair (blue) and zig-zag (red) edges in the circular system (left) and the Wimmer system (right).

sufficient structure in the wavefunction. Consequently, we examine states at higher energies from the Dirac point to bring calculations within a reasonable scope. (For instance, we have selected a system size under 100,000 orbital sites to facilitate replication of our results). Since trigonal warping becomes significant above $E = 0.4t$, we have selected the energy of $0.2t$ for all states in our analysis to maximize the number of wavelengths within a small graphene system while maintaining the same physics from energies closer to the Dirac point.

Fig. 5.6.5 shows four eigenstates of the circular graphene flake. Like the free-particle circular well, eigenstates of the graphene circular flake resemble eigenstates of the angular momentum operator (see Mason et al.[3] for direct comparisons and Husimi maps). For instance, the wavefunctions in Figs. 5.6.5a-b are radial-dominant, while the wavefunction in Fig. 5.6.5d is angular-dominant. These appearances are corroborated in the multi-modal analysis for the K' valley, which shows radially-oriented paths in Figs. 5.6.5a-b and circular paths skimming the boundary in Fig. 5.6.5d. Fig. 5.6.5c shows a state with a mixture of radial and angular components; in the

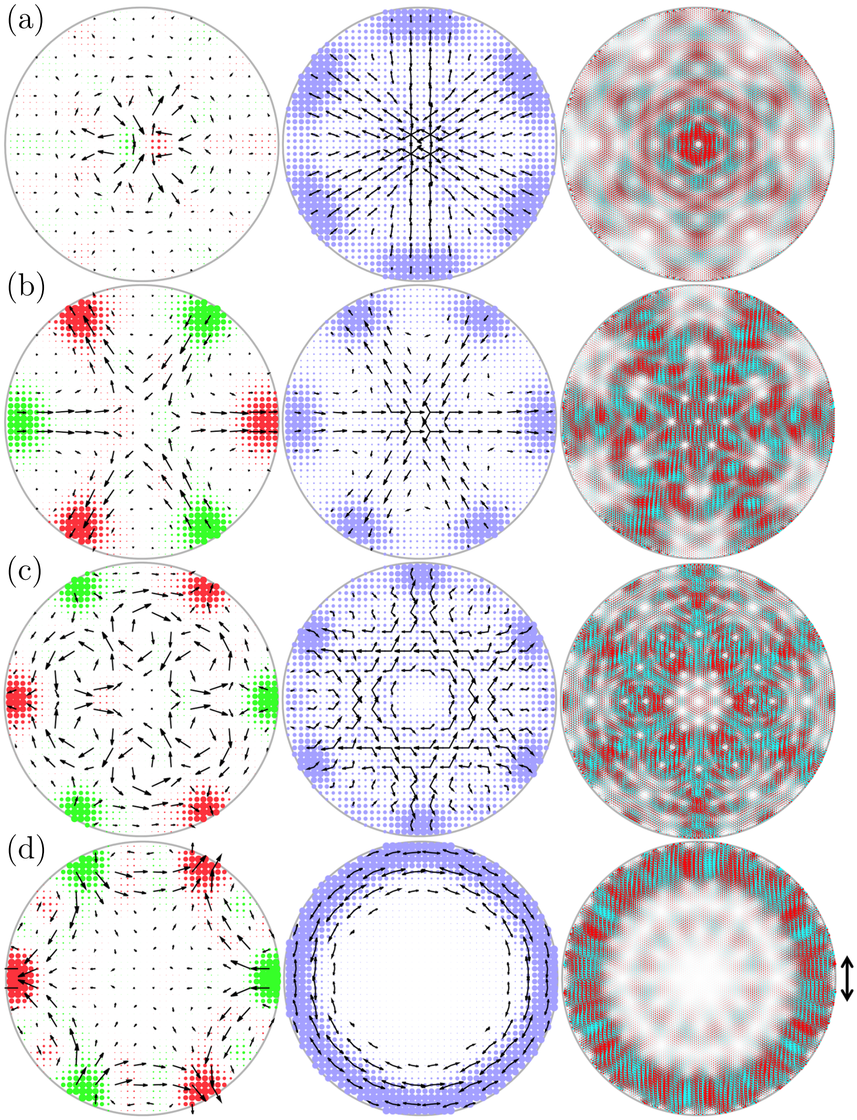

Figure 5.6.5: Low-energy graphene states require additional tools to fully grasp the classical dynamics. The Husimi map for the K'-valley is plotted for four eigenstates of a closed circular system with 71934 orbital sites at energies around $E = 0.2t$. All three calculations use coherent states with relative uncertainty $\Delta k/k = 20\%$, whose breadth is indicated by the double arrows on the right. From left-to-right: the Husimi flux, multi-modal analysis, and the wavefunction. The divergence of the Husimi flux is shown in green (red) to indicate positive (negative) values. In blue, the angular deflection.

multi-modal analysis, this appears as straight paths between boundary points highlighted by the angular deflection.

Unlike free-particle circular wells, however, the lattice sampling on the honeycomb lattice breaks circular symmetry and replaces it with six-fold symmetry. Because eigenstates of the system emphasize certain boundary conditions, the manner in which each state establishes itself strongly varies. For instance, the two radial-dominant states in Figs. 5.6.5a-b exhibit scattering exclusively within the same valley (a) or between valleys (b). Accordingly, the locations where the rays terminate on the boundary correlate with zig-zag and armchair boundaries respectively. The wider spread in angular deflection in Fig. 5.6.5a corroborates Beenakker et al.[117], showing that that intra-valley scattering occurs over a larger set of boundaries than inter-valley scattering.

Because each valley reflects back to itself in Fig. 5.6.5a, there is no net flow of either valley in the bulk of the system. As a result, the multi-modal analysis shows counter-propagating flows, and the Husimi flux (Eq. 5.2.2) is zero except at the center, where slight offsets in trajectories form characteristic vortices. In Fig. 5.6.5b, on the other hand, each ray in the wavefunction is associated with a distinct source and drain, which is evident in both the multi-modal analysis and the Husimi flux.

In Figs. 5.6.5c-d, the locations of sources and drains for the K' valley are reversed from Fig. 5.6.5b. However, the roles that inter-valley scattering play in these states is less clear; rather, inter- *and* intra-valley scattering dominate these wavefunctions. In Fig. 5.6.5c, this can been by the emphasis of angular deflection along the zig-zag boundaries, which do not show any divergence. In Fig. 5.6.5d, even though the wavefunction and the multi-modal analysis clearly emphasize a classical path that skims the boundary, the path actually flips between each valley each time it encounters an inter-valley scatterer. For both states, the various trajectories merge to form vortices in the Husimi flux, with sources and drains at armchair edges.

When the circular flake is distorted, as in the Wimmer system (Figs. 5.6.4 and 5.6.6), inter- and intra-valley scatterers are re-arranged and re-sized as a function of the local radius of curvature of the boundary.

Figs. 5.6.6a-b show two eigenstates of the Wimmer system. The boundary conditions for these states most closely resemble Fig. 5.6.3, since sources and drains appear next to each other. This is a signature of mixed scattering – both inter- and intra-valley scattering occur in various proportions at these points. For example, the multi-modal analysis in Fig. 5.6.6a shows a triangular path, but not all legs of the triangle are equally strong, corresponding to various degrees of absorption and reflection at each scattering point which can be seen in the divergence.

Edge-states are a set of zero-energy surface states that are strongly localized to zig-zag boundaries and potentially long-lived[12]. Because they can be used as modes of transport[90, 92], and also be strongly spin-polarized[91, 26], they have become a fascinating candidate for spin-tronic[12, 91, 90, 92, 26] devices.

Edge states exhibit a different dispersion relation than the two valleys in the bulk, so they cannot be “sensed” by the K' or K valley Husimi projections at their actual energies. Instead, the Husimi map can be generated using wavevectors appropriate to the edge states. On the right-hand side of Fig. 5.6.7, we show a Fourier transform of the edge state wavefunction in the upper-left, which shows that these edge states can

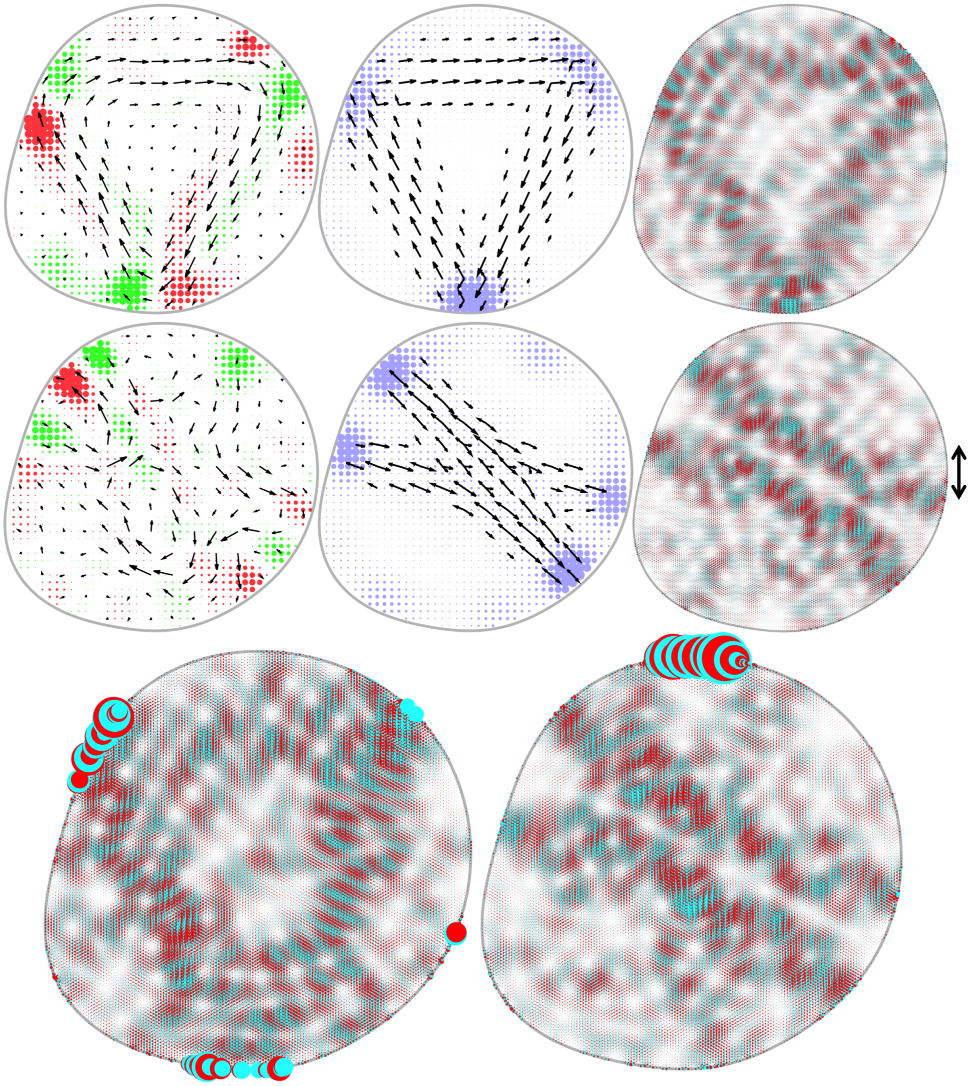

Figure 5.6.6: In parts (a) and (b), the same information is plotted as in Fig. 5.6.5, but for the Wimmer system (see Fig. 5.6.4), with 96425 orbital sites. These states also have energies near $E = 0.2t$ and are represented by coherent states of uncertainty $\Delta k/k = 20\%$. In parts (c) and (d), edge-state hybrid wavefunctions with bulk-state parallels to (a) and (b) are shown. These states are realized by setting the on-site energies of under-coordinated carbon atoms to $0.25t$.

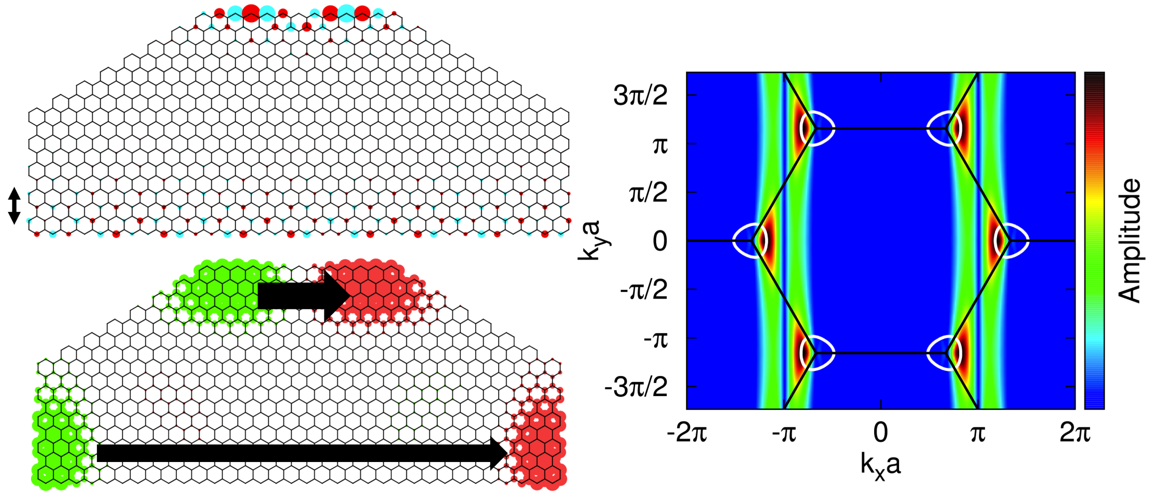

Figure 5.6.7: An extremely small "rooftop" graphene flake at energy $E = 0.0015735t$ showing two edge states at the top and bottom boundaries which tunnel into each other. At top left, the full wavefunction, at bottom-left, divergence is indicated in green and red, and a schematic of the Husimi projection is shown, using circles centered at each valley to determine the effective wavelength. At right, the Fourier transform of the state is shown, with the contour line used to generate the Husimi map at left.

be modeled using the valley formalism at the artificial energy $E = 0.45t$. We find that each edge state corresponds to a standing wave, which appears as if it is bouncing between the two valleys. The results do not substantially differ from other models – for instance, using wavevectors relative to the origin $\mathbf{k} = 0$ rather than $\mathbf{k} = \mathbf{K}'$.

As noted in Wimmer et al. [53], it is possible for edge states to tunnel into each other using bulk states as a medium. In Figs. 5.6.6c-d, edge-state hybridization with bulk states near $E = 0.2t$ has been induced by raising the onsite energies of under-coordinated atoms to $0.25t$. While onsite energies are likely non-trivial, and can arise from a number of sources[53], we have artificially inflated them to probe energies where a larger number of wavelengths can fit into the system. We have kept ratio of eigenenergies to passivation energy similar to theoretical predictions to provide a

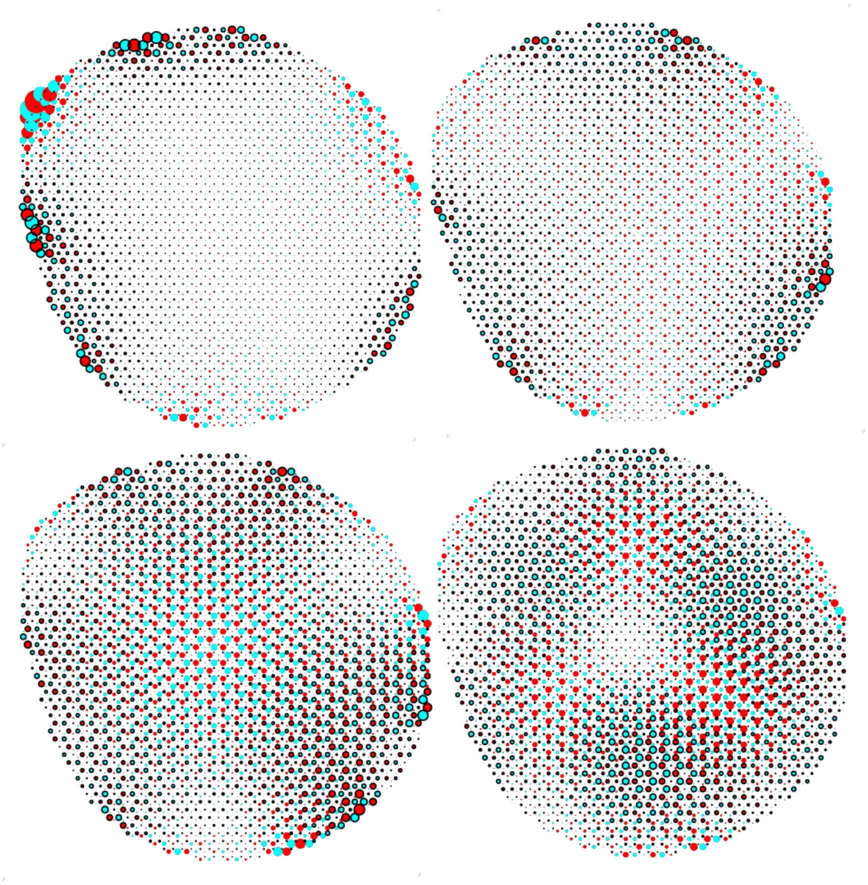

Figure 5.6.8: Additional edge-bulk hybrid states for a smaller Wimmer system with identical parameters. Here, the two sublattice are differentiated by adding black outlines to each B sublattice site. This helps show the connection between the bulk state and its orientation with different edges.

good analogy with larger systems at more experimentally realizable energies.

Using the normal valley formalism, we can examine edge states using Husimi maps of the bulk states with which they hybridize. However, effects of bulk-state selection among hybrid states appear to be subtle. For instance, it is possible for edge states to hybridize with bulk states whose classical dynamics interact strongly with boundaries where the edge state resides (See Fig. 5.6.6d) or not (Fig. 5.6.6c). Subtle changes to the bulk states *do* appear in extremely low-energy hybrid states: among features we have seen, orientations with different boundary types shift in response to the passivation parameter (See Fig. 5.6.8). Whether such effects can be observed for larger systems is a topic of further study.

5.6.3 Fano Resonance in Graphene

This section addresses Fano resonance[43] in graphene systems, a conductance phenomenon that occurs as a result of interference between a direct state (conductance channel) and a quasi-bound indirect state[103] similar to the eigenstates this thesis has examined. To study Fano resonance, we first compute a scattering wavefunction using the recursive numerical Green's function method described in Mason et al.[1]. This method produces a scattering density matrix ρ, which is diagonalized. Each eigenvector corresponds to a scattering wavefunction, which has an associated eigenvalue indicating its measurement probability (Fig. 5.6.9, middle).

This section focuses on the eigenstate from Fig. 5.6.3 of the closed billiard system that couples only weakly to leads which are attached at its sides (shown in the inset of Fig. 5.6.9). This makes it possible for a scattering electron to enter the system through a direct channel but then become trapped in a quasi-bound state related to the eigenstate, causing the density of states projected onto the eigenstate to strongly peak near its eigenenergy (Fig. 5.6.9, bottom). As the system energy sweeps across this energy, the phase of the eigenstate component shifts through π, causing it to interfere negatively and then positively with the direct channel, giving rise to the distinctive Fano curve (Fig. 5.6.9, top). As a result, the scattering wavefunction with the largest measurement probability is in fact a hybridized state between the

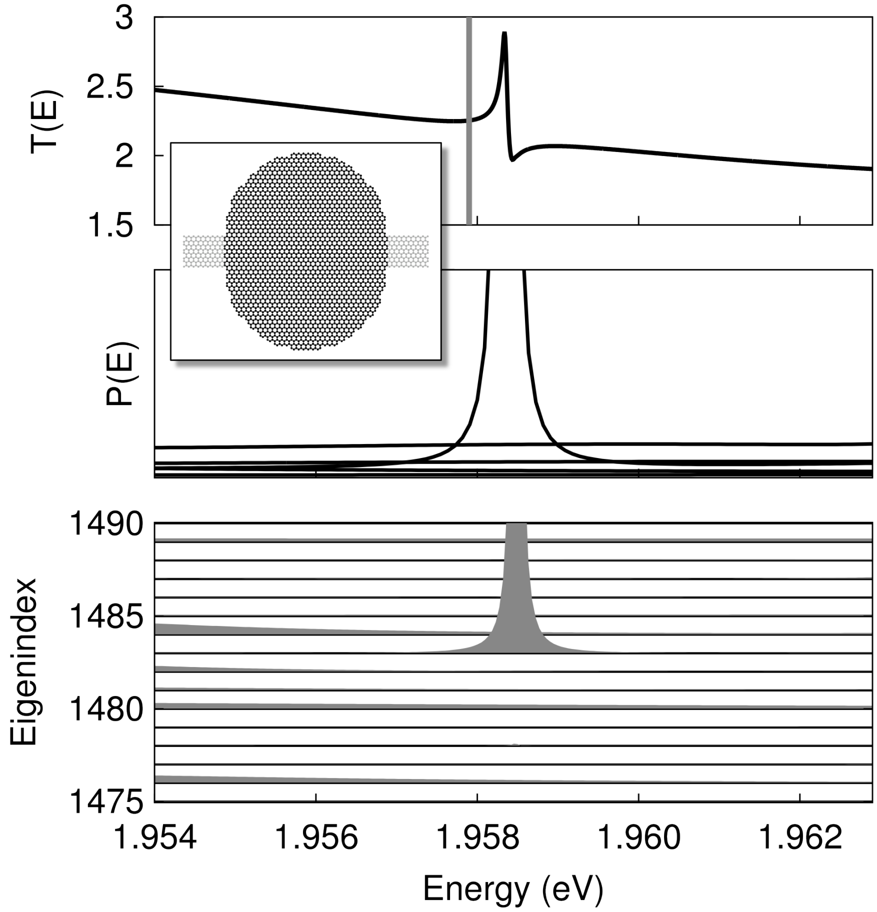

Figure 5.6.9: System properties of the scattering density matrix ρ around the Fano resonance centered at $E = 1.9582$eV for the open system shown in the inset. Top: The transmission profile across the two leads, with the closed-system eigenstate energy at $E = 1.9579$eV, corresponding to the eigenstate at index 1483 (below) shown in the vertical grey line. Middle: Diagonalizing the density matrix produces a handful of non-trivial scattering wavefunctions in its eigenvectors. The eigenvalues of these vectors, which correspond to their measurement probability, are graphed. The wavefunction associated with the closed-system eigenstate hybridizing with the direct channel peaks strongly around the Fano resonance. Bottom: The density matrix is projected onto the closed-system eigenstates, showing that eigenstate 1483 strongly peaks at the Fano resonance.

closed-system eigenstate and the direct channel, which we call resonant state. Its probability peaks around an energy near, but not exactly the same as, the eigenstate energy (Fig. 5.6.9, middle); the shift in energy arises as a perturbation from the leads.

Figs. 5.6.10 and 5.6.11 show the probability current below and above resonance under two representations: the bond current and the finite-difference flux. The bond current shows the probability flow between every pair of adjacent carbon atom sites, and it is defined as

$$j_{i\to j} = \frac{4e}{h}\mathrm{Im}\left[H_{ij}G^n_{ij}(E)\right], \tag{5.6.1}$$

where H_{ij} and $G^n_{ij}(E)$ are the off-diagonal components of the Hamiltonian and the electron correlation function between orbital sites i and j[27, 118]. The electron correlation function is proportional to the density matrix defined in Eq. 1.3.23, but in our calculations, we examine just one scattering state, so that $G^n_{ij} \propto \psi_i\psi^*_j$ where ψ_i is the scattering state probability amplitude at orbital site i. We can obtain a finite-difference analog of the continuum flux operator by defining

$$\mathbf{j}_i = \sum_j j_{i\to j}\frac{\mathbf{r}_j - \mathbf{r}_i}{|\mathbf{r}_j - \mathbf{r}_i|^2}, \tag{5.6.2}$$

which computes the vector sum of each bond current associated with a given orbital[119][2].

In Figs. 5.6.10 and 5.6.11, we have color-coded the bond current by the sublattice of the origin site, which shows the strong presence of small vortices alternating between the sublattices. These strong vortices indicate the mechanism by which the resonant state is able to “trap” the electron away from the leads. As expected, the

---

[2]. A quick derivation shows that $\mathbf{j}_i \propto \frac{\hbar}{m}\mathrm{Im}\left[\psi^*\nabla\psi\right]_i$ for the finite-difference Hamiltonian, as expected.

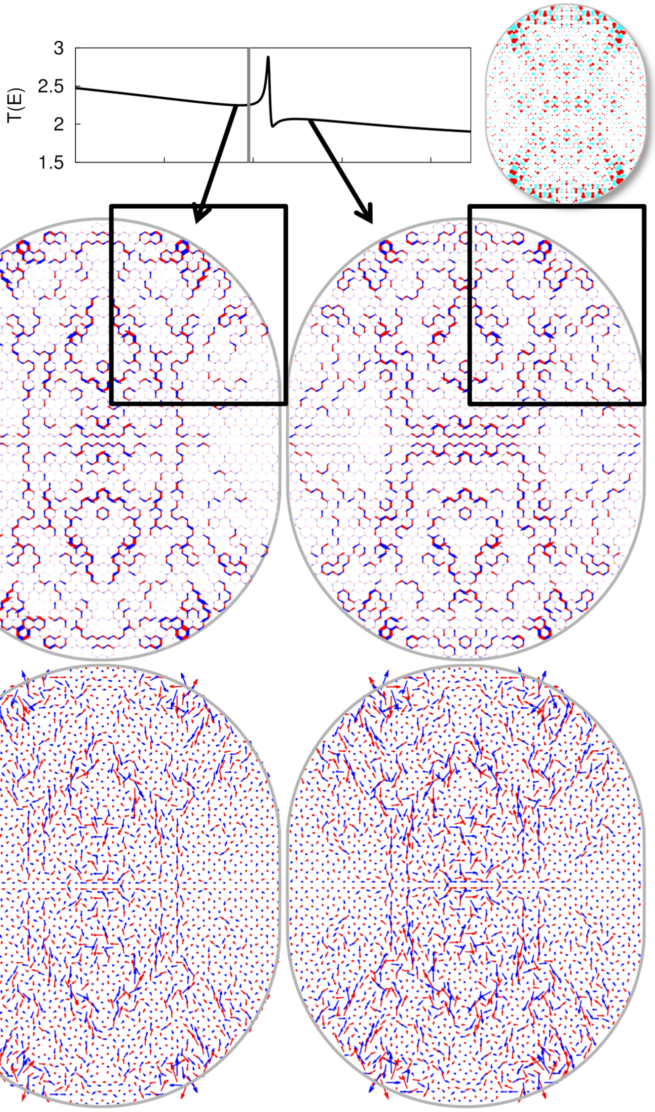

Figure 5.6.10: At top, the bond currents for the scattering wavefunction at energies $E = 1.9582t$ and $1.9586t$ are shown with the originating vector color-coded red (blue) for sublattice A (B). If the bond currents flowing in and out of each lattice site are summed, we obtain a finite-difference approximation to the probability flux, shown at bottom.

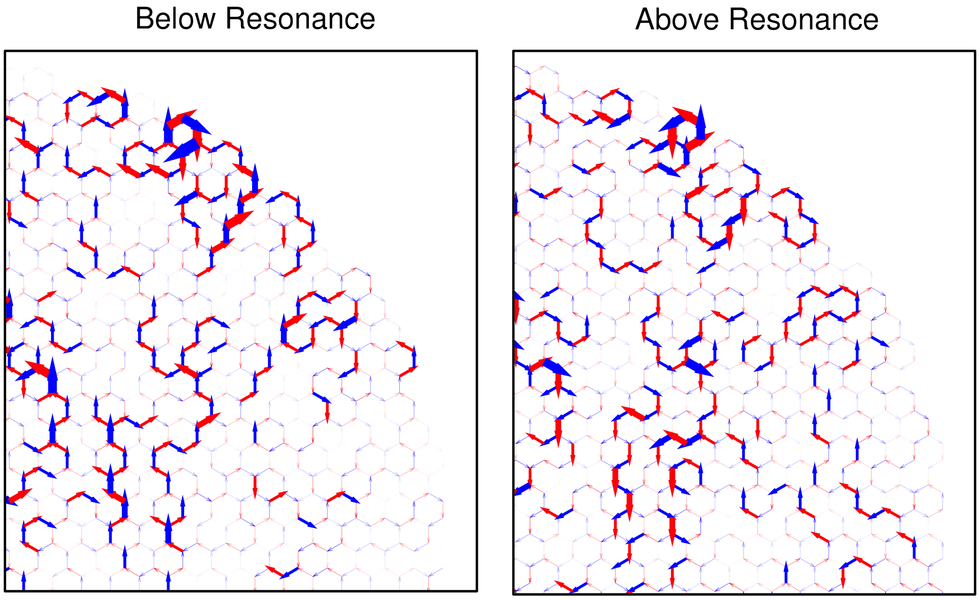

Figure 5.6.11: Magnified views from the bond currents in Fig. 5.6.10, showing that bond-current vortices are able to "trap" the electron in cyclical orbits. Due to the π phase shift, these vortices flip across resonance.

direction of flow reverses below and above resonance, consistent with the π phase shift of the indirect channel.

Fig. 5.6.12 shows the results of adding the Husimi flux maps of both valleys at two energies, below and above resonance. We find sources and drains in the summed Husimi flux map at the corners of the system where the classical paths of the K'-valley Husimi map (Fig. 5.6.3) reflect off the system boundary.

To understand why, we consider that during transmission, quasiparticles enter from the left incoming lead and exit through the right outgoing lead. However, near resonance, the wavefunction is strongly weighted by the closed-system eigenstate, which has *no* net quasiparticle current. Husimi maps for either valley also reflect this fact: they are indistinguishable from the Husimi maps of the closed-system eigenstate in Fig. 5.6.3, and the two valleys are inverse images of each other.

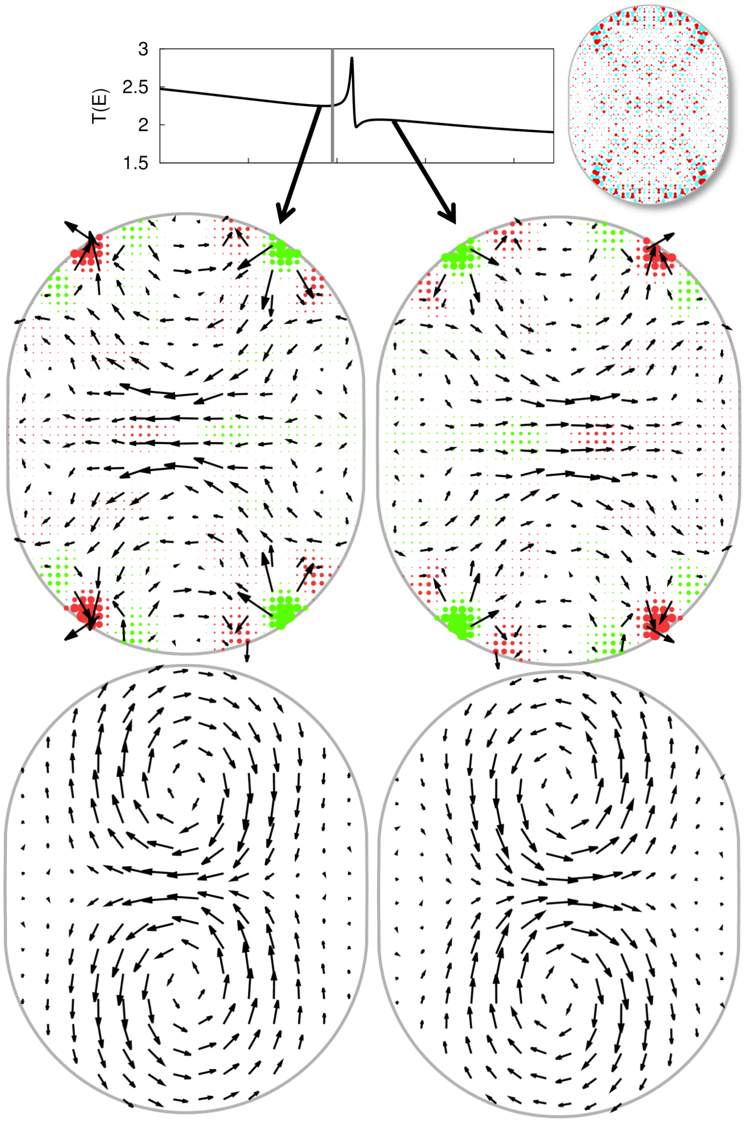

Figure 5.6.12: Above and below the Fano resonance in Figs. 5.6.9 (inset), the time-reversal symmetry between the K and K' valleys is lifted, making it possible to add the Husimi flux for both valleys to measure valley-polarized current. Above, the Husimi flux maps of both valleys are added for the scattering wavefunction at energies $E = 1.9582t$ and $1.9586t$, with $\Delta k/k = 30\%$. Below, the probability flux is shown, convolved with a Gaussian kernel of the same size as the coherent state. At energies this close to resonance, the wavefunction does not visually change from the closed-system eigenstate, shown in the inset, but the residual valley-polarized current that occurs near these resonances switches direction across resonance. This seems to be a phenomenon which likely accompanies most Fano resonances in graphene systems.

But the Husimi maps for the two valleys don't exactly cancel each other out. When we add them together to reveal the time-reversal asymmetric behavior of the wavefunction, the residual shows sources and drains of net quasiparticle flow which are strongly related to the Husimi maps for each valley, and do *not* show left-to-right transmission. Instead, the summed Husimi flux map shows the influence of transmission on the strongly-emphasized classical paths underlying the closed-system eigenstate.

Convolving the flux defined in Eq. 5.6.2 with a Gaussian kernel of the same spread as the coherent state used to generate the Husimi map creates an analog to the Husimi flux. While the convolved flux does not distinguish among valleys, it can help make sense of localized bond currents which are nearly impossible to interpret when the current flows are not constrained along a particular direction[119, 118]. We show the convolved flux at the bottom of Fig. 5.6.12, and find that it forms vortices which correlates with the summed Husimi flux maps for both valleys, and also fails to show the left-to-right flow responsible for transmission.

This behavior is directly analogous to flux in continuum systems, where flux vortices above and below resonance show local variations of flow but not the left-to-right flow responsible for transmission (see Fig. 4.4.4). Because of the π phase shift of the indirect channel across resonance, the local flows reverse direction above and below resonance, but they do not affect the overall drift velocity except exactly on resonance. We can recover the left-to-right drift velocity only by examining the system at larger scales using a larger Gaussian spread (Fig. 5.6.13)[3]. Like the continuum case in Fig. 4.4.4, the convolved current below and above resonance switches between

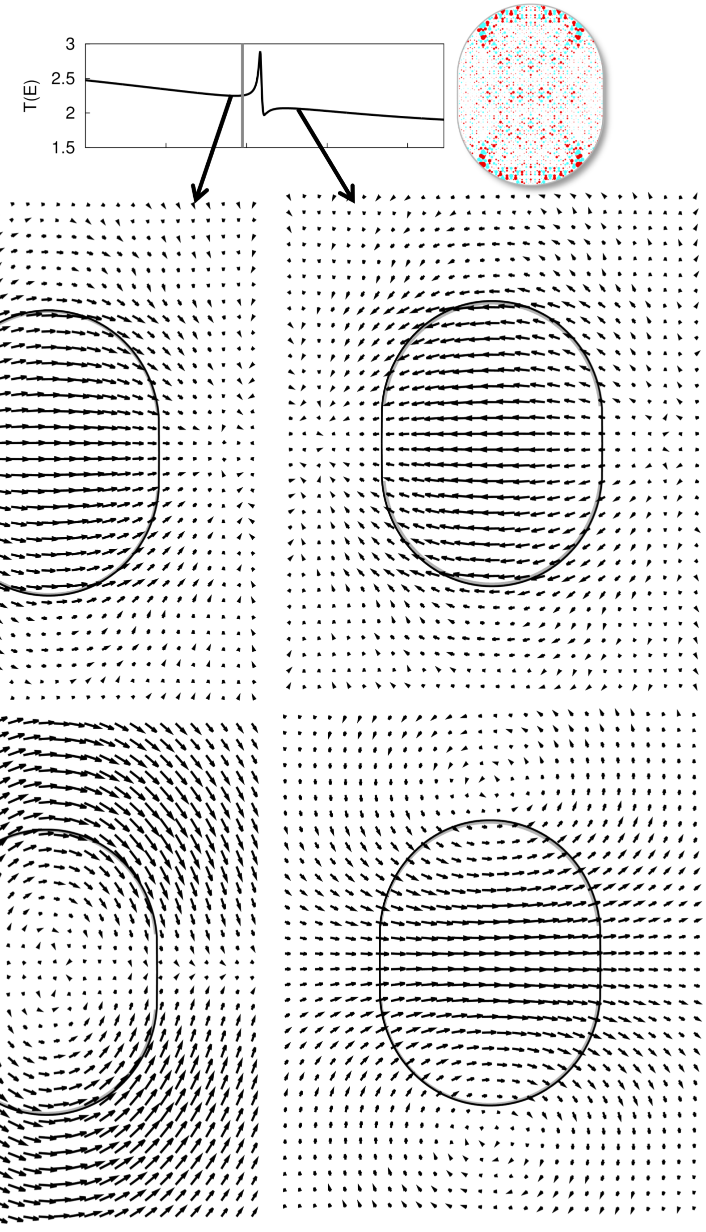

Figure 5.6.13: At top, the extended Husimi flux is shown for the K' valley at $E = 1.9582t$ and $1.9586t$, with $\Delta k/k = 5\%$. Below, the probability flux is shown, convolved with a Gaussian kernel of the same size as the coherent state. Even though the direction of the Husimi flux reverses across resonance, the convolved current remains largely left-to-right in analogy to Fig. 4.4.4.

extending vertically (below) or contracting (above). Interestingly, for the honeycomb lattice, net probability flux does not always equate to net particle flow in the same direction; in this case, the two anti-correlate.

For laterally symmetric systems like the graphene stadium billiards in this section, Fano resonances are often associated with a symmetric quasi-bound state which interferes with a non-symmetric direct channel, and undergoes a π phase shift across resonance. As a result, Fano resonances can leave their mark on the scattering wavefunction by inducing lateral asymmetries in the the scattering wavefunction. Because of the π phase shift, asymmetrical features below resonance reverse their lateral orientation above resonance.

The stable orbits that are emphasized by the quasi-bound state can be dramatically disturbed by slight modifications of the boundary, if those modifications happen at the scattering points most relevant to the orbit. The original authors Huang et al.[41] examined the relationship between system symmetry and strength of the Fano resonances by slightly modifying the system boundary at the black circle in Fig. 5.6.3, and demonstrated that some resonances were drastically reduced by this modification.

We have chosen the resonance in this study because the Fano resonance profile associated with it was among the most-reduced as a result of their system modification, and our analysis provides a clear picture as to why: the authors perturbed the system precisely where the eigenstate in Fig. 5.6.3 has the largest probability amplitude at the boundary. With the semiclassical picture, we are able to add to this finding an intuitive understanding: by disturbing the reflection angle at the exact point where the two valleys scatter, each time the electron scatters off that point some of its probability leaves the stable orbit. The authors effectively introduced a leak into the orbit, reducing its lifetime and the strength of its resonance considerably.

In another study, we explored the relationship between the direct and indirect channels by reducing the quantum dot to a two-state subspace: one state being the indirect channel eigenstate in Fig. 5.6.3, designated as $|\phi_{\text{indirect}}\rangle$, the other being any other orthogonal state of our choice, written as $|\phi_{\text{direct}}\rangle$. We write out a new Hamiltonian from the two-terminal geometry (Eq. 1.3.13) as

$$H_{\text{(in)direct,(in)direct}} = \left\langle \phi_{\text{(in)direct}} \left| H \right| \phi_{\text{(in)direct}} \right\rangle \tag{5.6.3}$$

and

$$V_{\text{(in)direct},L(R)} = \left\langle \phi_{\text{(in)direct}} \right| V_{CL(CR)}. \tag{5.6.4}$$

This reduces the Hamiltonian of the central region to a dense 2 × 2 matrix, allowing the formalism in Chapter 1 to remain the same.

Using the eigenstates of the closed system as the set of direct states $\{|\phi_{\text{direct}}\rangle\}$, we are able to produce various Fano resonance profiles depending on our choice. The state associated with eigenstate index 1475 (see Fig. 5.6.14), produces the most similar profile to the full simulation in Fig. 5.6.9.

In our two-state study, all direct states that produce a Fano profile with the symmetric indirect channel share the following properties:

1. They have large amplitude at the region bordering the leads
2. Their boundary amplitudes overlap the relevant eigenchannel
3. They exhibit lateral *anti*symmetry

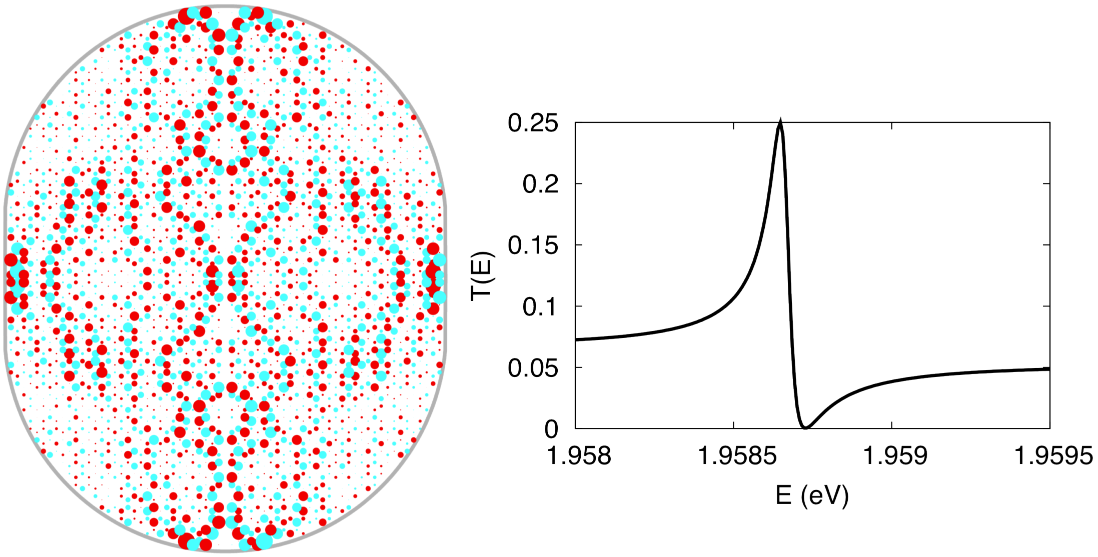

Figure 5.6.14: A laterally antisymmetric direct channel in the reduced two-state Fano study is shown alongside its resonance profile with the symmetric indirect channel from Fig. 5.6.3.

The last point is crucial since the indirect state is horizontally symmetrical. Just as an atomic s-orbital (spatially symmetric) and p-orbital (spatially antisymmetric) hybridize to form a spatial asymmetric wavefunction, the direct and resonant states hybridize to form asymmetrical scattering states. For more general studies, the direct channel is a hybrid of many closed-system eigenstates and is asymmetric as opposed to strictly antisymmetric.

The Husimi flux can also cast insight onto the scattering states associated with this resonance. For instance, we can examine the direct channel by a simple mathematical manipulation. Taking the scattering wavefunction Ψ of the resonant state, we can subtract the contribution from the quasi-bound state obtained by diagonalizing the perturbed Hamiltonian $H' = H + \Sigma_L + \Sigma_R$ where $\Sigma_{L(R)}$ is the self-energy contribution from the left (right) lead. Of the complex eigenstates $\{\phi_i\}$, only one will have an inner

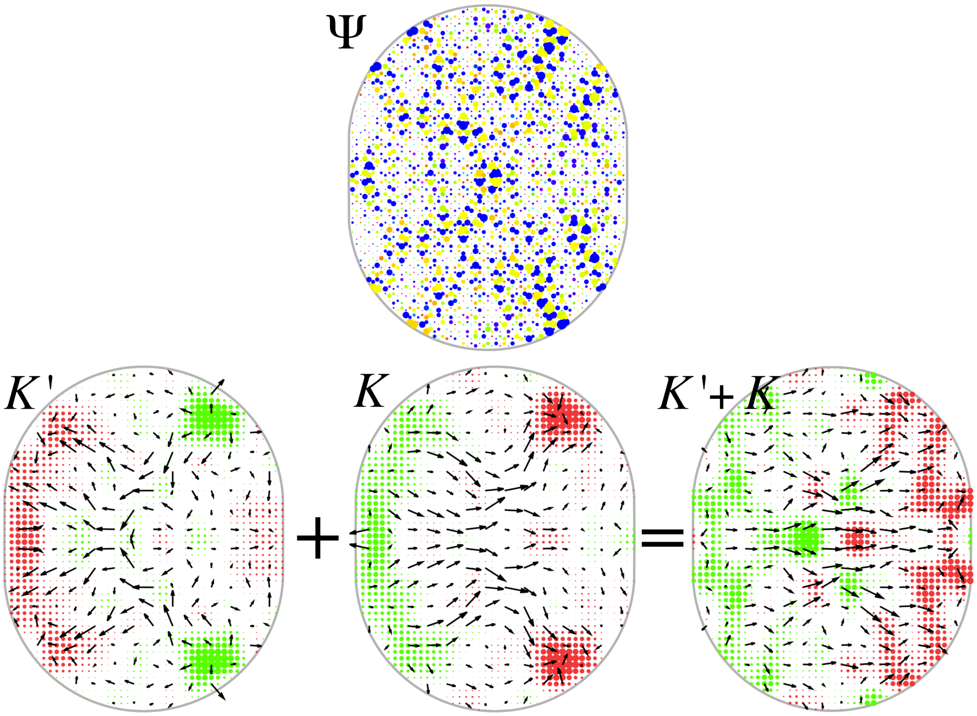

Figure 5.6.15: The wavefunction (top) of the direct channel, and the Husimi flux for the K', K, and $K' + K$ valleys showing overall flow from left-to-right. These maps are taken from the center of the resonance at $E = 1.9584$eV, and do not noticeably change across resonance.

product $\langle \phi_i | \Psi \rangle$ close to one – this is the indirect channel which we label as ϕ_{indirect}. The direct channel is obtained by

$$|\phi_{\text{direct}}\rangle = |\Psi\rangle - |\phi_{\text{indirect}}\rangle \langle \phi_{\text{indirect}} | \psi\rangle \,. \tag{5.6.5}$$

We show the direct channel, and its Husimi maps, in Fig. 5.6.15.

For this resonance, the direct channel also has strong closed-system character. Sources and drains for both valleys occur along boundaries not connected by leads, and the maps for both valleys are approximately inverses of each other. This helps explain why the direct channel is so easily affected by the indirect channel in Fig. 5.6.12, since it is also trapping the electron in a quasi-bound state.

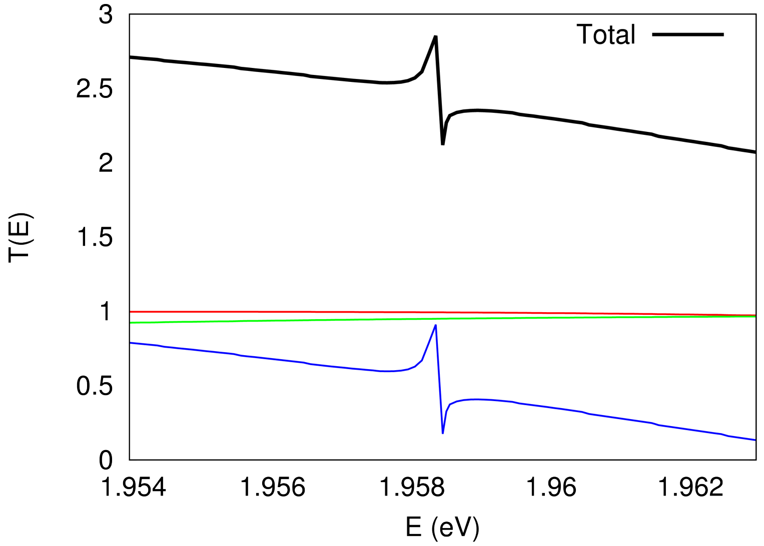

Figure 5.6.16: The transmission function (Total) is decomposed into individual transmission modes, with the Fano resonance clearly modulating quickly in blue. The other modes in red and green barely change over the energy range. One of those modes and its Husimi maps are shown in Fig. 5.6.17.

During a Fano resonance, other modes are also transmitting across the device, unperturbed by the quasi-bound state responsible for the resonance. In Fig. 5.6.16, we show the transmission matrix, decomposed according to the singular value decomposition

$$t = U^{\dagger}\Sigma V. \tag{5.6.6}$$

The columns of U and V are incoming and outgoing wavefunctions defined on the boundary of the scattering region, and the singular values in Σ give their respective transmission values. In Fig. 5.6.17, we show one of the full-transmission scattering wavefunctions, showing that transmission occurs almost entirely in the K' valley. Unlike the direct and indirect channels (Fig. 5.6.12 and 5.6.15), the Husimi flux maps for both valleys in this scattering state combine to reveal unambiguous left-to-right flow even at small scales.

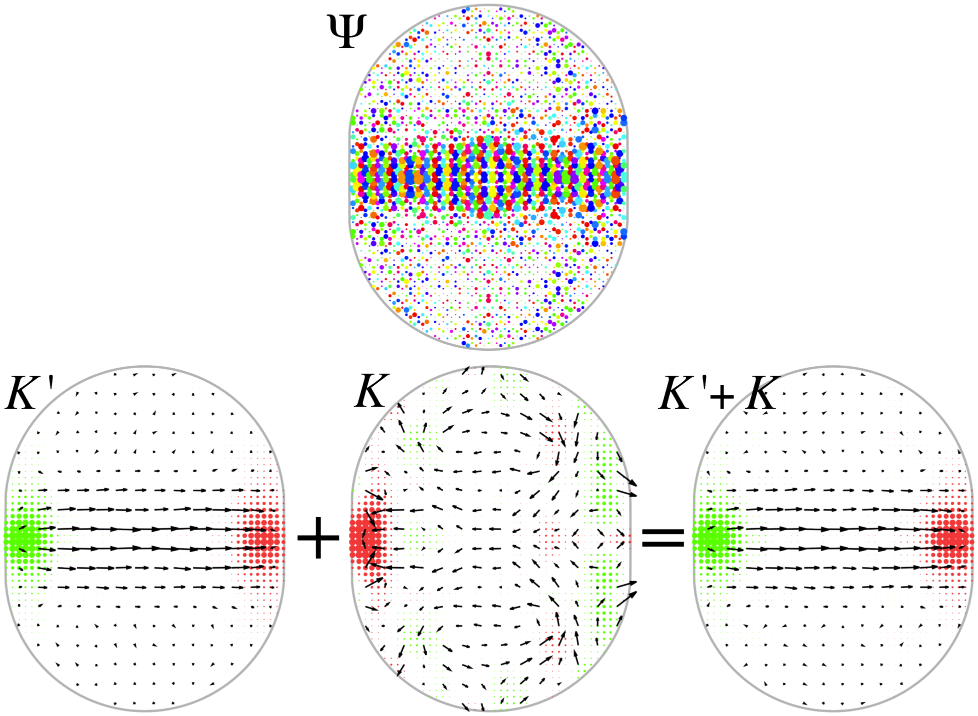

Figure 5.6.17: The wavefunction (top) of another full-transmission channel, and the Husimi flux for the K', K, and $K' + K$ valleys showing overall flow from left-to-right. Current in this state is entirely provided by the K' valley – contributions from the K valley are minor perturbations. These maps are taken from the center of the resonance at $E = 1.9584$eV, and do not noticeably change across resonance.

Appendix A

Uncertainty Propagation for Husimi Vector Addition

When integrating over the available k-space in Eq. 4.2.3, the resulting Husimi flux vector has lower uncertainty than the individual terms in the integral, but by how much? Understanding this mathematical detail is key to appreciating why the Husimi projection is valuable to extending the flux operator to an operator with defined uncertainty. Moreover, understanding the behavior of uncertainty propagation in this integral makes it possible to confidently approximate the result with a discrete sum, such as the sunbursts in Fig. 4.2.1, offering both visual and computational advantages.

We begin by considering the extreme cases. If the wavevector orientation remains unchanged for each measurement, summing up identical measurements has no effect on the final relative uncertainty. On the other hand, when either the spatial coordinates or the wavevectors are sufficiently separated, each Husimi vector constitutes an independent measurement; the uncertainty of the result will reduce by the square root of the number of measurements. In general, calculations fall in between these two extremes.

This analysis is concerned with only one dimension, since the variance along each orthogonal axis can simply be summed. First, the coherent state is expressed in the momentum basis as

$$\langle \mathbf{k} | \, \mathbf{r}_0, \mathbf{k}_0, \sigma \rangle \;=\; \left(\frac{\sigma}{\sqrt{\pi/2}} \right)^{1/2} e^{-\sigma^2 (\mathbf{k}-\mathbf{k}_0)^2 + i(\mathbf{k}-\mathbf{k}_0)\cdot \mathbf{r}_0}. \tag{A.0.1}$$

Most generally, the Husimi projection in Eq. 4.2.3 is the integral of Husimi functions over all of k-space. In this appendix, and in the figures throughout this paper, the integral is replaced with a finite sum of test wavevectors $\{\mathbf{k}_i\}$ which satisfy the dispersion relation at a particular energy.

The variance of the integral in Eq. 4.2.3 can be obtained by building on intuition about coherent states. It is well-known that the k-space variance of the coherent state can be simply derived by integrating the coherent state probability amplitude over k-space, weighting the integrand by $(\mathbf{k} - \mathbf{k}_0)^2$. Using the notation in Eq. A.0.1, this gives $\sigma_k^2 = \frac{1}{4\sigma_x^2}$ yielding the familiar relation $\sigma_x \sigma_k = \frac{1}{2}$. This can be thought of in the Husimi formulation as a statistical result where the quantity σ_k is the variance of each individual term in the Husimi vector summation. In this formulation, the variable is the wavevector and the probability function is the probability amplitude of the coherent state. Because the probability function is complex, we have to take the absolute sum squared.

Factoring in more than one Husimi function into the Husimi projection results in the expression

$$\frac{\sigma}{\sqrt{\pi/2}}\int_{-\infty}^{\infty}\left|\sum_i \left(k-k_i\right)e^{-\sigma^2(k-k_i)^2+i(k-k_i)x_0}\right|^2 dk, \tag{A.0.2}$$

where the set $\{\mathbf{k}_i\}$ are the set of test wavevectors, projected onto the given axis, x_0 is the spatial point being tested, and σ is the chosen spatial Gaussian spread. Setting the coherent states to the same phase at their centers, $x_0 = 0$, and the above integral can be evaluated to return

$$\sigma_k^2 = \frac{1}{4\sigma^2}\left(N + 2\sum_{i,j>i} e^{-\frac{\sigma^2}{2}(k_i-k_j)^2}\left(1-\sigma^2\left(k_i-k_j\right)^2\right)\right). \tag{A.0.3}$$

Already it is possible test this result against intuition. If each wavevector is identical, then $k_i - k_j = 0$ and the sum of N measurements results in the uncertainty $\sigma_k^2 = \frac{N^2}{4\sigma^2}$ which would provide no reduction of relative uncertainty. For large values of $|k_i - k_j| \gg \sigma$, the exponential term will overwhelm the quadratic term and the uncertainty becomes $\sigma_k^2 = \frac{N}{4\sigma^2}$, a reduction in the relative uncertainty of $\sqrt{N}$.

Perhaps most surprising about Eq. A.0.3 is that the second term, which quantifies the covariance between the two measurements, can actually be negative. What are its bounds? Fig. A.0.1 plots the quantity $Q(k_1, k_2, \sigma) = 2e^{-\frac{\sigma^2}{2}(k_2-k_1)^2}\left(1-\sigma^2\left(k_2-k_1\right)\right)$, showing that a minimum value of $-\frac{4}{e^{3/2}} \approx -0.893$ is achieved at $|k_2 - k_1| = \sqrt{3}/\sigma$. Every value of $|k_2 - k_1|$ beyond which Q goes through zero has achieved nearly independent measurements, which is found at $|k_2 - k_1| = \sigma^{-1}$.

The terms in Eq. A.0.3 suggest that when more and more vectors are added the uncertainty can be reduced arbitrarily by setting the correct separations between the test wavevectors. It even suggests that for three or more vectors we could possibly produce results with negative uncertainty, but intuitively that cannot be possible.

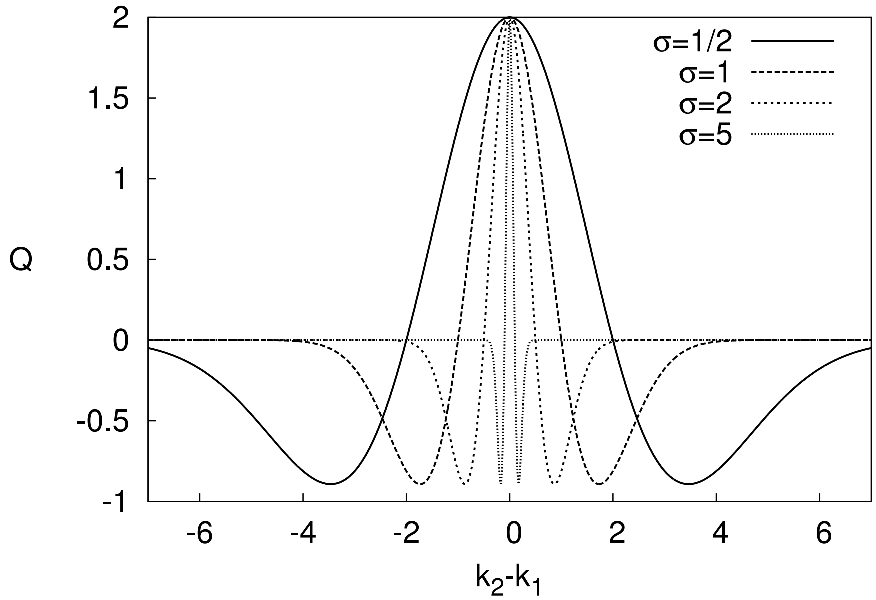

Figure A.0.1: The second term in Eq. A.0.3 is plotted for the addition of two vectors in the Husimi projection. This term represents the covariance between the two vectors, and is bounded above by 2 and below by $-\frac{4}{e^{3/2}}$ for all choices of σ.

To appreciate why from an analytical perspective, Fig. A.0.2 plots the results of σ_k^2 for the addition of three wavevectors. The minima that occur from maximizing the separation between each pair of wavevectors is indicated by the white dashed lines. At the center of the graph, a peak exists at $\sigma_k^2 = 9/4\sigma^2$, which falls to $3/4\sigma^2$ for areas beyond the area bounded by the white dashed lines, consistent with earlier observations. There is also a minimum (positive) uncertainty which arises from the fact that the separation between all pairs of points on a line cannot be equal. In Fig. A.0.2 this is evidenced by the fact that there are no points where three dashed lines intersect. For two vectors the minimum occurs at $\sigma_k^2 \approx 0.981/4\sigma^2$, for three $\sigma_k^2 \approx 1.017/4\sigma^2$ and for four $\sigma_k^2 \approx 1.036/4\sigma^2$. We can generalize and state that for $N_{\min}$ vectors that fall on separate minima, the uncertainty of their sum will be $\sigma_k \approx \frac{1}{2N_{\min}\sigma}$.

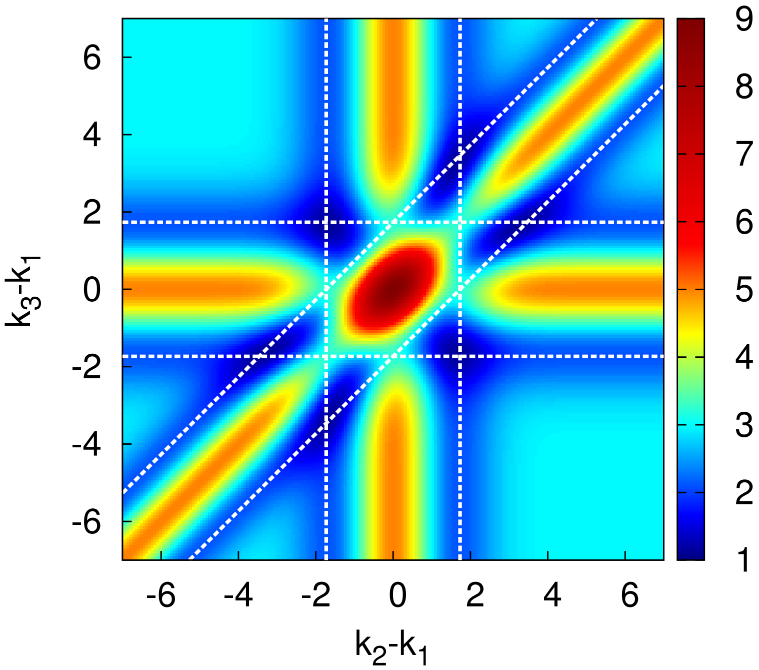

Figure A.0.2: The uncertainty that results from summing three vectors of a Husimi projection, as written in Eq. A.0.3 is plotted. The uncertainty is bounded above by $9/4\sigma^2$ and below by $\sim 1.017/4\sigma^2$. The dashed white lines indicate local minima that result from spacing each pair of vectors by $\sqrt{3}/\sigma$, which would give a minimum uncertainty for two-vector addition (see Fig. A.0.1).

Moreover, even if vectors are added that do not fall on the uncertainty minima in Figs. A.0.1 and A.0.2, they will have a negligible impact on the total relative uncertainty. So no matter how many vectors contribute to the sum, only the vectors on the minima will reduce the relative uncertainty, making the key quantity not the total number of vectors that are added, but the number that have sufficient separation to fall on the uncertainty minima.

How many vectors is this? We know, for instance, that this minimum will occur when the maximum number of vector pairs have a separation near $\sqrt{3}/\sigma$, and that this is likely to occur when they are evenly spaced on a line at that separation. Thus we propose that the number of vectors that can fall on the minima is given by

$N_{\min} = \text{floor}\left(2k(E)\sigma/\sqrt{3}\right)$, and using $\hbar k = \sqrt{2mE}$, we can rewrite this as $N_{\min} = \text{floor}\left(\sigma\sqrt{\frac{8mE}{3\hbar^2}}\right)$. Substituting this value results in the proportionalities

$$\Delta k/k \propto \frac{1}{N_{\min}\sigma} \propto \left(\frac{\sigma}{\hbar}\sqrt{mE}\right)^{-1}. \tag{A.0.4}$$

This makes sense intuitively: the relative uncertainty of a finely sampled Husimi vector addition goes down with larger σ and energy.

This result deepens the connection between the flux operator and the Husimi function for small σ, since for very small coherent states, the uncertainty minima, which are separated by σ^{-1}, grow increasingly far apart. There is only a finite range of wavevectors which satisfy the dispersion relation at a given energy, meaning that as the coherent states get smaller, fewer and fewer samples in k-space minimize the uncertainty. In fact, at the extreme limit of $\sigma \to 0$, the uncertainty cannot be minimized beyond a single measurement in each orthogonal direction, indicating that results for these small coherent states have undefined uncertainty, just like the flux operator. We corroborate this result using a different proof in Eq. 4.1.21.

Bibliography

[1] Douglas J. Mason, David Prendergast, Jeffrey B. Neaton, and Eric J. Heller. Algorithm for efficient elastic transport calculations for arbitrary device geometries. *Phys. Rev. B*, 84:155401, Oct 2011.

[2] Douglas J. Mason, Mario Borunda, and Eric J. Heller. *The Boundary Reflection Matrix for Arbitrary Cuts in Lattices.* (in preparation), 2012.

[3] Douglas J. Mason, Mario F. Borunda, and Eric J. Heller. Extending the concept of probability flux. (unpublished) arXiv:1205.3708.

[4] Douglas J. Mason, Mario F. Borunda, and Eric J. Heller. A semiclassical interpretation of probability flux. (unpublished) arXiv:1205.0291.

[5] Douglas J. Mason, Mario Borunda, and Eric J. Heller. Husimi projections in lattices. (in preparation) arXiv:1206.1013, 2012.

[6] Douglas J. Mason, Mario Borunda, and Eric J. Heller. Husimi projections in graphene. (in preparation).

[7] John H. Davies. *The Physics of Low-Dimensional Semiconductors: An Introduction.* Cambridge University Press, 1998.

[8] A. K. Geim and K. S. Novoselov. The rise of graphene. *Nature Materials*, 6(3):183–191, 03 2007.

[9] N.W. Ashcroft and N.D. Mermin. *Solid state physics*. Holt-Saunders International Editions: Science : Physics. Holt, Rinehart and Winston, 1976.

[10] Vitor M. Pereira, A. H. Castro Neto, and N. M. R. Peres. Tight-binding approach to uniaxial strain in graphene. *Phys. Rev. B*, 80:045401, Jul 2009.

[11] P. R. Wallace. The band theory of graphite. *Phys. Rev.*, 71:622–634, May 1947.

[12] A. H. Castro Neto, F. Guinea, N. M. R. Peres, K. S. Novoselov, and A. K. Geim. The electronic properties of graphene. *Rev. Mod. Phys.*, 81(1):109–162, Jan 2009.

[13] Cleve Moler and Charles Van Loan. Nineteen dubious ways to compute the exponential of a matrix. *SIAM Review*, 20:801–836, 1978.

[14] R. B. Sidje. Expokit: A software package for computing matrix exponentials. *ACM Trans. Math. Softw.*, 24(1):130–156, 1998.

[15] Pekka Koskinen, Sami Malola, and Hannu Häkkinen. Self-passivating edge reconstructions of graphene. *Phys. Rev. Lett.*, 101:115502, Sep 2008.

[16] J. A. M. van Ostaay, A. R. Akhmerov, C. W. J. Beenakker, and M. Wimmer. Dirac boundary condition at the reconstructed zigzag edge of graphene. *Phys. Rev. B*, 84:195434, Nov 2011.

[17] R. Landauer. Spatial variation of currents and fields due to localized scatterers in metallic conduction. *IBM Journal of Research and Development*, 1(3):223 –231, july 1957.

[18] M. P. López-Sancho and J. Rubio. Quick iterative scheme for the calculation of transfer matrices: application to mo (100). *J. Phys. F.: Met. Phys.*, 14:1205–1215, 1984.

[19] M. P. López-Sancho and J. Rubio. Highly convergent schemes for the calculation of bulk and surface green functions. *J. Phys. F.: Met. Phys.*, 15:851–858, 1985.

[20] M. Büttiker, Y. Imry, R. Landauer, and S. Pinhas. Generalized many-channel conductance formula with application to small rings. *Phys. Rev. B*, 31:6207–6215, May 1985.

[21] B. Huard, J. A. Sulpizio, N. Stander, K. Todd, B. Yang, and D. Goldhaber-Gordon. Transport measurements across a tunable potential barrier in graphene. *Physical Review Letters*, 98(236803), 2007.

[22] Y.-W. Tan, Y. Zhang, K. Bolotin, Y. Zhao, S. Adam, E. H. Hwang, S. Das Sarma, H. L. Stormer, and P. Kim. Measurement of scattering rate and minimum conductivity in graphene. *Physical Review Letters*, 99(246803), 2007.

[23] Fangping OuYang, Jin Xiao, Rui Guo, Hua Zhang, and Hui Xu. Transport properties of t-shaped and crossed junctions based on graphene nanoribbons. *Nanotechnology*, 20(5):055202, 2009.

[24] B. Ozyilmax, P. Jarillo-Herrero, D. Efetov, and P. Kim. Electronic transport in

locally gated graphene nanoconstrictions. *Applied Physics Letters*, 91(192107), 2007.

[25] F. Sols, F. Guinea, and A. H. Castro Neto. Coulomb blockade in graphene nanoribbons. *Physical Review Letters*, 99(166803), 2007.

[26] Wei L. Wang, Oleg V. Yazyev, Sheng Meng, and Efthimios Kaxiras. Topological frustration in graphene nanoflakes: Magnetic order and spin logic devices. *Phys. Rev. Lett.*, 102(15):157201, Apr 2009.

[27] S. Datta. *Electronic Transport in Mesoscopic Systems*. Cambridge University Press, Cambridge, 1997.

[28] E. Cuthill and J. McKee. Reducing the bandwidth of sparse symmetric matrices. In *Proceedings of the 1969 24th national conference*, pages 157–172, New York, NY, USA, 1969. ACM.

[29] James W. Demmel. *Applied Numerical Linear Algebra*. SIAM, 1997.

[30] James W. Demmel, Stanley C. Eisenstat, John R. Gilbert, Xiaoye S. Li, and Joseph W. H. Liu. A supernodal approach to sparse partial pivoting. *SIAM J. Matrix Analysis and Applications*, 20(3):720–755, 1999.

[31] Yigal Meir and Ned S. Wingreen. Landauer formula for the current through an interacting electron region. *Phys. Rev. Lett.*, 68(16):2512–2515, Apr 1992.

[32] Timothy A. Davis. *Direct Methods for Sparse Linear Systems*. SIAM, 2006.

[33] A. Svizhenko, M. P. Anamtram, T. R. Govindand, B. Biegel, and R. Venugopal. Two-dimensional quantum mechanical modeling of nanotransistors. *Journal of Applied Physics*, 91(4):2343, 2002.

[34] S. Cauley, J. Jain, C.-K. Koh, and V. Balakrishnan. A scalable distributed method for quantum-scale device simulation. *Journal of Applied Physics*, 101(123715), 2007.

[35] T. Usuki, M. Takatsu, R. A. Kiehl, and N. Yokoyama. Numerical analysis of electron-wave detection by a wedge-shaped point contact. 1994.

[36] Harold U. Baranger, David P. DiVincenzo, Rodolfo A. Jalabert, and A. Douglas Stone. Classical and quantum ballistic-transport anomalies in microjunctions. *Phys. Rev. B*, 44(19):10637–10675, Nov 1991.

[37] D Mamaluy, D Vasileska, M Sabathil, T Zibold, and P Vogl. Contact block reduction method for ballistic transport and carrier densities of open nanostructures, Phys. *Rev. B*, 71(24):245321, 2005.

[38] Michael Wimmer and Klaus Richter. Optimal block-tridiagonalization of matrices for coherent charge transport. *Journal of Computational Physics*, 228(23):8548–8565, 2009.

[39] Zhenhua Qiao and Jian Wang. A variant transfer matrix method suitable for transport through multi-probe systems. *Nanotechnology*, 18(43):435402, 2007.

[40] L. Kaplan and E. J. Heller. Weak quantum ergodicity. *Physica D: Nonlinear Phenomena*, 121(1-2):1 – 18, 1998.

[41] Liang Huang, Ying-Cheng Lai, David Ferry, Stephen Goodnick, and Richard Akis. Relativistic Quantum Scars. *Phys. Rev. Lett.*, 103(5):1–4, July 2009.

[42] F. Muñoz Rojas, D. Jacob, J. Fernández-Rossier, and J. Palacios. Coherent transport in graphene nanoconstrictions. *Physical Review B*, 74(19):1–8, 2006.

[43] U. Fano. Effects of configuration interaction on intensities and phase shifts. *Phys. Rev.*, 124(6):1866–1878, Dec 1961.

[44] E. R. Racec, U. Wulf, and P. N. Racec. Fano regime of transport through open quantum dots. *Phys. Rev. B*, 82:085313, Aug 2010.

[45] Holger Hennig, Ragnar Fleischmann, Lars Hufnagel, and Theo Geisel. Fractal conductance fluctuations of classical origin. *Physical Review E*, 76:015202, 2007.

[46] Roland Ketzmerick. Fractal conductance fluctuations in generic chaotic cavities. *Phys. Rev. B*, 54:10841–10844, Oct 1996.

[47] A. S. Sachrajda, R. Ketzmerick, C. Gould, Y. Feng, P. J. Kelly, A. Delage, and Z. Wasilewski. Fractal conductance fluctuations in a soft-wall stadium and a sinai billiard. *Phys. Rev. Lett.*, 80:1948–1951, Mar 1998.

[48] Jakob J. Metzger, Ragnar Fleischmann, and Theo Geisel. Universal statistics of branched flows. *Phys. Rev. Lett.*, 105:020601, Jul 2010.

[49] M.V. Berry and C. Upstill. Iv catastrophe optics: Morphologies of caustics and their diffraction patterns. volume 18 of *Progress in Optics*, pages 257 – 346. Elsevier, 1980.

[50] Luise Couchman, Edward Ott, and Thomas M. Antonsen. Quantum chaos in systems with ray splitting. *Phys. Rev. A*, 46:6193–6210, Nov 1992.

[51] M. S. Custódio and M. W. Beims. Intrinsic stickiness and chaos in open integrable billiards: Tiny border effects. *Phys. Rev. E*, 83:056201, May 2011.

[52] Henrik Bruus and Niall D Whelan. Edge diffraction, trace formulae and the cardioid billiard. *Nonlinearity*, 9(4):1023, 1996.

[53] M. Wimmer, A. R. Akhmerov, and F. Guinea. Robustness of edge states in graphene quantum dots. *Phys. Rev. B*, 82(4):045409, Jul 2010.

[54] K. Husimi. Some formal properties of the density matrix. *Proc. Phys. Math. Soc. Jpn.*, 22:264–314, 1940.

[55] W. Gale, E. Guth, and G. T. Trammell. Determination of the quantum state by measurements. *Phys. Rev.*, 165:1434–1436, Jan 1968.

[56] Yakir Aharonov and Lev Vaidman. Measurement of the schrödinger wave of a single particle. *Physics Letters A*, 178:38 – 42, 1993.

[57] M. Daumer, D. Dürr, S. Goldstein, and N. Zanghi. On the quantum probability flux through surfaces. *Journal of Statistical Physics*, 88:967–977, 1997.

[58] P.W. O'Connor and S. Tomsovic. The unusual nature of the quantum baker's transformation. *Annals of Physics*, 201(1):218–264, 1991.

[59] M.S. Child, G. Bruun, and R. Paul. Short time quantum phase space dynamics at a 1:2 fermi resonance. *Chemical Physics*, 190:373 – 380, 1995. Overtone Spectroscopy and Dynamics.

[60] E. J. Heller. Wavepacket dynamics and quantum chaology. In M. J. Giannoni, A. Voros, and J. Zinn-Justin, editors, *Proceedings of the 1989 Les Houches Summer School on "Chaos and Quantum Physics"*, pages 546–663, North-Holland, 1989. Elsevier Science Publishers B.V.

[61] Barbara Goss Levi. Do oxide superconductors behave as fermi liquids? *Physics Today*, 43(3):20–22, 1990.

[62] Barbara Goss Levi. In high-t[sub c] superconductors, is d-wave the new wave? *Physics Today*, 46(5):17–20, 1993.

[63] Barbara Goss Levi. Experiments probe the wavefunction of electron pairs in high-t[sub c] superconductors. *Physics Today*, 49(1):19–22, 1996.

[64] Andrea Damascelli. Probing the electronic structure of complex systems by arpes. *Physica Scripta*, 2004(T109):61, 2004.

[65] M.C. Gutzwiller. *Chaos in classical and quantum mechanics*. Interdisciplinary applied mathematics. Springer-Verlag, 1990.

[66] L. Kaplan and E. J. Heller. Measuring scars of periodic orbits. *Phys. Rev. E*, 59(6):6609–6628, Jun 1999.

[67] W. E. Bies, L. Kaplan, M. R. Haggerty, and E. J. Heller. Localization of eigenfunctions in the stadium billiard. *Phys. Rev. E*, 63:066214, May 2001.

[68] R. W. Robinett. Visualizing the solutions for the circular infinite well in quantum and classical mechanics. *American Journal of Physics*, 64(4):440–446, 1996.

[69] R. Peierls. Zur theorie des diamagnetismus von leitungselektronen. *Zeitschrift für Physik A Hadrons and Nuclei*, 80:763–791, 1933. 10.1007/BF01342591.

[70] L. A. Bunimovich. On the ergodic properties of some billiards. *Funct. Anal. App.*, 8:73–74, 1974.

[71] Patrick W. O'Connor and Eric J. Heller. Quantum localization for a strongly classically chaotic system. *Phys. Rev. Lett.*, 61:2288–2291, Nov 1988.

[72] S. Sridhar and E. J. Heller. Physical and numerical experiments on the wave mechanics of classically chaotic systems. *Phys. Rev. A*, 46:R1728–R1731, Aug 1992.

[73] Steven Tomsovic and Eric J. Heller. Long-time semiclassical dynamics of chaos: The stadium billiard. *Phys. Rev. E*, 47:282–299, Jan 1993.

[74] Fernando P. Simonotti, Eduardo Vergini, and Marcos Saraceno. Quantitative study of scars in the boundary section of the stadium billiard. *Phys. Rev. E*, 56:3859–3867, Oct 1997.

[75] Alex Barnett, Doron Cohen, and Eric J. Heller. Deformations and dilations of chaotic billiards: Dissipation rate, and quasiorthogonality of the boundary wave functions. *Phys. Rev. Lett.*, 85:1412–1415, Aug 2000.

[76] Eric J. Heller. Bound-state eigenfunctions of classically chaotic hamiltonian systems: Scars of periodic orbits. *Phys. Rev. Lett.*, 53(16):1515–1518, Oct 1984.

[77] Alex Barnett, Doron Cohen, and Eric J. Heller. Deformations and dilations

of chaotic billiards: Dissipation rate, and quasiorthogonality of the boundary wave functions. *Phys. Rev. Lett.*, 85:1412–1415, Aug 2000.

[78] Doron Cohen, Alex Barnett, and Eric J. Heller. Parametric evolution for a deformed cavity. *Phys. Rev. E*, 63:046207, Mar 2001.

[79] Th. von Kármán. Über den mechanismus des widerstandes, den ein bewegter körper in einer flussigkeit erzeugt. *Nacht. Wiss. Ges. Göttingen. Math. Phys. Klasse*, 509, 1911.

[80] G.D. Birkhoff. *Dynamical systems.* Colloquium Publications // American Mathematical Society. Edwards, 1927.

[81] P. Garbaczewski and R. Olkiewicz. *Dynamics of dissipation.* Lecture notes in physics. Springer, 2002.

[82] Ioan Kosztin, Dmitrii L. Maslov, and Paul M. Goldbart. Chaos in andreev billiards. *Phys. Rev. Lett.*, 75:1735–1738, Aug 1995.

[83] Melinda Y. Han, Barbaros Özyilmaz, Yuanbo Zhang, and Philip Kim. Energy band-gap engineering of graphene nanoribbons. *Phys. Rev. Lett.*, 98:206805, May 2007.

[84] K. S. Novoselov, Z. Jiang, Y. Zhang, S. V. Morozov, H. L. Stormer, U. Zeitler, J. C. Maan, G. S. Boebinger, P. Kim, and A. K. Geim. Room-temperature quantum hall effect in graphene. *Science*, 315(5817):1379, 2007.

[85] Elena Stolyarova, Kwang Taeg Rim, Sunmin Ryu, Janina Maultzsch, Philip Kim, Louis E. Brus, Tony F. Heinz, Mark S. Hybertsen, and George W. Flynn.

High-resolution scanning tunneling microscopy imaging of mesoscopic graphene sheets on an insulating surface. *Proceedings of the National Academy of Sciences*, 104(22):9209–9212, 2007.

[86] G. M. Rutter, J. N. Crain, N. P. Guisinger, T. Li, P. N. First, and J. A. Stroscio. Scattering and interference in epitaxial graphene. *Science*, 317(5835):219–222, 2007.

[87] Yuanbo Zhang, Victor W. Brar, Caglar Girit, Alex Zettl, and Michael F. Crommie. Origin of spatial charge inhomogeneity in graphene. *Nat Phys*, 5(10):722–726, 10 2009.

[88] J Berezovsky, M F Borunda, E J Heller, and R M Westervelt. Imaging coherent transport in graphene (part i): mapping universal conductance fluctuations. *Nanotechnology*, 21(27):274013, 2010.

[89] Jesse Berezovsky and Robert M Westervelt. Imaging coherent transport in graphene (part ii): probing weak localization. *Nanotechnology*, 21(27):274014, 2010.

[90] Michael Wimmer, İnan ç Adagideli, Sava ş Berber, David Tománek, and Klaus Richter. Spin currents in rough graphene nanoribbons: Universal fluctuations and spin injection. *Phys. Rev. Lett.*, 100(17):177207, May 2008.

[91] Wei L. Wang, Sheng Meng, and Efthimios Kaxiras. Graphene nanoflakes with large spin. *Nano Letters*, 8(1):241–245, 2008. PMID: 18052302.

[92] Michael Wimmer, Matthias Scheid, and Klaus Richter. Spin-polarized Quantum

Transport in Mesoscopic Conductors: Computational Concepts and Physical Phenomena. *arXiv:0803.3705*, 2008.

[93] T. O. Wehling, K. S. Novoselov, S. V. Morozov, E. E. Vdovin, M. I. Katsnelson, A. K. Geim, and A. I. Lichtenstein. Molecular doping of graphene. *Nano Letters*, 8(1):173–177, 2008. PMID: 18085811.

[94] Stephan Schnez, Johannes Güttinger, Magdalena Huefner, Christoph Stampfer, Klaus Ensslin, and Thomas Ihn. Imaging localized states in graphene nanostructures. *Phys. Rev. B*, 82:165445, Oct 2010.

[95] T. O. Wehling, A. V. Balatsky, M. I. Katsnelson, A. I. Lichtenstein, K. Scharnberg, and R. Wiesendanger. Local electronic signatures of impurity states in graphene. *Phys. Rev. B*, 75:125425, Mar 2007.

[96] L. Simon, C. Bena, F. Vonau, D. Aubel, H. Nasrallah, M. Habar, and J. C. Peruchetti. Symmetry of standing waves generated by a point defect in epitaxial graphene. *The European Physical Journal B - Condensed Matter and Complex Systems*, 69:351–355, 2009. 10.1140/epjb/e2009-00142-3.

[97] H. Amara, S. Latil, V. Meunier, Ph. Lambin, and J.-C. Charlier. Scanning tunneling microscopy fingerprints of point defects in graphene: A theoretical prediction. *Phys. Rev. B*, 76:115423, Sep 2007.

[98] M.I Katsnelson and A.K Geim. Electron scattering on microscopic corrugations in graphene. *Philosophical Transactions of the Royal Society A: Mathematical, Physical and Engineering Sciences*, 366(1863):195–204, 2008.

[99] Pekka Koskinen, Sami Malola, and Hannu Häkkinen. Evidence for graphene edges beyond zigzag and armchair. *Phys. Rev. B*, 80:073401, Aug 2009.

[100] Jifa Tian, Helin Cao, Wei Wu, Qingkai Yu, and Yong P. Chen. Direct imaging of graphene edges: Atomic structure and electronic scattering. *Nano Letters*, 11(9):3663–3668, 2011.

[101] Kyle A. Ritter and Joseph W. Lyding. The influence of edge structure on the electronic properties of graphene quantum dots and nanoribbons. *Nature Materials*, 8(3):235–242, 03 2009.

[102] David K. Ferry, Jonathan P. Bird, Richard Akis, David P. Pivin Jr., Kevin M. Connolly, Koji Ishibashi, Yoshinobu Aoyagi, Takuo Sugano, and Yuichi Ochiai. Quantum transport in single and multiple quantum dots. *Jpn. J. Appl. Phys.*, 36(Part 1, No. 6B):3944–3950, 1997.

[103] Andrey E. Miroshnichenko, Sergej Flach, and Yuri S. Kivshar. Fano resonances in nanoscale structures. *Rev. Mod. Phys.*, 82:2257–2298, Aug 2010.

[104] D. K. Ferry, R. Akis, and J. P. Bird. Einselection in action: Decoherence and pointer states in open quantum dots. *Phys. Rev. Lett.*, 93:026803, Jul 2004.

[105] J. Göres, D. Goldhaber-Gordon, S. Heemeyer, M. A. Kastner, Hadas Shtrikman, D. Mahalu, and U. Meirav. Fano resonances in electronic transport through a single-electron transistor. *Phys. Rev. B*, 62:2188–2194, Jul 2000.

[106] Kensuke Kobayashi, Hisashi Aikawa, Akira Sano, Shingo Katsumoto, and Ya-

suhiro Iye. Fano resonance in a quantum wire with a side-coupled quantum dot. *Phys. Rev. B*, 70:035319, Jul 2004.

[107] L. E. Calvet, J. P. Snyder, and W. Wernsdorfer. Fano resonance in electron transport through single dopant atoms. *Phys. Rev. B*, 83:205415, May 2011.

[108] L.L. Sohn, L.P. Kouwenhoven, and G. Schön. *Mesoscopic electron transport*. NATO ASI series: Applied sciences. Kluwer Academic Publishers, 1997.

[109] D.K. Ferry and S.M. Goodnick. *Transport in nanostructures*. Cambridge Studies in Semiconductor Physics and Microelectronic Engineering. Cambridge University Press, 1999.

[110] I.O. Kulik and R. Ellialtıoğlu. *Quantum mesoscopic phenomena and mesoscopic devices in microelectronics*. NATO science series: Mathematical and physical sciences. Kluwer Academic, 2000.

[111] J.P. Bird. *Electron transport in quantum dots*. Kluwer Academic Publishers, 2003.

[112] S. Datta. *Quantum transport: atom to transistor*. Cambridge University Press, 2005.

[113] Jürgen Wurm, Adam Rycerz, İnan ç Adagideli, Michael Wimmer, Klaus Richter, and Harold U. Baranger. Symmetry classes in graphene quantum dots: Universal spectral statistics, weak localization, and conductance fluctuations. *Phys. Rev. Lett.*, 102:056806, Feb 2009.

[114] Liang Huang, Ying-Cheng Lai, David K Ferry, Richard Akis, and Stephen M Goodnick. Transmission and scarring in graphene quantum dots. *Journal of Physics: Condensed Matter*, 21(34):344203, 2009.

[115] D K Ferry, L Huang, R Yang, Y-C Lai, and R Akis. Open quantum dots in graphene: Scaling relativistic pointer states. *Journal of Physics: Conference Series*, 220(1):012015, 2010.

[116] Liang Huang, Rui Yang, and Ying-Cheng Lai. Geometry-dependent conductance oscillations in graphene quantum dots. *EPL (Europhysics Letters)*, 94(5):58003, 2011.

[117] A. R. Akhmerov and C. W. J. Beenakker. Boundary conditions for dirac fermions on a terminated honeycomb lattice. *Phys. Rev. B*, 77(8):085423, Feb 2008.

[118] Jie-Yun Yan, Ping Zhang, Bo Sun, Hai-Zhou Lu, Zhigang Wang, Suqing Duan, and Xian-Geng Zhao. Quantum blockade and loop current induced by a single lattice defect in graphene nanoribbons. *Phys. Rev. B*, 79:115403, Mar 2009.

[119] L. P. Zârbo and B. K. Nikolić. Spatial distribution of local currents of massless dirac fermions in quantum transport through graphene nanoribbons. *EPL (Europhysics Letters)*, 80(4):47001, 2007.